UNIVERSITY OF CALIFORNIA SAN DIEGO

Microstructure observations of mixing and turbulent heat fluxes in the western Arctic Ocean

A dissertation submitted in partial satisfaction of the
requirements for the degree
Doctor of Philosophy

in

Oceanography

by

Elizabeth Coombs Fine

Committee in charge:

Professor Matthew Alford, Co-Chair
Professor Jennifer MacKinnon, Co-Chair
Professor Ian Eisenman
Professor Robert Pinkel
Professor Sutanu Sarkar
Professor Fiammeta Straneo

2019

The dissertation of Elizabeth Coombs Fine is approved, and it is acceptable in quality and form for publication on microfilm and electronically:

_____

_____

_____

_____

_____
Co-Chair

_____
Co-Chair

University of California San Diego

2019

TABLE OF CONTENTS

LIST OF FIGURES

LIST OF TABLES

ACKNOWLEDGEMENTS

My advisors Jennifer MacKinnon and Matthew Alford are mentors in every sense of the word, and I am extremely grateful for their intellectual insights and personal support. Over the course of my graduate career they have provided encouragement, inspiration, and leadership by example, and have taught me how to be a scientist. I would also like to acknowledge the contributions of my committee, Ian Eisenman, Robert Pinkel, Sutanu Sarkar, and Fiamma Straneo. They have shared essential support, advice, and context for my work.

John Mickett, who co-authored all three of my thesis chapters, has provided invaluable perspectives and insight and has given generous feedback on multiple iterations and drafts. Thomas Peacock and Arnaud le Boyer have also contributed both to this work and to my development as a scientist. Ruth Musgrave and Amy Waterhouse have been very generous in sharing scientific insight, opportunities, and their personal experience. I am also especially grateful to Robert Pickart for welcoming me onboard the Healy. Many other scientists have helped me develop as an oceanographer, and I would particularly like to acknowledge Harper Simmons, Jonathan Nash, and Peter Franks in this regard.

One of the highlights of my graduate career has been the 139 days I've spent at sea. The captains and crews I sailed with onboard the *R/Vs* Sikuliaq, Revelle, Healy, Sally Ride, and Sproul have provided technical and scientific support and a safe environment to learn the (sometimes literal) ropes of life at sea. I could not be more grateful for the stories and memories I have from those journeys.

My foray into physical oceanography began with a summer internship with Robert Pinkel, Andrew Lucas, and Michael Goldin. I am extremely grateful to them for sharing the wonders of seagoing oceanography with me. As the MOD group has grown and developed, I have benefited from a supportive community of engineers, scientists, students, postdocs, and friends. Thank you all for creating such a wonderful place to work and live.

I began graduate school with the PO class of 2014. Isabella Arzeno, Bia Villas Boas, Paul

Chamberlain, Derek Grimes, Stephen Holleman and Olavo Marques, I have learned so much from each of you over the years. I have benefitted immensely from friendships with those outside of our immediate cohort as well, including the bullpen group and the JOE working group, and from all of my officemates, shipmates and colleagues.

I'm grateful for the support of many people, beginning with my parents and grandparents who fostered a love of learning and the outdoors from my early childhood. From there I have had a number of great teachers and mentors, including Professor Burchat, who convinced me I could complete a physics major, and Dr. Frank Bryan at NCAR, who mentored me through my master's degree. The faculty and staff of SIO have also been incredibly helpful over these years, and my extended family and in-laws have been a font of love and wisdom. I could not have completed this program without the support, guidance, and mentoring I've received from all quarters.

Finally, a special thank you to Michael and Nala. To Nala for her unyielding loyalty, affection, and joyful enthusiasm when she hears it's time to go to work. And to Michael for absolutely everything.

Chapter 2, in full, is being prepared for submission for publication. Fine, Elizabeth; Alford, Matthew H.; MacKinnon, Jennifer A.; Mickett, John B. The dissertation author was the primary investigator and author of this paper.

Chapter 3, in full, is a reprint of the material as it appears in Journal of Physical Oceanography 2018. Fine, Elizabeth; MacKinnon, Jennifer A.; Alford, Matthew H.; Mickett, John B. Microstructure observations of turbulent heat fluxes in a warm-core Canada Basin eddy. J. Phys. Oceanogr., 48:2397-2418. The dissertation author was the primary investigator and author of this paper. © American Meteorological Society. Used with permission.

Chapter 4, in full, is being prepared for submission for publication. Fine, Elizabeth; MacKinnon, Jennifer A.; Alford, Matthew H.; Mickett, John B.; Peacock, Thomas; le Boyer, Arnold. The dissertation author was the primary investigator and author of this paper.

VITA

2011	B.S. in Physics, Minor in Philosophy, Stanford University
2014	M.S. in Physics, University of Colorado Boulder
2019	Ph.D. in Oceanography, University of California San Diego

PUBLICATIONS

Fine, E.C., J. A. MacKinnon, M. H. Alford, J. B. Mickett, T. Peacock, A. Le Boyer (2019). Mixing of Pacific Summer Water intrusions, eddies, and filaments in the Beaufort Sea, *in prep*.

Fine, E.C., J. A. MacKinnon, M. H. Alford, J. B. Mickett (2019). Near-inertial waves and microstructure mixing observations in the Beaufort Sea. *in prep*.

Fine, E.C., J. A. MacKinnon, M. H. Alford, J. B. Mickett (2018). Microstructure observations of turbulent heat fluxes in a warm-core Canada Basin eddy. *J. Phys. Oceanogr.*, 48:2397-2418

MacKinnon, J. A., J. D. Nash, M. H. Alford, A. J. Lucas, J. B. Mickett, E. Shroyer, A. F. Waterhouse, A. Tandon, D. Sengupta, A. Mahadevan, M. Ravichandran, R. Pinkel, D. Rudnick, C. B. Whalen, M. S. Alberty, J. Sreelehka, **E. C. Fine**, D. Chaudhuri, G. L. Wagner (2015). A tale of two spicy seas. *Oceanography*, 29:50–61

Fine, E. C., F. O. Bryan, W. G. Large, D. A. Bailey (2015), An initial estimate of the global distribution of diurnal variation in sea surface salinity, *J. Geophys. Res. Oceans* 120: 3211-3228.

Xu, M., D. A. Tieri, **E. C. Fine**, J. K. Thompson, and M. J. Holland (2014), Synchronization of Two Ensembles of Atoms. *Phys. Rev. Lett.*, 113:154101-154106.

ABSTRACT OF THE DISSERTATION

Microstructure observations of mixing and turbulent heat fluxes in the western Arctic Ocean

by

Elizabeth Coombs Fine

Doctor of Philosophy in Oceanography

University of California San Diego, 2019

Professor Matthew Alford, Co-Chair
Professor Jennifer MacKinnon, Co-Chair

The Arctic Ocean is characterized by a halocline rather than a thermocline, so that fresh water is found at the surface, with saltier (and often warmer) water beneath. In the western Arctic, the Pacific and Atlantic Oceans provide sources of oceanic heat. The year-round Pacific Summer Water (PSW) temperature maximum is found 40-80 m beneath the sea surface, while Atlantic Water (AW) is generally found deeper than 200 m. Both the Atlantic and Pacific source waters are warming, and the heat content of PSW has nearly doubled over the last three decades.

The broad goals of this disseration are to identify the processes that regulate the release

of heat out of these two water masses, to quantify the heat transported upwards where it may affect sea ice, and to understand how these processes may evolve in a changing Arctic Ocean. Microstructure data collected during the 2015 ArcticMix and 2018 Stratified Ocean Dynamics of the Arctic (SODA) process cruises provide a unique opportunity to observe the small-scale mixing associated with subsurface heat in the Canada Basin.

Multiple processes play a role in setting turbulence rates in the western Arctic. Widespread double diffusive convection results in small upwards heat fluxes out of the AW. We investigate the possible influence of observed wind-generated near-inertial internal waves on AW turbulent heat fluxes and find that the impact is minimal, with AW heat fluxes consistently low due to a number of factors inhibiting the creation and vertical propagation of internal waves. We additionally investigate the relative importance of mixing processes associated with anomalously warm PSW intrusions. We find double diffusive convection results in high upwards heat fluxes out of two separate warm intrusions, one warm-core eddy observed in the 2015, and one slope current intrusion observed in 2018. We document a relationship between the vertical complexity of warm intrusions and the total heat flux out of them, with more complex vertical structure corresponding to increased overall mixing. This relationship is supported by 12 microstructure surveys that sampled PSW conducted across both 2015 and 2018.

Chapter 1

Introduction

The Arctic Ocean differs from most of the global oceans for a number of reasons. The Arctic Ocean is much colder and fresher than most of the global ocean, with most of its waters within a few degrees of the freezing point. These two features result in a halocline stratification of the Arctic Ocean, with fresh water found near the surface, rather than the more typical thermocline stratification. The Arctic Ocean currently has a annually persistent ice cap, with seasonal variation in its surface extent and volume. The Arctic Ocean is also relatively isolated from the rest of the Global Ocean. It is a mediterranean sea, with two primary connections with the Pacific and Atlantic oceans in the Bering and Fram Straits respectively. These two inflows represent opportunities for relatively warm and salty water from the Atlantic and Pacific Oceans to flow into the Arctic. The warm input from these inflows results in two distinct Arctic water masses: the Atlantic Water (AW), which is found throughout the Arctic Ocean, and the Pacific Water (PW), which is lesser in volume due to the shallowness of the Bering Strait, and is almost exclusively found in the western Arctic. Due to the relative saltiness of each of these water masses and the haline stratification of the Arctic, both subduct upon arrival into the Arctic basin and are found at depth, with relatively fresh PW found between 30-200 m depth, and saltier AW found from 200-800 m in the western Arctic. Pacific Water has different characteristics that are set seasonally

prior to its subduction, with warmer and fresher Pacific Summer Water influenced by river runoff and insolation, and Pacific Winter Water colder and saltier due to brine rejection in the Chukchi sea and Beaufort Shelf. Although these water masses are formed seasonally, both are annually persistent within the western Arctic. These subsurface water masses result in an unusual situation in which turbulent mixing has a tendency to transport heat upwards from PSW and AW in much of the western Arctic halocline. Along with unusual physical oceanography, the Arctic Ocean supports both a unique ecosystem and the traditional lifestyles of local indigenous communities.

The Arctic Ocean has been dramatically affected by climate change. All available data suggests a precipitous drop in both summer and winter sea ice surface area and volume, concurrent with an increase in air temperatures and an increase in the heat transport through the Bering and Fram Strait inflows. Heat fluxes from both the ocean and the atmosphere to sea ice vary throughout the year, but only an additional 1 W m^{-2} of average heat flux to the ice is needed to produce the observed sea ice declines (Carmack et al., 2015). Multiple climatological processes may provide that heat, including ice albedo feedback, changes in cloud cover, and changes in atmospheric temperatures, as well as changes in oceanic heat fluxes. The relative contributions of each of these processes is not well-understood.

The present work is largely concerned with the oceanic processes that result in vertical heat fluxes in the western Arctic, and how these processes may be influenced by a changing climate. The first of these proccesses is internal wave-driven turbulent mixing. This type of ocean mixing is generally the dominant mixing process away from continental shelves and topography (MacKinnon et al., 2017). Energy is input into the ocean at relatively large spatial and temporal scales, primarily by the winds and the tides. Due to wave-wave interactions, this energy is transfered downscale to smaller and smaller length and time scales, until it reaches dissipative scales, ultimately resulting in mixing. Both wind and tide energy input to the Arctic Ocean is generally weaker than that at lower latitudes, and correspondingly the Arctic Ocean's internal wave field is approximately an order of magnitude less energetic than the typical midlatitude

internal wave field (Morison et al., 1985). Turbulent kinetic energy dissipation rates are also significantly lower over most of the Arctic ocean than at other latitudes (Fer, 2009). However, a reduction in the Arctic's sea ice cover provides more increased opportunity for wind energy to enter the ocean interior, potentially resulting in increased mixing rates, and corresponding heat fluxes.

The thermohaline stratification of the Arctic Ocean is also susceptible to a second type of mixing, double diffusion. Double diffusion occurs due to the difference in the molecular diffusivities of heat and salt. In particular, double diffusive convection, which occurs when cool and fresh water lies above warm and salty water, provides a mechanism for the vertical transport of heat even in the absence of background mixing. Double diffusion is frequently observed above the Atlantic Water throughout the Arctic Ocean (Timmermans et al., 2008b; Shibley et al., 2017). It is also less commonly observed above particularly warm PSW intrusions (Kawaguchi et al., 2014; Timmermans and Jayne, 2016). The strength of a double diffusive instability is assessed by considering the density ratio, defined here as

$$R_\rho = \frac{\beta \Delta S}{\alpha \Delta T}. \tag{1.1}$$

in which ΔS and ΔT are the changes in salinity and temperature over a given length scale, and α and β are the thermal expansion and haline contraction coefficients, respectively. Double diffusive convection occurs above warm and salty intrusions, while salt-fingering occurs below such intruions. As the temperature of both Atlantic and Pacific water inflows increase, temperature gradients between warm inflow water and the winter water masses that are generally near the freezing temperature sharpens, and the thermal expansion coefficient α increases. Both of these factors result in lower (and hence increasingly unstable) density ratios, indicating that as inflows warm double diffusion may become an increasingly important process in setting vertical heat fluxes.

The data used in this dissertation were collected during two western Arctic process cruises, the ArcticMix cruise conducted in September 2015 and the Stratified Ocean Dynamics of the Arctic (SODA) process cruise conducted in September 2018. Both cruises were conducted over a similar region of the Chukchi shelf and Beaufort sea, and both included microstructure sampling that allows for the direct calculation of turbulent diffusivities and fluxes.

In Chapter 2, we investigate the hypothesis that a decline in sea ice may result in more efficient energy transfer from the wind to the ocean interior, resulting in increased vertical heat fluxes out of the Atlantic Water. A wind event occurred at the beginning of the ArcticMix cruise and a nine-day moored profiler record documented wind generated near-inertial internal waves in response. Two microstructure surveys, one taken just after the event and the other nine days after the event allow us to investigate the effect this internal wave response had on turbulent heat fluxes and mixing. We find that while near-inertial internal waves were observed following the wind event, the rate of turbulent dissipation of kinetic energy (ε) was only slightly elevated above 150 m, and was unchanged below that depth. We estimate the energy flux from the wind to the ocean with the use of a slab model and estimate the vertical energy flux in the internal wave field from the mooring observations. Atlantic Water heat fluxes were minimal.

During the ArcticMix cruise, a warm-core intrahalocline eddy was observed in the vicinity of Barrow Canyon. This eddy is described in detail in Chapter 3 (Fine et al., 2018). Its core consisted of Pacific Summer Water in anticyclonic rotation. Using microstructure measurements, we estimate both vertical and lateral heat fluxes out of the eddy, as well as the total heat transport in each direction. We find that distinct processes determine the heat flux in each direction, with double diffusive convection resulting in an upwards heat flux of 5 W m^{-2} out the eddy's top, thermohaline intrusions resulting in lateral heat fluxes of 2000 W m^{-2} out of its sides, and shear-driven turbulence resulting in downwards heat fluxes of 0.5 W m^{-2} from the eddy's bottom. The overall lifetime of the eddy is estimated to be 1-2 years and is set by the large lateral heat fluxes.

In Chapter 4, we consider the relationship between lateral stirring of Pacific Summer Water and the vertical processes that contribute to small-scale mixing. A survey of a Pacific Summer Water intrusion in the Chukchi slope current during the SODA cruise emphasizes the interdependency of these processes, with lateral stirring setting up a complex structure of strong thermohaline gradients. When sharp enough, these gradients become double diffusively unstable, resulting in elevated ε along strong temperature gradients. Examining all microstructure surveys taken during both the ArcticMix and SODA cruises shows a correlation between the variance of thermal gradients and the total heat transported from PSW intrusions into the background cool water. Multiple factors conspire to facilitate this heat transfer, with lateral stirring resulting in sharpened gradients and increased surface area between the water masses, sharpened gradients resulting in elevated double diffusive fluxes, and all three factors leading to increased heat fluxes.

All three chapters contribute to a growing body of literature detailing the distribution of heat in the Arctic Ocean, the processes that control this distribution, and the impact of this increased heat on both regional and global climate. Our hope is that an improved understanding of these processes will support better understanding, prediction, and ulimately mitigation of rapid climate change in one of the most unique places on the planet.

Chapter 2

Near-inertial waves and microstructure mixing observations in the Beaufort Sea

2.1 Introduction

The Arctic Ocean is currently facing a rapidly changing climate. The minimum summer sea ice extent has declined dramatically in the last decades, and this trend is predicted to continue in coming years. As sea ice retreats, areas of the upper ocean over which sea ice previously mediated atmospheric forcing become subject to direct momentum and buoyancy fluxes. Sea ice retreat has been particularly rapid in the western Arctic, and especially over the Beaufort Sea (Carmack et al., 2015).

The western Arctic Ocean is characterized by a double halocline with substantial amounts of sub-surface heat. At the surface, there is a layer of cool and fresh water associated with sea ice. Beneath the surface, Pacific Summer Water is formed due to summertime subduction of relatively warm Pacific-origin water and is found from approximately 30-100 m deep. This water mass is separated from the deeper Alantic Water by colder and saltier Pacific Winter Water that forms in the shelf seas surrounding the western Arctic. The Atlantic Layer, which in the western Arctic is

found between 200-800 m depth, contains enough heat to melt the entirety of the Arctic ice cap many times over if it were transported directly to the surface (Rudels et al., 2004).

Due to the heat contained in the interior Arctic ocean, the rate of vertical turbulent mixing plays a crucial role in setting upwards heat fluxes that may affect sea ice at the surface. Compared to mid-latitude oceans, mixing rates tend to be low in the western Arctic, minimizing the impact of heat found at 200 m and deeper on near-surface heat content and ocean-ice heat fluxes (Padman and Dillon, 1987; Rainville and Winsor, 2008; Fer, 2009; Shaw et al., 2009; Toole et al., 2010; Jackson et al., 2010; Lincoln et al., 2016).

Most mixing in the stratified ocean interior is driven by breaking internal waves, which are primarily forced by the wind and the tides (Munk and Wunsch, 1998). Wave-wave interactions transfer energy to increasingly high wavenumbers, leading to instabilities that result in turbulent mixing. The degree of mixing from breaking internal waves has been found to be related to the spectral level of the wave field. While regional features of the internal wave field vary, throughout much of the global ocean the empirical Garrett and Munk spectrum is a reasonable approximation of both the overall internal wave energy and its frequency and wave number distribution (Garrett and Munk, 1972, 1975; Cairns and Williams, 1976; Polzin et al., 2014). However, in the western Arctic the energy content of the internal wave field has historically been an order of magnitude smaller than the Garrett and Munk spectrum (Levine et al., 1985). The presence of sea ice and weak Arctic tides have already been mentioned as factors that tend to limit the energy available to the Arctic internal wave field. The Arctic Ocean is additionally well north of the mid-latitude storm track that is a hot-spot of wind input to the internal wave field (Alford, 2001). The internal waves that do form may also tend to dissipate in the ice-ocean boundary layer after a single reflection off the ocean bottom (Pinkel, 2005).

Retreating sea ice and a corresponding increase of wind-driven momentum transfer into the western Arctic Ocean has been hypothesized to have significant implications for stratification and vertical heat transport (Rainville and Woodgate, 2009; Dosser and Rainville, 2016). If a

reduction in summer sea ice were to substantially increase the transfer of energy from the wind into the interior Arctic ocean, this could result in increased dissipation at depth and more mixing of the deep ocean. Such mixing could transport heat from Atlantic Water upwards, potentially creating a feedback loop as increasing vertical heat fluxes accelerate sea ice melt.

Some observations suggest an increase in internal wave energy in response to wind forcing in regions with reduced summer sea ice. Energetic internal waves have been observed in mooring data from July through September, when sea ice is near its seasonal minimum (Rainville and Woodgate, 2009). An upward trend in near-inertial internal wave amplitudes has been identified in ITP records from 2005-2014 (Dosser and Rainville, 2016). Comparisons between ITPs in lower and higher ice concentrations demonstrate that more internal wave energy is found surrounding the ITPs in low sea-ice concentration regions (Cole et al., 2018), and the same effect has been observed by moorings on the Beaufort slope (Martini et al., 2014). As the summer Arctic becomes increasingly ice-free, wind-forced near-inertial internal waves provide a pathway for energy to enter the interior of the western Arctic.

In spite of observations of increased internal wave energy in response to surface forcing, observations in the western Arctic have not found a corresponding increase in the rate of dissipation of TKE (ε) in the ocean interior in response to surface forcing. Indirect estimates of ε compared across the last decades have not identified substantial increases in recent years (Guthrie et al., 2013; Lique et al., 2014). In a summer of 2012 study, Lincoln et al. (2016) directly measured microstructure following a storm that occurred over ice-free waters. While near-inertial internal waves were observed, ε and heat fluxes out of the Atlantic water were not elevated beyond typical background rates. These observations suggest that even during large storms, wind energy tranfer into the interior ocean may not cause a significant increase in local ε and corresponding mixing in the Arctic Ocean's Atlantic halocline.

Shipbased sampling in the Arctic is seasonally constrained, and *in situ* microstructure measurements are scarce, making it difficult to determine whether mixing rates are changing on

decadal timescales. There is a large impetus to develop and test methods such as finescale parameterizations that infer mixing estimates from widely available (often autonomously collected) data. Finescale parameterizations infer dissipation from larger scale measurements by assuming that the ocean's internal wave field is locally in steady state, and that energy cascades from large vertical scales to dissipative scales via internal waves (Polzin et al., 2014). Provided these assumptions hold, ε can be inferred from observations of the internal wave field at scales much larger than the scales of dissipation. The large-scale observations may be based on either shear or strain (Kunze et al., 2006). Finescale parameterizations have been applied to both CTD and velocity data in the global ocean (e.g. Whalen et al. (2012, 2015); Kunze (2003); Kunze et al. (2006); Waterhouse et al. (2014); Polzin et al. (2014)). Generally, agreement between finescale parameterizations and direct microstructure measurements are robust to within a factor of two to three (Whalen et al., 2015), although they may diverge in regions where mixing occurs due to processes other than a downscale energy cascade in internal waves (e.g., topographic mixing, convection, double diffusive convection–see Polzin et al. (2014) and Waterman et al. (2014)). In the Arctic Ocean, finescale parameterizations are generally in good agreement with microstructure measurements (Guthrie et al., 2013; Lique et al., 2014; Chanona et al., 2018). However, to our knowledge there have been no direct comparisons between finescale parameterizations and microstructure measurements using data obtained simulaneously in the Arctic Ocean. Such comparisons are necessary both to understand the opportunities afforded by existing autonomous sampling systems to estimate mixing rates over climatological time scales, and to be aware of limitations that may arise in applying finescale parameterizations in an environment that is quite different from the low to mid-latitude oceans.

In the current study, we present observations collected by a mooring deployed in the Beaufort Sea in September of 2015 that captured the near-inertial internal wave (NIW) response to a wind forcing event in conjunction with concurrent microstructure observations made in the same region. Our analysis focuses on three main questions:

1. **Are there differences in the wind-driven generation of NIWs in the Arctic as compared to at lower latitudes that result in lower Arctic internal wave energy even in the absence of sea ice?** How do the unusual aspects of the Arctic environment affect NIW generation?

2. **Do NIWs substantially increase vertical eddy diffusivity and corresponding heat fluxes?** What diffusivities and heat fluxes are observed in this study region? Does NIW forcing contribute to vertical heat fluxes out of the Atlantic Water?

3. **Do finescale parameterizations applied in the western Arctic provide accurate mixing estimates?** Do these estimates at the mooring site agree with direct microstructure measurements collected during the same time frame?

Section 2 describes the methods used for data collection and analysis. Results from mooring and microstructure data, as well as a finescale parameterization are presented in section 3. Discussion and conclusions are shared in section 4.

2.2 Methods

2.2.1 Observations

Data were collected during a cruise onboard the R/V *Sikuliaq* from August 30th to September 26th of 2015. A mooring instrumented with four ADCPs and two McLane profilers was deployed at 72° 35.646' N, 145° 1.002' W from August 31st to September 19th 2015 (yeardays 242 to 262) (Fig. 2.1). During this time period, five microstructure surveys were made in the Beaufort Sea using a custom-built microstructure profiler. Due to instrument failure, the current study focuses on data collected during the first 9 days of the deployment, yeardays 242 to 251, and the two microstructure profiler surveys taken during this time frame (Fig. 2.1). Data for

the first microstructure survey were collected 85 km from the mooring on yearday 244, while data for the second were collected 102 km from the mooring on yearday 250.

The instruments deployed on the mooring consist of an upward-looking 300kHz ADCP and a downward-looking 75 kHz ADCP both mounted at 42 m depth, a McLane Moored Profiler that sampled from 42 m to 946 m, and an upward-looking 300 kHZ ADCP mounted at 957 m depth. Unfortunately the profiler stopped profiling on yearday 251, 9 days into the deployment. An additional profiler that was intended to sample from 983-2031 m deep and a fourth ADCP mounted at 2732 m both failed to collect any data. The profiler collected hourly profiles of CTD data and velocity data with a noise floor of ~ 3 cm s^{-1}.

Microstructure measurements were collected using a Modular Microstructure Profiler (MMP), developed by M. C. Gregg at the Applied Physics Laboratory of the University of Washington and currently operated by our group at the Scripps Institution of Oceanography. The MMP is a loosely-tethered profiler that falls at nominally 0.6 m s^{-1}. It carries two custom-built shear probes used to infer the turbulent kinetic energy dissipation rate (ε), an FP07 thermistor used to infer the rate of dissipation of thermal variance (χ), a Seabird CTD, and an altimeter for near-bottom sampling. The turbulent kinetic energy dissipation rate ($\varepsilon = (15/2)\nu\overline{\partial u/\partial z)^2}$) is calculated by iteratively fitting a Panchev curve to shear spectra measured by the shear probes and calculated over 2.5 second (1-2 m) windows, and is then binned to 0.25 m bins to match the scale of the CTD data.

2.2.2 Data products

Inverse model tidal velocities from the Arctic Ocean 5 km Inverse Model (AOTIM-5) are compared with mooring velocities to examine whether tidal forcing plays a significant role in the observations (Padman and Erofeeva, 2004).

Hourly 10 m winds from the NCEP CFSv2 (Saha et al., 2010) are used to force a slab model. These winds generate an Arctic surface wavefield that agrees reasonably well with

available buoy data (Stopa et al., 2016). However, comparing CFSv2 winds to measurements taken at Point Barrow (not shown) suggests that the reanalysis winds have lower variance around the inertial frequency by about a factor of 2.

2.2.3 Analysis

Finescale parameterization

Following previous studies, the rate of TKE dissipation is calculated as

$$\varepsilon = \varepsilon_0 \frac{\overline{N^2}}{N_0^2} \frac{\langle U_z^2 \rangle^2}{\langle U_{zGM}^2 \rangle^2} h_1(R_\omega) L(f,N). \tag{2.1}$$

Here, $\varepsilon_0 = 6.73 \times 10^{-10}$ W kg^{-1}, $N_0^2 = 3$ cph, U_z is finescale vertical shear, and $\langle U_{zGM}^2 \rangle$ represents the variance of vertical shear from the Garret and Munk 1976 model. The function h_1 is defined as

$$h_1(R_\omega) = \frac{3(R_\omega + 1)}{2\sqrt{2} R_\omega \sqrt{R_\omega - 1}} \tag{2.2}$$

and R_ω is the ratio of the variance of shear to strain,

$$R_\omega = \frac{\langle U_z^2 \rangle}{\overline{N^2} \langle \zeta_z^2 \rangle} \tag{2.3}$$

in which ζ represents isopycnal displacement. Strain is calculated as

$$\zeta_z = \frac{N^2 - N_{fit}^2}{\overline{N^2}} \tag{2.4}$$

in which $N^2(z)$ is the local buoyancy frequency squared, N_{fit}^2 is a polynomial fit over a given depth range to N^2, and $\overline{N^2}$ is the mean N^2 over that depth range (Gregg, 1989; Polzin et al., 1995;

Kunze et al., 2006; Whalen et al., 2015). The function $L(f,N)$ is defined as

$$L(f,N) = \frac{f \cosh^{-1}(\frac{\overline{N}}{f})}{f_{30} \cosh^{-1}(\frac{N_0}{f_{30}})} \tag{2.5}$$

in which f is the Coriolis frequency and f_{30} is the Coriolis frequency at 30°, and represents the latitudinal dependence of the internal wavefield (Gregg et al., 2003).

The profiler measured both density and velocity, allowing for direct calculation of the shear-to-strain ratio R_ω. To apply a finescale parameterization, we bin the data into overlapping depth windows. The shallowest depth used for the analysis was 75 m, as above this depth the stratification varied too rapidly with depth. Below 300 m, the signal in strain is dominated by double diffusive layering, so we limit our analysis to the 75-300 m depth range. The top window used for the finescale parameterization has a height of 75 m, while the other windows are 100 m tall (see Table 2.1). This is also the depth range over which we have concurrent microstructure measurements.

For the calculation of shear, we follow Kunze et al. (2006) and multiply velocity spectra by $N_0/\overline{N}$ where $\overline{N}$ is buoyancy frequency averaged in each depth range over the entire time series and $N_0 = 3$. We detrend and window the scaled velocity using a cosine tapered window. A Fourier transform is applied to find velocity coefficients, and these are used to estimate velocity spectra. These are corrected by a $sinc^2$ function to account for the McLane profiler 2 m binning (Polzin et al., 2002). Averaging spectra together and then integrating up to a cutoff wavenumber allows us to estimate the relevant variance. We use 0.04 cpm as the high wavenumber cutoff to retain sufficient wavenumber range for the integration while avoiding small scales where white noise in velocity causes the shear spectra to rise linearly. Strain is processed similarly, but is not scaled or corrected. The same 0.04 cpm cutoff wavenumber is used.

Slab model

The near-inertial mixed layer response to wind forcing can be described through the use of a damped slab model (Pollard and Millard, 1970). Details of this model are described in D'Asaro (1985). In this analysis, the mixed layer depth H is inferred from the ADCP velocity record to be 15 m, while the artificial damping term $r = 0.05f$ is chosen to maximize correlation between the magnitude of slab model and observed velocities.

2.3 Results

2.3.1 Temperature, salinity, and density

Stratification in the western Arctic is almost entirely controlled by variations in salinity (Fig. 2.2). The mean stratification profile over the duration of the mooring deployment is characterized by relatively high stratification from 50 to 70 m ($N^2 = 6 \times 10^{-4}$ rad^2 s^{-2}) , which decays rapidly to about 150 m depth. This region is characterized by relatively cool and fresh water, with a local temperature maximum at $\sim$50 m that is characteristic of Pacific Summer Water and a local minimum at $\sim$100 m indicating the Pacific Winter Water. A second local maximum in stratification occurs between 150 and 250 m, with N^2 reaching values of about 2×10^{-4} rad^2 s^{-2} (or 0.1 cph). This secondary peak is associated with the top of the Atlantic Water. Beneath 250 m, the stratification rapidly decays, with N^2 reaching a value of 1.8×10^{-6} rad ^{2} s^{-2} at 750 m.

From about 200 to 450 m, the stratification is unstable to double diffusive convection. This is seen from the Turner Angle (Fig. 2.2c), defined as

$$Tu = arctan\left(\frac{-\alpha\Delta\theta}{\beta\Delta S}\right) - 45^\circ \tag{2.6}$$

in which α and β are the thermal expansion and haline contraction coefficients, and ΔT and ΔS are vertical gradients of temperature and salinity calculated as first differences over 2 m bins, then

smoothed over 8 m. A Turner angle between -90° and -45° indicates double diffusive convective instability, with -90° $< Tu < -51°$ indicating strong instability (generally Tu must be in this range for diffusive convective layering to be present). Strong instabilities are present from about 225-450 m.

2.3.2 Velocity and isopycnal displacement

The velocity signal is dominated by near-inertial internal waves (Fig. 2.3b,c). The observed upward phase propagation corresponds to downwards energy propagation, consistent with surface generation (Gill, 1982). The mooring was deployed immediately following a wind event that appears to have generated the observed near-inertial waves. Hourly surface winds from the NCEP CFSv2 wind reanalysis product show a wind event occuring two days before the mooring deployment (Fig. 2.3a).

At the latitude of our observations, the inertial frequency ($f = 1.387 \times 10^{-4}$ rad s^{-1}) is quite close to the M2 tidal frequency (1.406 $\times 10^{-4}$ rad s^{-1}). Consequently we are unable to distinguish these two frequency bands over the mooring record. Tides are quite weak in the western Arctic (Fig. 2.3a; maximum modeled barotropic tidal velocities are approximately 0.2 cm/s). The appearance of near-inertial waves does not seem to be related to the barotropic spring/neap cycle.

Isopycnal displacement (η) is calculated from the 2 m gridded temperature and salinity measurements (Fig. 4.3d). The gridded density data are sorted in depth to create stably stratified profiles prior to calculating η. As in the velocity record, η is dominated by the signal of a downward-propagating NIW packet (Fig. 2.3b-d).

Upwards phase/downward energy propagation from the surface to depths of about 200 m is also apparent in horizontal kinetic energy density (HKE) (Fig. 2.4). A second pulse of energy centered around 175 m depth is also apparent.

2.3.3 Shear, N^2, and Richardson Number

The inverse Richardson number over 20 m vertical scales ($Ri^{-1}_{20m} \equiv \mathbf{U}^2_{z20m}/N^2_{20m}$), in which $\mathbf{U}^2_{z20m} = u^2_{z20m} + v^2_{z20m}$ is the vertical shear of horizontal currents and N_{20m} is the local buoyancy frequency, provides an indication as to where horizontal flow is susceptible to finescale shear instabilities (Fig. 2.3f, Miles (1961); Howard (1961)). Shear instabilities are possible where $Ri^{-1} > 4$. A 20 m scale for first-differencing is chosen to minimize the influence of high-wavenumber noise.

Shear ($\mathbf{U}^2_{z20m}$) is calculated by first differencing velocity over 20 m (Fig. 2.3g). It is elevated near the surface, and decays with depth around 200 m. The buoyancy frequency N^2_{20m} is also calculated as a first difference over 20 m, and is elevated near the surface and around 200 m.

Beneath 400 m, N^2_{20m} shows a distinct pattern due to double diffusive layers. These layers are found at the top of the Atlantic Water in the central basin, which is susceptible to a double diffusive convective instability (e.g., Padman and Dillon (1987); Shibley et al. (2017)). In this record, layers are always apparent below 400 m. On yearday 248, layers appear between 200-400 m (Fig. 2.3g). Their appearance appears to be due to the advection of a front past the mooring, with shallower layers existing on the northern side of the front; this event will be addressed in a future publication. These layers are not visible in the shear and velocity records as their vertical extent is smaller than the ADCP's vertical resolution. However, they are clearly visible in N^2_{20m} as alternating bands of high and low stratification.

We limit our analysis to depths above 400 m, as below this range noise in shear and double diffusive structure of N^2_{20m} dominates the signal. In this region, Ri^{-1}_{20m} is less than 1, indicating stable flow at vertical scales of 20 m (although Ri may be critical at smaller scales).

2.3.4 Microstructure observations

Direct measurements of ε from the MMP were made during two surveys within 100 km of the mooring (Fig. 4.1). The first of these consisted of 53 profiles taken over 14.5 hours on yearday 244, while the second consisted of 11 profiles taken over 3 hours on yearday 251 (Fig. 2.6). In these surveys, we see that ε is generally quite low ($\varepsilon < 3 \times 10^{-10}$ W kg^{-1}) below 50 m. However, above 150 m dissipation was elevated by a factor of 2-3 in the survey that took place on yearday 244 during the NIW event, relative to the survey undertaken on yearday 251. This suggests the NIW event was associated with measurablely increased dissipation in the upper water column. The maximum value of $\varepsilon = 6 \times 10^{-10}$ W kg^{-1} was found at 30 m depth during the survey on yearday 244.

One potential concern is that the observed values of ε are fairly near the 10^{-10} W kg^{-1} noise floor of the MMP. Histograms over both surveys show peaks at the instrument noise floor, implying that the true value of ε does often fall below 10^{-10} W kg^{-1}. However, both survey distributions have primary peaks around 2×10^{-10} m^2 s^{-3}, with a slightly higher peak in the earlier survey (Fig. 2.8). This suggests that averages calculated from the data are physically meaningful, if subject to overestimation. The buoyancy Reynolds number $Re_\nu = \varepsilon/(\nu N^2)$ (Fig. 2.6d) calculated during each survey suggests that even during the more energetic survey, dissipation rates were not strong enough to result in fully developed isotropic turbulence, defined where Re_ν is greater than 25 (Rohr et al., 1988). This is another factor that may result in overestimation of ε.

2.3.5 Finescale parameterization

Finescale parameterization estimates of ε were calculated in four depth bins. The shallowest bin spanned from 75 to 150 m depth centered at 112.5 m, and the next three were 100 m bins centered at 150 m, 200 m, and 250 m (Table 2.1). Mean shear and strain spectra in each of

these bins were approximately an order of magnitude less energetic than Garrett and Munk 76 levels (Fig. 2.7a-d).

Ratio of shear to strain

The ratio of shear to strain variance features prominently in the finescale parameterization as the nondimensional number R_ω. Many studies assume a set value for R_ω based on typical dynamics. However, the concurrent shear and strain measurements from the moored profiler permits the calculation of the ratio of normalized shear variance to strain variance R_ω directly from observations. This is done using 12-hour averaged vertical spectra of shear and strain over the profiler record (Fig. 2.7e-g). R_ω varies substantially in both time and in depth, with an average value of 5.3. There is substantial structure of R_ω in depth, with R_ω elevated in the uppermost depth bins due to the predominance of near-inertial waves (Chinn et al., 2016).

ε_{fs} estimates

Calculating a finescale estimate of ε (ε_{fs}) using R_ω calculated from the observed shear and strain results in estimates that are within a factor of three of the observed microstructure measurements in the top two depth bins; however, the deeper finescale estimates are an order of magnitude less than microstructure observations (Fig. 2.6c, 2.7). Estimates in the top two bins vary substantially in time and with R_ω, while the deeper estimates for ε_{fs} are approximately constant. In general, ε_{fs} varies with shear, which is mostly dominated by the near-inertial signal. This is consistent with the hypothesis that NIWs generate local mixing, and with microstructure observations showing elevated ε above 150 m during the survey on yearday 244 following the wind event.

Estimating ε_{fs} using a time-averaged vertical profile for R_ω rather than allowing for R_ω to vary in time does not affect results substantially, and although R_ω varies dramatically in depth, using a constant $R_\omega = 3$ only results in a factor of two change in ε_{fs} estimates (Fig. 2.6).

2.3.6 Mixing and heat fluxes

For a given ε, an upper bound for density diffusivity K_ρ may be calculated following Osborn 1980

$$K_\rho \leq \frac{\Gamma \varepsilon}{N^2} \tag{2.7}$$

in which Γ is a mixing efficiency generally taken to be 0.2 and N^2 is time-averaged buoyancy frequency. Thermal diffusivity is estimated assuming $K_\rho = K_T$, which allows for the calculation of a vertical heat flux $F_H = -\rho C_P K_T \theta_z$, with upward heat flux defined as positive. Upper bounds for diffusivities and heat fluxes for MMP surveys 1 and 2 and for the ε_{fs} estimates from finescale parameterization are quite low, with diffusivities 5-10 times the molecular diffusivity and all heat fluxes less than 0.05 W m^{-2}. As Re_ν is also quite low (Fig. 2.6d), these results should be treated as upper bounds, as turbulence is likely not isotropic.

2.4 Discussion

2.4.1 NIW energy input and loss

One of the primary motivations for this study was to understand why numerous observations have not seen an increase in ε and vertical turbulent Atlantic Water heat fluxes associated with the decline of sea ice and increased wind forcing. Wind forcing stimulates inertial oscillations within the ocean mixed layer. Convergences and divergences due to the horizontal variability of these oscillations drive NIWs, which propagate within the ocean interior. NIWs tranfer energies to small scales due to instabilities and wave-wave interactions, ultimately leading to dissipation. If wind forcing increases on decadal time scales with no corresponding increase in ε at depth, it seems there must be a “weak link" along this chain where energy is dissipated before reaching Atlantic Water. In this section we consider each step in turn based on the observations we have available. Because tides are extremely weak in this region and the observed waves propagated

downwards, we assume the near-inertial wave field is driven by the wind. Energy fluxes and dissipation rates estimated from each section are summarized in Table 2.3.

Energy flux from wind forcing to the mixed layer

Using a slab model and the NCEP CFSv2 hourly time series as described in section 2, we estimate the power input from the wind into the ocean's mixed layer during the storm.

When running a slab model, there is one free parameter r, which represents energy loss in the mixed layer either due to local turbulence or due to the radiation of internal waves. The parameter r is constrained to be larger than 0, and $r << f$ is required for stability. There is additionally the reference depth of the mixed layer, H_{ref}, which is determined from observations. As we have mixed layer velocity measurements available, we use these to tune r and H (within a range consistent with the observed mixed layer depth) to optimize agreement between the magnitudes of the slab model velocities and the near-inertial filtered observations. We find that using $H = 15$ m and $r = 0.05f$ is consistent with the observed data (R^2 = 0.7 with a two-hour phase shift). This is a lower ratio of r/f than the frequently used $r = 0.15f$ (Alford, 2001, 2003).

Using these parameters, we run a slab model and compare the results to the observed velocity (Fig. 2.5). Over the large wind event from yearday 240 to 242, the average wind stress is 0.1 N m^{-2} (Fig. 2.5a). Modeled mixed layer velocities during this period agree well with observations from the uplooking 300 kHz ADCP from the period when the mooring was deployed (Fig. 2.5 b and c, ADCP observations shown as dashed lines). During the same period, the average energy flux from the wind into the ocean is estimated as $\tau \cdot \mathbf{u_{model}}$ = 0.01 W m^2, in which τ is the wind stress calculated from the reanalysis winds (Fig. 2.5d).

The wind energy input into the ocean can also be estimated using the observed mixed layer velocities along with the reanalysis τ to calculate $\tau \cdot \mathbf{u_{obs}}$. Observed velocities are only available starting on yearday 243 when the mooring was deployed. Using the CFSv2 winds with $\mathbf{u_{obs}}$, the average energy flux from yearday 243 to 247 is 4 $\times 10^{-3}$ W m^{-2}. Over the same period,

calculating energy flux using $\mathbf{u_{mod}}$ results in a smaller flux of 3 $\times 10^{-3}$ W m^{-2}. This suggests that the total wind energy input into the ocean may be larger than the slab model estimate, which is consistent with observed mixed layer velocities that are slightly larger than modeled velocities (Fig. 2.5b and c). Comparing CFSv2 winds for the Point Barrow region to measurements taken at Point Barrow (not shown) suggests that the reanalysis winds have lower variance around the inertial frequency by about a factor of 2. If the clockwise rotating inertial frequency component of the wind forcing at the mooring location is underestimated by the reanalysis product, using the reanalysis winds likely would result in an underestimation of the wind-to-ocean energy flux.

NIW energy flux

The vertical energy flux in the internal wave field is $F = Ec_{gz}$, in which E is energy density (estimated throughout as horizontal energy density, due to the very small observed displacements) and c_{gz} is the vertical group velocity of the internal wave. We estimate the maximum energy density in the IW field as 0.006 J kg^{-1} or 6 J m^{-3} (Fig. 2.4). Robustly estimating c_{gz} is somewhat more complicated. We use three different approaches to bound this quantity. An estimate can be made directly from the horizontal kinetic energy figure (2.4c). Between yeardays 245 to 249, the pulse of HKE travels from approximately 70 to 140 m deep. This corresponds to a vertical group velocity of approximately 17 meters per day, or 2×10^{-4} m s^{-1}.

The group velocity can also be estimated from internal wave properties. The vertical group velocity c_{gz} is a function of the intrinsic frequency ω, vertical wavenumber m, and the effective inertial frequency f_{eff}:

$$c_{gz} = \frac{\omega^2 - f_{eff}^2}{m\omega}. \tag{2.8}$$

We do not have the spatial data necessary to determine relative vorticity, but assume that this is small so that $f_{eff} \approx f$. The intrinsic frequency ω can be estimated by applying a harmonic fit to the WKB stretched and scaled velocities. First, u and v velocities are stretched and scaled

following Sanford (1991) by dividing by smoothed N, filtered following Sanford (1991), and put onto a stretched coordinate

$$z^* = \frac{1}{N_0}\int N(z)dz \tag{2.9}$$

(see Fig. 2.2d and e). These quantities are lowpass filtered (Fig. 2.9a,c). A rotary filter is applied to isolate downward propagating energy (Fig. 2.9b,d).

For much of the record, the harmonic fit varies substantially in both depth and time, suggesting a multiwave environment. However, a window can be isolated in which the velocity signal is dominated by a single near-inertial wave, from stretched depth 165 to 220 and yearday 244.5 to 247. Within this window, the fit is relatively stable around an intrinsic frequency $\omega = 1.42 \times 10^{-4}$ rad s^{-1} $= 1.02f$. Using a vertical wavelength of 150 m estimated from the velocity data, this corresponds to a group velocity of 1.5 $\times 10^{-4}$ m s^{-1} $= 1.07f$, or 13 m day^{-1}.

The frequency of the observed wave can also be determined from the polarization equation:

$$v = -\frac{if}{\omega}u \tag{2.10}$$

For a given wave packet, we can estimate the intrinsic frequency as

$$\omega = f\sqrt{\frac{<u^2>}{<v^2>}} \tag{2.11}$$

This allows us to use a second method to determine the intrinsic frequency ω. At each depth an ellipse is fit to the filtered data, and ω is calculated based on the u and v velocites inferred from that fit. We again use the reduced window in which one NIW clearly dominates the signal. In this case, ω is 1.5×10^{-4} rad s^{-1}. This corresponds to a group velocity of 4 $\times 10^{-4}$ m s^{-1}, or 36 m day^{-1}.

Using $c_{gz} \sim 2 \times 10^{-4}$ m s^{-1} or 18 m day^{-1} (consistent with the observed propagation and between the two estimates from explicit fitting), we estimate a vertical internal wave energy flux

of $\sim 10^{-3}$ W m^{-2}. For comparison, the estimated lower bound for energy flux from the large wind event into inertial oscillations in the mixed layer is ten times this (0.01 W m^{-2}), so that the vertical energy flux estimated in the observed high-wavenumber NIW is about 10% of the energy flux from the wind into the mixed layer.

Energy loss from NIWs to dissipation

Energy dissipates as the wave travels due to instabilities and wave-wave interactions. Assuming that the wave frequency doesn't change, local dissipation can be estimated from the wave energy equation

$$\frac{\partial E}{\partial t} + (\mathbf{u} \cdot \nabla)E = \nabla \cdot \mathbf{c}_g E + Q_+ + Q_- \tag{2.12}$$

in which E represents energy, $\mathbf{u}$ background velocity (larger length and slower time scales than the internal wave), $\mathbf{c}_g$ the wave group velocity (including both horizontal and vertical component), and Q_+ and Q_- represent local sources and sinks of energy. Making the further simplifying but unrealistic assumptions that there is no local energy input, no net advection of wave energy, and that the only local energy sink is dissipation (no downscale transfer of energy to higher frequencies and wavenumbers), this equation simplifies to

$$\frac{\partial E}{\partial t} \sim \nabla \cdot \mathbf{c}_g E + \varepsilon \tag{2.13}$$

There are two different routes we can take to estimate local dissipation from equation 2.13. First, averaging in depth from 30 to 300 m (the range of the microstructure profiler) and assuming there is no net energy flux in or out of that range we have the balance

$$\frac{\Delta \langle E \rangle}{\Delta t} \geq \varepsilon \tag{2.14}$$

We assume that this is an upper bound on ε as it neglects downscale energy transfer via wave-wave interactions and the advection and radiation of energy. Between yearday 243 and 250, the depth-averaged energy density from 30-300m decreased from approximately 3×10^{-3} m^2 s^{-2} to 1×10^{-3} m^2 s^{-2} (Fig. 2.4a). With $\Delta E = 0.002$ m^2 s^{-2} and $\Delta t = 7$ days $= 6.048\times10^5$ s, we find an upper bound $\varepsilon \leq 4\times10^{-9}$ W kg^{-1}.

As a second approach, we can use equation 2.12 and consider it over a time range when energy is approximately in steady state. This results in an approximate balance between the energy flux divergence and local dissipation,

$$-\nabla\cdot\mathbf{c}_g E \sim \varepsilon \tag{2.15}$$

We make the further assumptions that the vertical group velocity is constant with depth in the WKB stetched and scaled frame, and that the wave only propagates in the vertical (Kunze and Sanford, 1984). With these assumptions, this balance simplifies to

$$\varepsilon \leq c_{gz}\frac{\partial E}{\partial z} \tag{2.16}$$

We again treat this as an upper bound on ε, as there are in fact other sources of energy loss that have been neglected in the assumptions.

In section 4.a.2. we calculated three different estimates of the vertical group velocity c_{gz}. For the first of these, we estimated vertical group velocity directly from HKE. Between 70 and 170 m HKE density decreased from 0.006 m^2 s^{-2} to 0.002 m^2 s^{-2} (Fig. 2.4b), and with an estimated vertical group velocity of 2×10^{-4} m s^{-1} this implies $\varepsilon \leq 8\times10^{-9}$ W kg^{-1}. The time-averaged quantity $c_{gz}\frac{dE}{dz}$ is generally significantly higher than observed dissipation (Fig. 2.10).

We also used two methods to calculate group velocity within an isolated window in which the intrinsic frequency was approximately constant. Corresponding upper bounds for ε can

be estimated by multiplying these group velocities by $\Delta E_{WKB}/\Delta z^*$ within the WKB-stretched window. Within this window, HKE decreases from 0.02 to 0.01 m^2 s^{-2}, for a $\frac{\Delta E}{\Delta z^*}$ of 1.8 $\times 10^{-4}$ m s^{-2}. Multiplying by c_{gz} for the harmonic fit results in an upper bound $\varepsilon \leq 3 \times 10^{-8}$ W kg^{-1}, while using c_{gz} from the ellipse fit results in $\varepsilon \leq 7 \times 10^{-8}$ W kg^{-1}. These are higher bounds than determined from the decay of HKE over the whole time/depth range.

The highest value of ε measured during the MMP survey was 6×10^{-10} W kg^{-1} (30 m depth). This is lower than the upper bounds discussed above by a factor of 3 to 16.

The dispersion relationship can be used to estimate the horizontal wavenumber κ_H and group velocity c_{gH} for these waves. From the dispersion relation,

$$\kappa_H^2 = \frac{m^2(\omega^2 - f^2)}{N^2 - \omega^2} \tag{2.17}$$

and in terms of this wavenumber, the horizontal group velocity is

$$c_{gH} = \frac{N^2 \kappa_H}{m^2 (f^2 + \frac{N^2 \kappa_H^2}{m^2})^{1/2}}. \tag{2.18}$$

Using a frequency $\omega = 1.43 \times 10^{-4}$ rad s^{-1} (consistent with a vertical group velocity $c_{gz} = 2 \times 10^{-4}$ m s^{-1}), the horizontal wavelength is approximately 50 km, with a horizontal group velocity of about 6 km day^{-1}. The difference in scales between the vertical and horizontal group velocities emphasizes that the ε estimates discussed above are upper bounds as horizontal propagation cannot realistically be neglected.

2.4.2 Comparison to lower latitude studies

We observed an event with significant winds and corresponding wind stresses up to 0.25 N m^{-2}. At other latitudes, events of similar magnitude have been observed to both contribute significantly to the internal wave field and to result in elevated local ε (e.g. Alford and Gregg (2001)). Such events are likely to become more common as the Arctic ocean is increasingly

exposed to wind forcing in the summer and early fall. It has been hypothesized that such forcing may cause a feedback effect in which increasing wind energy is transmitted into the deep ocean, increasing background diffusivities and causing a net upwards transport of Atlantic-origin heat.

Historically, sea ice and the associated ice-ocean boundary layer were thought to be the primary factors that limit energy transfer from wind to internal waves in the Arctic. However, observations suggest that in spite of a storm occurring over the ice-free ocean, ε wasn't appreciably elevated below 150 m where it could potentially impact Atlantic Water vertical turbulent heat fluxes. At shallower depths, ε was a factor of 2-3 larger in the survey taken soon after the storm compared to the later survey. There are a number of factors which may make the transfer of wind energy into the deeper stratified ocean especially inefficient in the Arctic relative to lower latitudes even in the absence of persistent sea ice. In this section, we compare each step of the chain of energy transfer from the wind to ocean dissipation and mixing with other latitudes to try to identify the factors that insulate the Atlantic Water from wind-driven mixing even in the absence of sea ice cover.

Energy flux from the wind to the mixed layer

A higher Coriolis frequency f results in relatively smaller near-inertial mixed-layer responses at high latitudes. In general, wind spectra are red, so that keeping the wind spectrum constant while increasing f results in less energy resonant at inertial frequencies (e.g. Mickett et al. (2010)). Using the same mixed layer depth $H = 15$ and damping $r = 0.005f$, as well as the same winds, running a slab model at 45 °N rather than 72 °N results in twice as much power input into the mixed layer (Table 2.2). This effect is even more pronounced if the same model is applied at 4 °N. This is an unrealistic comparison, as wind fields, mixed layer depth, and local dissipation are not independent of latitude. However, it conceptually isolates the effect of latitude on the slab model from these other factors.

There are a number of other factors which may affect the efficiency of energy transfer

from the wind to the mixed layer. Chief among these is the frequency distribution of storm-driven wind forcing. In the northern hemisphere, it is the clockwise near-inertial component of the wind forcing that stimulates the mixed layer response. An analysis of how the projection of wind forcing onto the inertial frequency varies with latitude is made complicated by scare high latitude measurements, and is beyond the scope of this paper. However, it is possible that the spatial and temporal scales of Arctic storms are less resonant with the local inertial frequency than their lower latitude counterparts.

Energy flux in the NIW field

Based on slab model estimates of the energy flux from the wind to the ocean and estimates for the energy flux within the observed high mode NIW field, we estimate the vertical energy flux within the NIW field only accounts for 10% of the modeled energy flux from the wind into the mixed layer. Other studies estimate 12-33% of the wind energy that excites inertial oscillations in the mixed layer penetrates the stratified ocean as NIWs (Furuichi et al., 2008; Alford et al., 2012). These studies are not exactly comparable to the current analysis, as the Alford et al. (2012) figure is an estimate of the NIW energy that penetrates to 800 m at Station Papa over the course of a year (excluding low mode internal waves that cannot be detected from mooring data), while the Furuichi et al. (2008) estimate is derived from a model and examines the portion of energy that propagates below 150 m. Given the uncertainties associated with the slab model, the NIW energy flux estimates, and the relatively short data record, our 10% estimate is not necessarily inconsistent with these previous studies. However, the actual energy flux from the wind to the ocean is likely higher, as the slab model estimates from the NCEP CFSv2 wind product are biased low due to the lack of near-inertial variability in the reanalysis product.

What happens to energy that enters the mixed layer but doesn't appear in the observed NIW field? There are many options. Mixed layer energy is quickly transferred to potential energy in the form of hydrostatic pressure perturbations as a result of convergence and divergence within

the mixed layer. These pertubations drive deep velocities that cannot be observed by the mooring instruments. Energy also radiates horizontally from the forcing site, and can dissipate locally in the mixed layer or be converted to potential energy as a result of mixing that deepens the mixed layer. In the Arctic ocean, there are multiple effects that may conspire to limit the energy carried by the high-mode NIWs that have the potential to access the Atlantic Water halocline.

NIWs are generated when mixed layer inertial oscillations result in zones of convergence and divergence. These zones exist due either to the spatial scales and translation speeds of wind events, the spatial scales of oceanic surface eddy kinetic energy, or to the length scale set by the rate of variation of the Coriolis frequency f (Gill, 1984; D'Asaro, 1989). The rate of varation of $f = 2\Omega sin(\theta) \approx f_0 + \beta y$ with latitude (that is, β) is low towards the poles. At 72 $^\circ$ N, $\beta = 7.04 \times 10^{-12}$ rad m^{-1} s^{-1}, compared to 1.61×10^{-11} rad m^{-1} s^{-1} at 45 $^\circ$ N and 2.27×10^{-11} rad m^{-1} s^{-1} at 4 $^\circ$ N. This corresponds to less convergence and divergence due to wind-driven inertial oscillations, resulting in small horizontal wavenumbers and shallow energy ray paths. This has the effect of inhibiting downward propagation of energy.

The spatial scales of both the wind and surface eddy kinetic energy fields may also be quite different in the Arctic than at lower latitudes. The Rossby radius of deformation in the Arctic is much smaller than at midlatitudes [$\mathcal{O}$(10 km)] and ice patchiness can contribute to spatial variability. Both of these effects may tend to counteract the larger length scales set by β, but the relative importance of these factors is not well understood.

Another factor that may play a role in limiting energy flux into the NIW field, particularly during the ice-free summer, are shallow mixed layers with sharp stratification. The depth of the mixed layer determines the modes into which energy is transfered. A deeper mixed layer results in energy transfer to lower modes with lower vertical wavenumbers, while a shallower mixed layer transfers energy to higher modes and higher vertical wavenumbers (Gill, 1984). Group velocity scales inversely with vertical wavenumber, so that NIWs waves with higher vertical wave numbers travel more slowly. This slower group velocity may result in more dissipation before

NIWs have the opportunity to propagate appreciable distances into the stratified ocean below.

The combination of a relatively shallow ray path induced by low β and high stratification at the base of the mixed layer and slow group velocity due to shallow mixed layers may result in energy propagation that is largely horizontal rather than vertical, so that NIWs are may either dissipate at shallow depths or reach continental slopes rather than propagate into the Atlantic Water. Experiments performed by running a version of the Gill (1984) near-inertial wave model at 75 °N suggests that both the low value of β and the effects of shallow mixed layers contribute to reducing the vertical propagation of energy carried in wind generated NIWs (J. Guthrie, personal communication 2019).

Energy transfer from internal waves to dissipation

The finescale parameterization estimates ε based on large scale shear and strain due to the internal wave field. In the global ocean, it is generally successful to within a factor of 2-3 (Whalen et al., 2015). In the next section, we compare observed ε with finescale parameterization estimates and discuss possible explanations for observed discrepancies.

2.4.3 Agreement and discrepancies between microstructure measurements and finescale parameterizations

Above 200 m, the time-averaged finescale parameterization estimates of ε are within a factor of two of the time-averaged observed values within each microstructure survey over the corresponding depth ranges. However, at 200 m and deeper, finescale parameterizations underestimate observed rates of ε by approximately a factor of 10. In the 200 m bin, the shear spectrum is only 40% as energetic as in the 150 m bin. In general, ε varies as S^4 (Gregg, 1989), so this weak shear explains the order of magnitude reduction in ε_{fs} between the 150 m and 200 m bin. However, ε inferred from microstructure measurements does not drop off to the same degree

in this depth range. At 200 m, the density ratio becomes unstable to double diffusive convection as the Atlantic Water halocline begins (Fig. 2.2c). Although double diffusive convection results in different small-scale physics than shear-driven turbulence, fitting Panchev spectra to shear variance still effectively calculates ε (Inoue et al., 2007; St. Laurent and Schmitt, 1999). However, it is uncertain whether the assumptions that go into the finescale parameterization hold in regimes that are unstable to double diffusion. The internal wave field still carries some energy, but it is weak below 200 m and the mechanics of its downscale transfer may be quite different than in regions with doubly stable stratification. This discrepancy between the finescale parameterization and observed values occurs even in the absence of characteristic double diffusive staircases, indicating that caution must be used applying finescale parameterizations in double diffusive regimes even when apparent staircases are not present.

Although this parameterization used measurements of both shear and strain, assuming a constant $R_\omega = 3$ only results in factor of two changes in ε_{fs}, suggesting that measuring just one of these quantities would be largely sufficient to characterize dissipation due to internal waves. This is true even for the high R_ω values associated with the presence of NIWs.

2.4.4 Observed ε, vertical heat fluxes, and significance

Observations suggest dissipation rates of $\sim 3 \times 10^{-10}$ W kg^{-1} between 50 and 150 m during the period that the NIW passed by, with maximum rates at 30 m of $\sim 6 \times 10^{-10}$ W kg^{-1}. In the survey during the NIW event, ε was elevated by a factor of 2-3 in this depth range relative to the survey after the NIW event. These values are consistent with the upper bounds on ε estimated from features of the wave field [$O(10^{-9}$ m^2 s$^{-3})$]. An internal wave with initial energy density of 0.0025 m^2 s^{-2} exposed to dissipation rates of 6×10^{-10} W kg^{-1} for the two weeks it would take to propagate to 200 m depth loses 30 % of its energy. This suggests that significant internal wave energy dissipates above the heat stored in the Atlantic Water mass. Observations show a very weak wave field below $\sim$ 150 m, consistent with the hypothesis that most of the energy that

propagates out of the mixed layer dissipates well above the Atlantic Water. These results are also consistent with studies by Lincoln et al. (2016), Guthrie et al. (2013), and Lique et al. (2014), all of which found that a decline in sea ice cover has not been associated with elevated mixing at the intermediate depths where Atlantic Water is found in the western Arctic ocean.

Even immediately following a wind event and ensuing NIWs, observed heat fluxes out of the Atlantic water were minimal (less than 0.05 W m^{-2}). For reference, vertical heat fluxes due to double diffusive convection above the Atlantic Water generally range from 0.05-0.3 W m^{-2} (Timmermans et al., 2008b). Diffusivities and heat fluxes were slightly elevated in the upper ocean ($<$100 m depth) following the NIW event compared to the later survey. The vertical gradient of temperature varied rapidly in this region due to filaments of PSW. However, the average temperature profile was warmer at the top and cooler at the bottom, resulting in downwards net heat fluxes rather than upwards.

There is significant variability in the mean thermal gradients above 200 m in the western Arctic, and NIW forcing may cause epsiodic upwards heat fluxes above NSTM or warm PSW filaments under certain conditions. The Arctic is also undergoing rapid climate change. Significant alteration to the Arctic Ocean stratification could allow more efficient transfer of energy into the deep ($>$200 m) ocean. For instance, a longer ice-free season with more ice-free sea surface increases the fetch that drives surface waves during late summer and autumn storms (Thomson and Rogers, 2014). Larger surface waves may act to deepen the mixed layer, resulting in more efficient NIW energy transfer into the water column.

Rapid climate change in the Arctic Ocean has resulted in temporally prolonged and spatially expanded seasonally ice-free regions. Currently, many factors conspire to preserve low mixing rates even in ice-free conditions, insulating the heat stored in the deep Atlantic Water. However, these factors themselves may be altered as the climate continues to change, and many questions remain.

Table 2.1: Results of a finescale parameterization using moored profiler shear and strain data. The range within a standard deviation of the mean is given in parentheses. Means of ε are calulated geometrically.

Depth range (m)	$\langle R_\omega \rangle$	$\langle \varepsilon \rangle$ (W kg^{-1})
75-150	10 (0.1 to 20)	1×10^{-10} (3×10^{-11} to 4×10^{-10})
100-200	19 (12 to 26)	2×10^{-10} (2×10^{-10} to 4×10^{-10})
150-250	3 (1 to 4)	5×10^{-11} (2×10^{-11} to 1×10^{-10})
200-300	3 (2 to 4)	6×10^{-11} (3×10^{-11} to 1×10^{-10})

2.5 Acknowledgments

This work was supported by NSF grants PLR 14-56705 and PLR-1303791 and by NSF Graduate Research Fellowship grant DGE-1650112. The hourly NCEP CFSv2 model data are made available by NCAR (https://rda.ucar.edu/datasets/ds094.1/). The Arctic Ocean Tidal Inverse Model (AOTIM-5) data are made available by the Earth & Space Research Institute (ESR; https://www.esr.org/research/polar-tide-models/list-of-polar-tide-models/aotim-5/).

We gratefully acknowledge the *Sikuliaq* captain and crew, MOD engineering team, and ArcticMix collaborators who made this study possible. We are additionally grateful to Mike Gregg, Tom Weingartner, John Guthrie, Jim Thomson, Justin Stopa, Peter Winsor, Harper Simmons, Mary-Louise Timmermans, Yueng-Djern Lenn, Rob Pinkel, Laurie Padman, and Joe Metzger for scientific support and insight; and to Mike Gregg and Dave Winkel for supporting the transition of the MMP instrumentation from APL/UW to SIO.

Microstructure data are available for download at https://microstructure.ucsd.edu. Mooring data is available from the authors upon request.

Chapter 2, in full, is being prepared for submission for publication. Fine, Elizabeth; Alford, Matthew H.; MacKinnon, Jennifer A.; Mickett, John B. The dissertation author was the primary investigator and author of this paper.

Table 2.2: Slab model output using CFSv2 wind forcing from the mooring location on yeardays 240-242, H = 15, and r = 0.05f at varying latitudes. Standard deviations of mean quantities are given in parentheses.

Latitude (° N)	|Wind Stress| (N m^{-2})	Energy Flux (W m^{-2})
72	0.1 (0.05)	0.01 (0.007)
45	0.1 (0.05)	0.02 (0.01)
4	0.1 (0.05)	0.3 (0.2)

Table 2.3: Summary of energy flux and ε estimates

Flux from wind to ocean mixed layer	10^{-2} (3×10^{-3} to 2×10^{-2}) W m^{-2}
NIW field energy flux	10^{-3} (9×10^{-4} to 2×10^{-3}) W m^{-2}
NIW field ε from	
.....microstructure measurements (30 m)	6×10^{-10} (3×10^{-10} to 1×10^{-9}) W kg^{-1}
.....microstructure measurements (75-150 m)	3×10^{-10} (2×10^{-10} to 6×10^{-10}) W kg^{-1}
.....finescale parameterization (75-150 m)	1×10^{-10} (3×10^{-11} to 4×10^{-10})
..... $\frac{\Delta E}{\Delta t}$	$\leq 4\times10^{-9}$ W kg^{-1}
..... $\frac{\partial E}{\partial z}c_{gz}$	$\leq 8\times10^{-9}$ W kg^{-1}

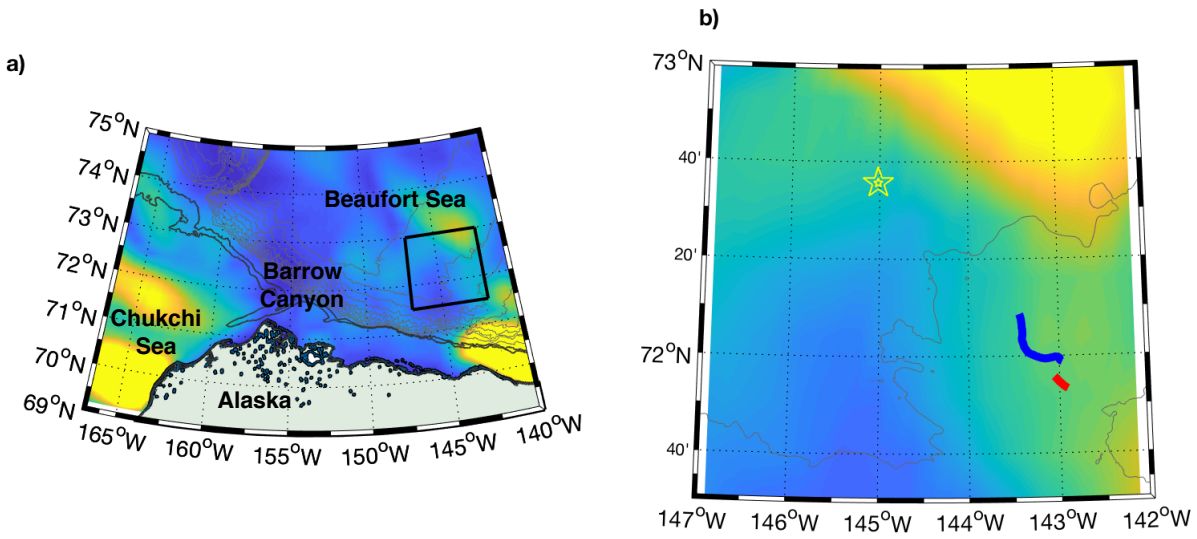

Figure 2.1: Map of the study region. Colors show the maximum energy flux from the wind to the ocean mixed layer calculated from a slab model using 10 m CFSv2 winds on between yearday 240-243 in mW m^{-2}. a) Regional map, study area is highlighted in black box b) Study area. Mooring is shown as a star. First and second microstructure survey locations are shown as blue and red lines, respectively.

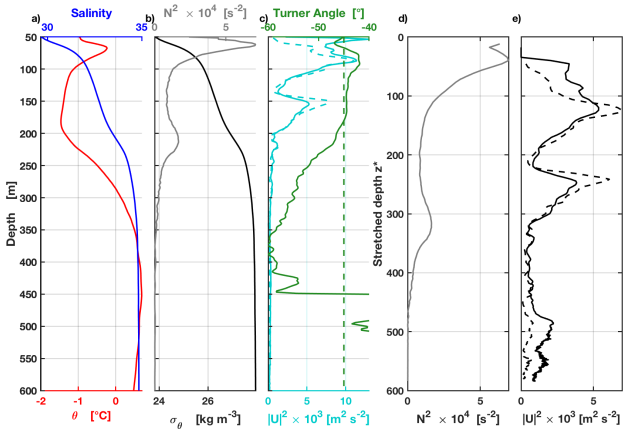

Figure 2.2: Average profiles over the profiler record duration of a) Potential temperature (red), salinity (blue) b) σ_θ (black) and N^2 (gray) c) $|U|^2$ (cyan, with NIW filtered $|U_{NI}|^2$ dashed) and Turner angle (green). The Turner angle is calculated using gradients of temperature and salinity calculated as first differences over 2 m bins, then smoothed over 8 m. The dashed green line indicates Tu = -45°, the boundary between double diffusive convective instability and doubly stable stratification. WKB stretched and scaled quantities averaged over the profiler record: d) N^2_{WKB} and e) $|U_{WKB}|^2$ (with NIW filtered $|U_{WKB,NI}|^2$ dashed).

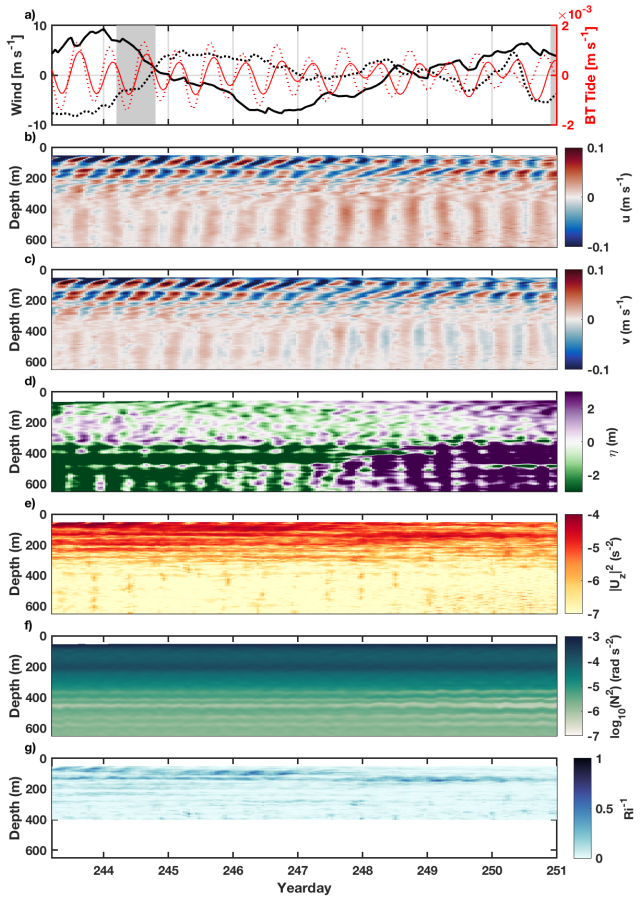

Figure 2.3: a) 10 m wind velocity from CFSv2 reanalysis product (black; east-west solid, north-south dotted) and barotropic tidal velocity from Arctic Ocean 5 km Inverse Model (AOTIM-5) (red; east-west solid, north-south dotted), with the timing of the two MMP surveys shaded in gray, b) u velocity (m s^{-1}), c) v velocity (m s^{-1}), d) isopycnal displacement η (m), e) $|\mathbf{U_{z20m}}|^2$ (s^{-2}), f) N^2_{20m} (rad s^{-2}), g) Ri^{-1}_{20m} from $|\mathbf{U_{z20m}}|^2$ and N^2_{20m}. Ri^{-1}_{20m} is masked below 400 m as noise in shear and variations in N^2 due to double diffusive layers dominate the signal below this depth. All observations made by the mooring profiler.

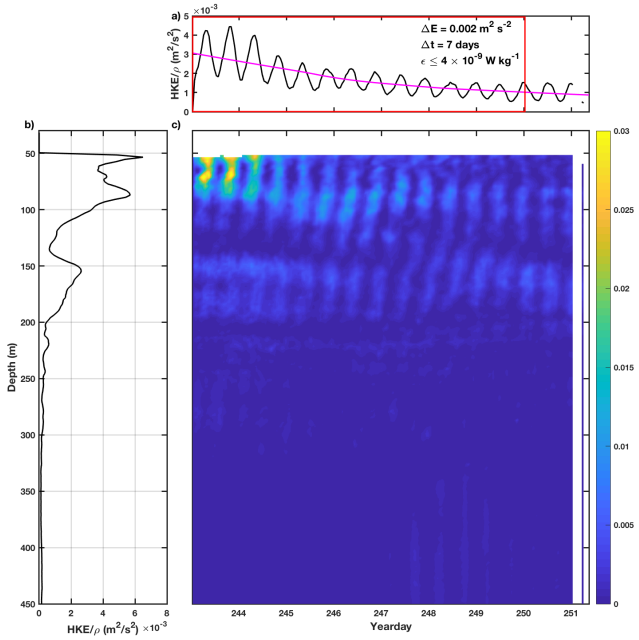

Figure 2.4: a) Depth-averaged from 30 to 300 m and b) Time-averaged over the profiler record c) horizontal kinetic energy calculated from profiler velocities. The period used to determine an upper bound on ε due to the dissipation of the NIW is highlighted in red in a)

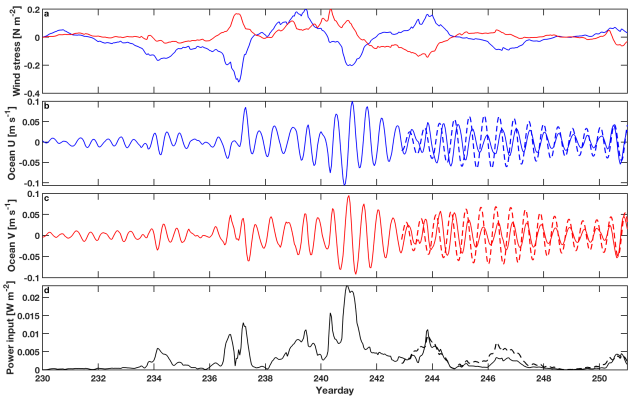

Figure 2.5: a) Wind stress input for slab model, based on CFSv2 10 m winds and assuming no ocean velocity. Blue and red represent east-west and north-south stress, respectively. b) East-west mixed layer velocity from slab model. Dashed line represents measured 15 m velocity filtered at the near-inertial frequency. c) As in b, but for north-south mixed layer velocity. d) Power input from the slab model calculated as $\tau \cdot \mathbf{u}$ The dashed line represents $\tau \cdot \mathbf{u_{obs}}$, where $\mathbf{u_{obs}}$ is the observed 15 m velocity filtered at the near-intertial frequency, and τ is calculated from reanalysis winds.

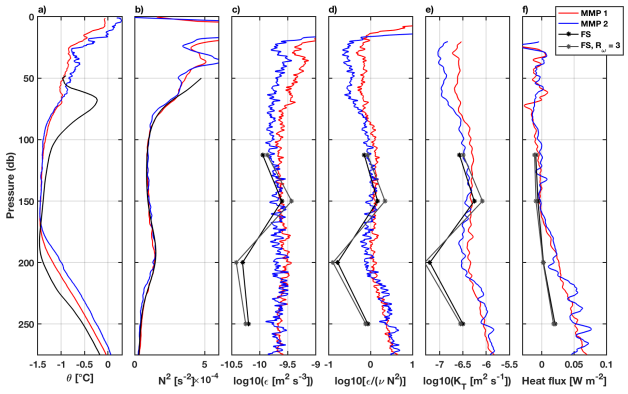

Figure 2.6: Quantities averaged over MMP surveys one (red) and two (blue), and averaged over the profiler record using finescale parameterization (black): a) Potential temperature, b) N^2, c) ε, d) Re_b, e) K_T, and f) heat flux. Black stars represent finescale estimates calculated using both shear and strain profiler measurements to calculate R_ω *in situ*, while gray stars are calculated using $R_\omega = 3$.

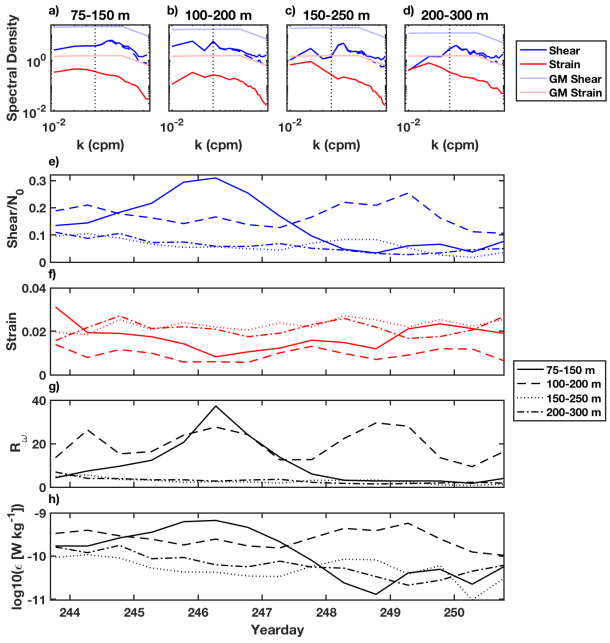

Figure 2.7: Top: Average normalized shear (blue) and strain (red) spectra for depth bins a) 75-150 m b) 100-200 m c) 150-250 m and d) 200-300 m. Light blue and red lines are the Garret-Munk 1976 shear and strain spectra for each depth bin. Normalized shear spectra uncorrected for roll-off are shown as dotted lines. The wavenumber cutoff $k_c = 0.04$ m^{-1} used for integration is shown as a dotted black line. Bottom: Time-series plots for 12 hour finescale estimates of e) normalized shear, f) strain, g) *in situ* R_ω, and $\log_{10}(\varepsilon_{fs})$ for all depth bins. Line style indicates depth bins, with the 75-150 m depth bin solid, 100-200 m dashed, 150-250 m dotted, and 200-300 m dash-dot.

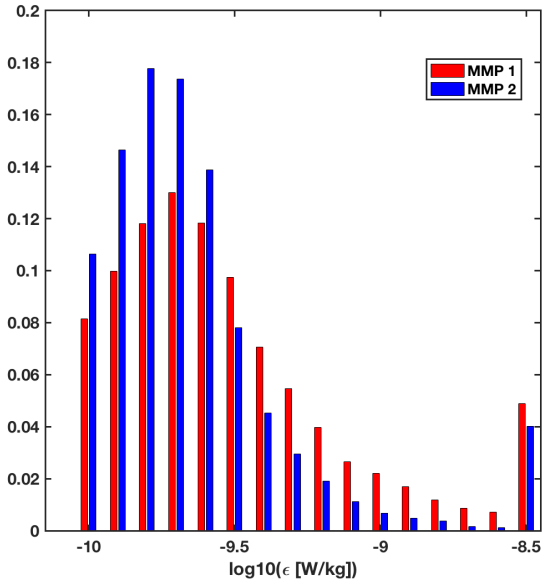

Figure 2.8: Histograms of ε measured during MMP surveys 1 (red) and 2 (blue). The instrument noise floor is 1×10^{-10} W kg^{-1}, and values are capped there. In both surveys there are peaks in the distribution between 1 and 3 $\times 10^{-10}$ W kg^{-1}, suggesting that observed patterns are physically meaningful, if subject to overestimation.

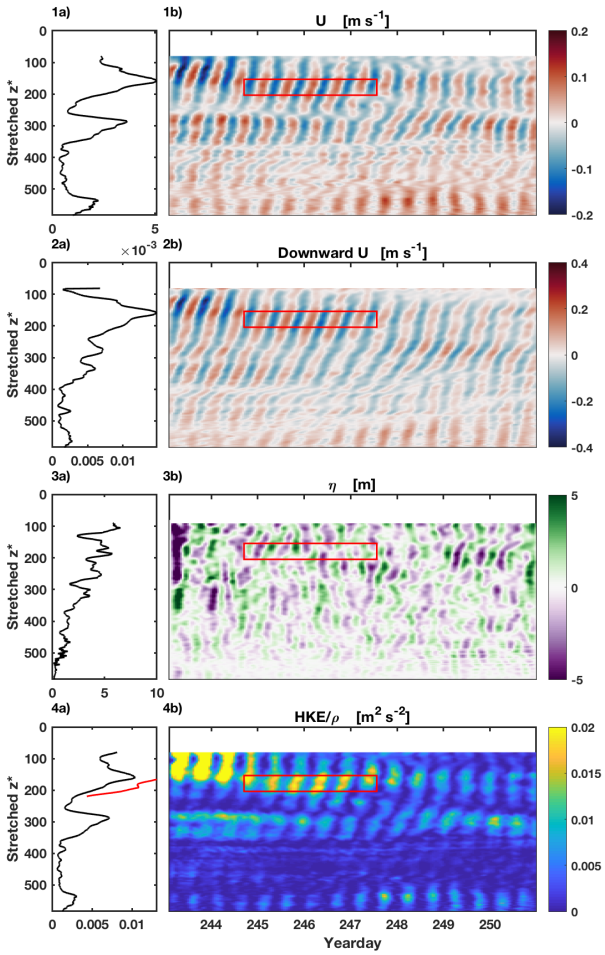

Figure 2.9: WKB stretched, scaled, and lowpass filtered 1a) time-averaged u amplitude ($m^2\ s^{-2}$), 1b) u velocity ($m\ s^{-1}$), 2a) time-averaged rotary-filtered downward propagating velocity amplitude ($m^2\ s^{-2}$), 2b) rotary-filtered downward propagating velocity ($m\ s^{-1}$) 3a) time-averaged isopycnal displacement amplitude η^2 (m), 3b) η (m), 4a) depth-averaged rotary-filtered downward propagating horizontal kinetic energy density (u^2+v^2), and 4b) rotary-filtered downward propagating horizontal kinetic energy density (u^2+v^2). The segment used for fitting to find the internal wave frequency from yearday 244.5 to 247 and scaled depth 165 to 220 m is shown in a red box in each hovmoller plot. The red line in 4a) is the time-average of downward propagating HKE density within that segment.

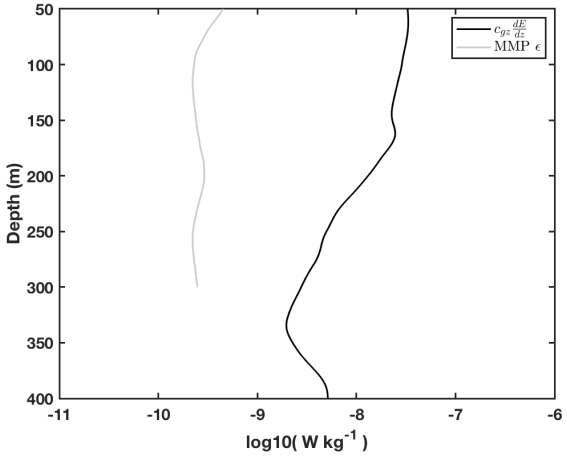

Figure 2.10: The time-averaged vertical derivative of energy flux, calculated as $c_{gz}\frac{dE}{dz}$, with $c_{gz} = 2 \times 10^{-4}$ m s^{-1} and $\frac{dE}{dz}$ smoothed over 100 m. The quantity $c_{gz}\frac{dE}{dz}$ is calculated in WKB coordinates, then put onto scaled coordinates (F_z is invariant under the WKB transform). Observed values of ε averaged over the MMP survey on yearday 244 are plotted for reference.

Chapter 3

Microstructure Observations of Turbulent Heat Fluxes in a Warm-Core Canada Basin Eddy

3.1 Introduction

In the last decades Arctic sea ice has declined at an alarming rate, and this loss is expected to continue in the coming years (Carmack et al., 2015; Overland and Wang, 2013). Ocean heat fluxes have been known to contribute to the growth/melt cycle of Arctic sea ice since the 1970s (Maykut and Untersteiner, 1971); however, the pathways by which oceanic heat reaches Arctic sea ice are complex and our knowledge is constrained by a lack of *in situ* observations (Carmack et al., 2015). Global climate model predictions have historically underestimated the rate of sea-ice melt (Eisenman et al., 2011); better knowledge of the processes that bring oceanic heat into contact with sea ice is needed to improve both regional and global model predictions.

Heat can be stored in subsurface water masses in the Arctic Ocean because salinity is much more influential than heat in setting the density of water near the freezing temperature. In

the western Arctic, the relatively warm Pacific Summer Water (PSW) and Atlantic Water (AW) masses are found between 40-100 m and 200-400 m depth, respectively. PSW originates with flows through the Bering Strait, driven by the pressure gradient associated with the higher sea level in the Pacific than in the Arctic. In the summer, these flows are further modified in the Chukchi Sea, developing into two varieties of PSW (Rudels, 2001). These are the relatively warm fresh Alaskan Coastal Water (ACW) and somewhat colder and saltier summer Bering Sea Water (sBSW) (Shimada et al., 2001; Pickart et al., 2005; Timmermans et al., 2014). ACW is modified by inflow from Alaskan rivers and is identified by a temperature maximum in a salinity range of 29-32.2, while sBSW is modified in the Bering Sea and identified by a temperature maximum in the salinity range of 32.2-33 (Timmermans et al., 2014). The lateral distribution of PSW is thought to play a role in regulating the extent of sea ice (Shimada et al., 2001, 2006; Steele et al., 2004; Pickart, 2004; Woodgate et al., 2010; Watanabe, 2011) although the mechanism for heat flux from PSW to the surface is unclear in the Canada Basin, where PSW is generally found more than 50 m from the surface and is usually separated from the mixed layer by strong haloclines (Toole et al., 2010). Prior studies suggest that while Atlantic-origin water contains more subsurface heat than PSW, stratification allows only very modest heat fluxes out of the Atlantic Layer in the western Arctic (Padman and Dillon, 1987; Timmermans et al., 2008a; Sirevaag and Fer, 2012; Lincoln et al., 2016).

Eddies are ubiquitous in the Arctic and are frequently observed by both ships and drifting platforms (Hunkins, 1974; Newton et al., 1974; Manley and Hunkins, 1985; D'Asaro, 1988b; Padman et al., 1990; Plueddemann et al., 1998; Münchow et al., 2000; Muench et al., 2000; Krishfield et al., 2002; Halle, 2003; Pickart et al., 2005; Pickart and Stossmeister, 2008; Timmermans et al., 2008b; Kadko et al., 2008; Kawaguchi et al., 2012; Zhao et al., 2014; Bebieva and Timmermans, 2015; Pisareva et al., 2015; Kawaguchi et al., 2016). Intrahalocline eddies in the western Arctic are thought to form due to instabilities at the mouth of Barrow Canyon (D'Asaro, 1988a; Shaw and Chao, 2003; Watanabe, 2011) and along the Beaufort and Chukchi slope currents (Hunkins,

1974; Manley and Hunkins, 1985; Muench et al., 2000; Chao and Shaw, 2003; Pickart, 2004; Pickart et al., 2005; Spall et al., 2008; Watanabe, 2011). As they make their way into the Canada Basin, such eddies may play an important role in the transport and modification of Pacific-origin Arctic water masses (D'Asaro, 1988a; Steele et al., 2004; Pickart, 2004; Pickart et al., 2005; Pickart and Stossmeister, 2008; Spall et al., 2008; Watanabe, 2011).

In this paper, we describe an anomalously warm anticyclonic eddy observed on the Chukchi slope in September of 2015 (Fig.3.1 and 3.2). The core of this eddy was quite warm (6 $^{\circ}$C) and close to the surface (40 m). This is significantly warmer than most previously described Arctic eddies (Manley and Hunkins, 1985), although Kawaguchi et al. (2012) observed an eddy with similar properties in 2010. The core of the warm eddy had similar temperature-salinity properties to ACW (see section 3). Warm ACW enters the central Canada Basin via Barrow Canyon (D'Asaro, 1988b; Münchow and Carmack, 1997; Steele et al., 2004; Shroyer, 2012), where it divides into the baroclinically unstable Beaufort shelfbreak jet (Rudels, 2001; Steele et al., 2004; Pickart, 2004; Nikolopoulos et al., 2009; von Appen and Pickart, 2012) and Chukchi slope current (Corlett and Pickart, 2017). Warm-core eddies likely form due to instabilities either at Barrow Canyon or along the topographically trapped currents. These warm and salty Chukchi slope eddies are somewhat analogous to the small warm and salty Mediterranean eddies ("meddies"), which have been described since the 1980s (Armi and Zenk, 1984; Armi et al., 1989; Ruddick, 1992; Ruddick et al., 2010). Warm ACW eddies could play a significant role in the transport of Pacific-origin freshwater, nutrients, and heat into the Arctic Basin, which could play a role in setting stratification, affect biological productivity, and impact the growth/melt of sea ice.

In the following analysis we focus primarily on the processes that remove heat from the eddy's core. Our goal is twofold: to identify the processes that cause heat flux out of the eddy observed in September 2015, and to quantify the net heat flux due to these processes. Our analysis indicates that the following three processes act to extract heat from the eddy (in order of increasing importance): (1) shear-driven mixing; (2) double diffusive layering; and (3) net

lateral heat fluxes along the flanks of eddies. Here we briefly introduce the candidate processes. In section 3.b.1 we present the evidence that these processes are active in the eddy, and in section 3.b.2 we consider their respective contributions to heat flux.

Shear-driven mixing When the shear within a flow is high relative to local stratification, instabilities may occur, resulting in overturns and turbulent mixing. Shear is elevated above and below the core of an eddy due to its rotation. Smaller-scale variation in shear may be due to the effects of internal waves, which are primarily driven by winds and tides. Mixing due to shear-driven turbulence has been observed to play an important role in setting heat fluxes in the Eurasian Arctic (Fer et al., 2010; Peterson et al., 2017; Meyer et al., 2017); however shear is generally low in the western Arctic due to weak tides and modest wind-forced near-inertial waves (D'Asaro and Morehead, 1991; D'Asaro and Morison, 1992; Pinkel, 2005; Fer, 2009).

Double diffusive convection (DDC) DDC is a common phenomenon in the Arctic Ocean (Neshyba et al., 1971; Melling et al., 1984; Padman and Dillon, 1987, 1988, 1989, 1991; Kelley et al., 2003; Sundfjord et al., 2007; Lenn et al., 2009; Timmermans et al., 2008a; Polyakov et al., 2012; Sirevaag and Fer, 2012; Kawaguchi et al., 2012, 2014; Bebieva and Timmermans, 2015; Guthrie et al., 2015; Bebieva and Timmermans, 2017) and has previously been observed above warm-core Arctic eddies (Padman and Dillon, 1991; Padman, 1994; Bebieva and Timmermans, 2015; Kawaguchi et al., 2012) and PSW intrusions (Kawaguchi et al., 2014). DDC occurs when gravitationally stable cold and fresh water overlies a warm and salty layer. At a molecular level, heat diffuses upwards faster than salt, leading to rising buoyant parcels. As a parcel rises, heat diffuses out of it faster than salt, so that its buoyancy decreases. The parcel may initially overshoot its neutral density due to inertia, resulting in damped oscillatory behavior. Over time, this process results in well-defined convecting cells which are separated by thin interfaces where the cells meet. Fluxes of both heat and salt are generally continuous through layers and interfaces, but within the convecting layers both temperature and salinity are relatively uniform while across the interfaces there are sharp gradients in both temperature and salinity. This results in a characteristic staircase

apparent in vertical profiles of temperature, salinity, and density. DDC steps are ubiquitous in the Canada Basin above the Atlantic Layer, but estimates of heat flux through them are fairly low, with an estimated range of 0.05-0.3 W m^{-2} (Timmermans et al., 2008a).

Lateral heat fluxes Thermohaline intrusions occur where warm and salty water lies laterally next to cold and fresh water and are observed frequently throughout the world's oceans. These intrusions result in a net flux of heat and salt from the warm salty side of the front (Turner, 1978; Ruddick and Richards, 2003). Thermohaline intrusions have been observed at the edges of warm and salty Mediterranean eddies (meddies), where they dominate the decay of meddies' heat signature and density anomaly (Armi et al., 1989; Ruddick, 1992; Ruddick et al., 2010). Similar intrusions have frequently been observed in the Arctic Ocean (see Ruddick and Richards (2003) for a review).

All three of these processes are known to occur in the Arctic, and the warm-core intrahalocline eddy described below contained regions in which each of them dominated local heat fluxes. However, the relative importance of these processes in the overall decay of warm intrahalocline eddies (or, more generally, subducted PSW) is not well understood, nor are the heat fluxes associated with each process. In the sections that follow, we describe the methods used to observe the eddy and outline the eddy's observed structure and properties. We describe the features that indicate the presence of different mixing processes and quantify the heat flux from the eddy's core due to each. Finally we compare the relative importance of these processes and quantify the net heat transport out of the eddy's top, bottom, and sides.

3.2 Methods

The observations discussed in this paper were taken aboard the R/V *Sikuliaq* on the Chukchi slope in September of 2015. The survey was conducted just north of the mouth of Barrow Canyon at 72° 23.17' N, 154° 10.80' W. The first survey consisted of four Shallow Water

Integrated Mapping System (SWIMS) transects, shown as solid lines in Fig. 3.1, and two Modular Microstructure Profiler (MMP) lines, shown as dashed lines in Fig. 3.1. Intermittent gaps in the MMP profiling occurred due to the MMP cable freezing to its reel. The number of profiles and speed during each transect are given in Table 3.1.

The observations discussed herein were obtained using two instruments both built by M. C. Gregg at APL/UW and modernized and currently operated by our group at SIO: the Shallow Water Integrated Mapping System (SWIMS) and the Modular Microstructure Profiler (MMP) (Gregg and Pratt, 2010; Wesson and Gregg, 1994). SWIMS is a profiler that is towed behind a ship. It is rapidly winched up and down, making a tight sawtooth pattern. During the portions of this survey conducted using SWIMS, the ship maintained a speed of approximately 2 m s^{-1}, or 4 kts, over ground. Profiles (both up- and down-casts) were made to 150 m depth roughly every 100 seconds, corresponding to a horizontal resolution of $\sim$200 m. SWIMS carries a Seabird 9plus CTD, upward- and downward-looking 300 kHz RDI workhorse ADCPs, an optical backscatter sensor, an oxygen sensor, a fluorometer, and an altimeter for work near the sea floor. Only CTD and ADCP data were used in the present study. Velocities were converted from relative to absolute values by vertically integrating shear and referencing the resulting velocities to a hull-mounted shipboard sonar. The CTD dataset used in this analysis was vertically gridded to 0.5 m bins, while the velocity dataset was gridded into 2 m bins. Velocities were determined to be unreliable within 20 m of the surface, due to the ship wake and reflection from the surface; values in these depth bins are not reported.

MMP is a loosely tethered microstructure profiler. It falls at $\sim$0.6 m s^{-1} and has two custom-built shear probes, an FP07 thermistor, CTD, and altimeter. The turbulent kinetic energy (TKE) dissipation rate (ε) was calculated from microscale shear measurements using an iterative process to fit a Panchev curve to the shear spectra, assuming isotropic turbulence (see Wesson and Gregg (1994)). The dissipation rate of thermal variance (χ) was inferred from the FP07 assuming isotropic turbulence. Both ε and χ were windowed into 2.5 second segments (corresponding

to 1-2 m in depth) prior to spectral analysis. Generally, $\chi = 6\kappa_T < \theta_z^2 >$, in which κ_T is the molecular diffusivity of heat, and $< \theta_z^2 >$ is the variance of the thermal gradient. The fall rate of the MMP is too high to fully resolve the Batchelor spectra of the microstructure temperature gradients, so χ was inferred iteratively (Luketina and Imberger, 2001). In each window, an initial estimate of χ was calculated by integrating the spectrum of θ_z. Maximum likelihood estimation (MLE) was used with this χ estimate to determine the Batchelor wavenumber (k_B) (Ruddick et al., 2000). A revised estimate of χ was calculated from this k_B, and the process iterated until subsequent χ estimates were within 20% of the previous value. Due to the presence of sub-meter-scale structure in temperature, χ is very sensitive to the method of selection of spectral windows, with poorly selected windows introducing factor of 1000 errors into calculated χ. The procedure used to window χ is discussed in more detail in Appendix A. The nominal noise floors for ε and χ are 10^{-10} W kg^{-1} and 10^{-10} $^{\circ}$C^2 s^{-1}, respectively. All MMP data were gridded to 0.25 m depth bins except where otherwise noted. For flux calculations, all quantities were smoothed in the vertical to 1 m. Bulk lateral thermal gradients were additionally smoothed laterally over 1 km.

Due to the lognormal distribution of ε and χ (e.g., Gregg et al. (1993)), sampling errors in both directly measured quantities and calculated fluxes were determined using a bootstrapping procedure. The sampling errors in ε and χ were the largest source of quantifiable error in our calculated heat fluxes, and were generally within 50% of the measured values. However, we cannot quantify errors due to instrument bias or violations of the assumptions inherent in the methods used to calculate heat flux, which likely have a bigger contribution to the uncertainties in mean quantities (e.g., Peters et al. (1988) report uncertainties of a factor of 2-3 in measured ε and χ). All reported values are only accurate within a factor of 2-3, and for this reason, only one significant figure is reported for heat flux calculations.

3.3 Results

3.3.1 Eddy structure

CTD and ADCP data collected during the SWIMS transects indicate the eddy was an anticyclonic warm-core intrahalocline eddy, with core temperatures of 6 °C (Fig. 3.1, 3.2, 3.3). This is an exceptionally warm eddy for the Canada Basin, as most observed warm-core eddies reach temperatures of 1-2 °C (Manley and Hunkins, 1985; Pickart and Stossmeister, 2008; Zhao et al., 2014). The eddy is warmest between 30-50 m depth, with a warm anomaly observed as deep as 95 m (Fig. 3.2).

Temperature and salinity measured in transects T1-T4 show a warm salty core (30-50 m) that was fairly homogeneous, although each transect captured different sections of this core (Fig. 3.3). Beneath this core, temperature decreased slowly, with the 3 °C isotherm extending as deep as 75 m. In T3 and T4, a secondary warm anomaly appeared next to the eddy, likely part of an arm that extends off the eddy core. The salinity in the core of the eddy ranged from 31 to 31.5, which is within the salinity range for Alaskan Coastal Water (ACW) (Timmermans et al., 2014). The velocities measured are consistent with anticyclonic rotation (keeping in mind that most transects did not bisect the center of the eddy). The rotation of the eddy was apparent far beneath its warm core, with velocity signals extending as deep as 250 m, the deepest measurement (not shown). However, the warm core of the eddy from 30 to 50 m showed intensified velocities that were laterally offset from the rotation in the deeper portion of the water column.

Composite eddy features were determined by binning each measurement into overlapping 500 m bins based on radial distance from the eddy's center. To determine the eddy's center, all measurements were backtracked based on the average barotropic velocity during the survey of 4 cm s^{-1} N and 6 cm s^{-1} W. With the assumption that all points experienced this average velocity over the course of the survey, each point along the survey was backtracked to its position at the start of the survey. Using these new position coordinates for each measurement, the center was

determined by least-squares fitting to the location that minimized radial velocity (Fig. 3.1). The binned measurements were reflected about zero to create a composite transect through the eddy; Fig. 3.4 shows depth-averaged quantities for this composite transect.

Heat content anomaly per azimuthal meter relative to 0 °C (Fig. 3.4a) was calculated in 500 m radial bins, and was concentrated in the homogeneous warm core of the eddy. At the edges of the eddy, the heat anomaly tapered off. The total heat content anomaly of the eddy relative to 0 °C of 7×10^{16} J was calculated by assuming azimuthal symmetry so that the heat calculated in each radial bin was integrated over a ring of equal distance from the eddy center.

Composite azimuthal velocity (V_θ) in each bin (Fig. 3.4b, black) was calculated by applying coordinate transforms to each measured Cartesian velocity prior to binning these values. Geostrophic velocity ($V_{\theta g}$, Fig. 3.4b, blue) was determined by integrating the thermal wind equation

$$\frac{\partial V_{\theta g}}{\partial z} = -\frac{g}{\rho_0 f}\frac{\partial \rho}{\partial r}, \tag{3.1}$$

in which g is acceleration due to gravity (9.8 m s^{-2}), r is the distance from a given bin to the eddy's center, f is 1.37×10^{-4} s^{-1}, and ρ is the binned potential density. We assumed completely geostrophic velocities at 140 m (the deepest we consistently sampled density). $V_{\theta g}$ explained about 90% of the eddy's velocity, with cyclostrophic velocity ($V_{\theta c} = \sqrt{gr\rho_r/\rho}$, Fig. 3.4b, red) accounting for the remaining 10%.

The average relative vorticity ($\zeta = r^{-1}\partial(rV_\theta)/\partial r$) across the full extent of the eddy (Fig. 3.4c) was -3×10^{-5} s^{-1}. Taking the eddy Rossby number to be Ro = $|\zeta|/f$ gives an eddy Rossby number of 0.2. Based on the Zhao et al. (2014) study of Arctic eddies identified from ice-tethered profiler (ITP) data, this is well within the range of eddies typically observed in the Arctic. Within the eddy's central core, the relative vorticity almost perfectly offsets planetary vorticity. This is similar to the eddy described by D'Asaro (1988b), in which the potential vorticity at the eddy core was nearly zero due to the opposing influences of relative and planetary vorticity.

3.3.2 Turbulence and heat fluxes

Observations collected along transects T5 and T6 included microstructure shear and temperature measurements. All quantities were binned to 0.25 m bins with χ treated as discussed in Appendix A. The lateral temperature gradient was smoothed over 1 km in the horizontal. The TKE dissipation rate (Fig. 3.5a) was high [$\mathcal{O}(10^{-6})$ W kg^{-1}] near the surface (extending to 15-20 m depth) due to ship wake and surface boundary layer processes (e.g., MacKinnon et al. (2016)), and generally low beneath this layer. However, ε was elevated [$\mathcal{O}(10^{-8})$ W kg^{-1}] compared to background noise [$\mathcal{O}(10^{-10})$ W kg^{-1}] in a relatively thin layer surrounding the eddy's thermohaline core. Within the core, ε was generally not detectable above the instrument noise level. Similarly, χ (Fig. 3.5, top right) was high near the surface and elevated at the edges of the eddy.

Elevated ε and high temperature gradients surrounding the eddy core (Fig. 3.5, Fig. 3.3) suggest that heat may have been mixing from the eddy's core into the surrounding water. In the following section, we describe the observations that indicate the presence of three distinct processes: shear-driven mixing, DDC, and lateral heat fluxes due to thermohaline intrusions. This discussion is followed by a quantitative analysis of the heat fluxes and transport due to each process.

Observations indicating the presence of each process

Shear-driven mixing

We calculated shear at a 4 m scale ($\mathbf{U}_{z_{4m}} = \sqrt{u_z + v_z}$) by interpolating velocity to a regularly spaced 0.2 km grid, smoothing to 4 m bins in the vertical and 1 km bins in the horizontal, and taking 4 m first differences. Above and below the eddy core, $\mathbf{U}_{z_{4m}}$ was elevated (Fig. 3.6a). The general pattern of $\mathbf{U}_{z_{4m}}$ was consistent with a core in solid-body rotation; however, there were smaller anomalies in shear that could be due to small-scale processes. Prior studies suggest that internal waves may interact with the potential vorticity of eddies, leading to effects that can

induce refraction or wave breaking at the edge of eddies via various mechanisms (Kunze, 1985, 1986), and such effects have been observed in previous studies of Arctic eddies (Halle, 2003; Kawaguchi et al., 2016). The anomalies we observed in shear are suggestive of internal waves, although frequency information cannot be determined from this survey.

The buoyancy frequency squared (N^2_{4m}, Fig. 3.6b), similarly calculated by interpolating density to the same grid as velocity, smoothing, and taking first differences over 4 m, was also high above the eddy. The inverse Richardson number ($Ri^{-1}_{4m} = \mathbf{U}_{z4m}{}^2/N^2_{4m}$) is used to characterize the propensity for shear instability, with growing instabilities expected for $Ri^{-1} > 4$. In these measurements, Ri^{-1}_{4m} is generally low, but is elevated below the eddy core, suggesting possible susceptibility to shear instabilities (Fig. 3.6c). Shear instabilities may also occur at vertical scales smaller than the 4 m smoothing used to calculate Ri^{-1}_{4m}. The rate of turbulent dissipation ε, measured on T5 using the MMP, was elevated above and beneath the eddy's core and on the flanks of the eddy (Fig. 3.6d). Beneath the eddy core, elevated ε may be explained by shear instabilities that occur due to geostrophic shear. However, the elevated ε above the eddy and on its flanks is primarily due to other smaller-scale processes.

Double diffusive convection (DDC) The vertical temperature gradient just above the eddy's core was quite strong [$\mathcal{O}(1)$ °C m^{-1}] (Figs. 3.2a, 3.3). Both temperature and salinity increased with depth above the eddy, creating favorable conditions for the formation of diffusive layers. These layers were apparent in individual profiles of both temperature and salinity (Fig. 3.7, a, b) as well-mixed homogeneous layers separated by sharp interfaces with high gradients in both temperature and salinity.

The density ratio $R_\rho = (\beta\Delta S)/(\alpha\Delta T)$, in which α is the thermal expansion coefficient, β is the saline contraction coefficient, ΔT is the vertical difference in temperature over a given depth range, and ΔS is the vertical difference in salinity across the same range, indicates susceptibility to double diffusion (Turner, 1974; Huppert and Turner, 1981). The Turner angle (Fig. 3.5c) $Tu = tan^{-1}[(\alpha\Delta T)/(\beta\Delta S)] - 45°$ maps the density ratio onto the polar plane. In this formulation,

$-90° < Tu < -45°$ corresponds to DDC instabilities, $-45° < Tu < 45°$ corresponds to stable stratification, $45° < Tu < 90°$ indicates salt fingering instabilities, and $Tu > 90°$ and $Tu < -90°$ both correspond to gravitational instabilities. The Turner angle indicates that the region above the eddy is subject to DDC, while the region within the eddy core is double diffusively stable (Fig. 3.5c), consistent with the observed staircase structure at the top of the eddy (Fig. 3.7, a). The average density ratio in this region is $R_\rho = 2.6 \pm 1.0$. Additional DDC characteristics are given in Table 3.2. Based on the presence of stair-steps, shear that is weak relative to the local stratification, and the local Turner angle, we assume the elevated values of ε observed at the top of the eddy (Fig. 3.6, Fig. 3.5) were associated primarily with DDC. There was a small region below the eddy's core that was weakly susceptible to salt fingering instabilities (75-80 m); however, since this region was quite small we conclude that shear-driven mixing was dominant beneath the eddy core. Salt fingering may have played a more significant role within the eddy core between 55 to 60 m depth; however as this process moves heat within the eddy's core rather than removing it from the eddy we have not treated it in our analysis.

Lateral intrusions

Lateral temperature gradients (Fig. 3.5d) and salinity gradients (not shown) were fairly strong along the sides of the eddy, with temperature gradients of $\mathcal{O}(10^{-3})$ °C m^{-1}. This promotes another double diffusive phenomenon: thermohaline intrusions. These intrusions appeared as alternating layers of cold-fresh and warm-salty water which were coherent across multiple profiles at the sides of the eddy (Fig. 3.7, a, c). Double-diffusive intrusions can occur due to the presence of warm salty water lying next to cold fresh water (Stern, 1967; Ruddick and Turner, 1979), and May and Kelley (1997) describe how a density-compensated thermohaline gradient, combined with lateral shear, can also trigger a baroclinic instability, leading to lateral mixing. The analysis that follows depends on the assumption that the intrusions were approximately in steady state balance on timescales that are short relative to the eddy decay time; that is, that the timescale for the evolution of intrusions was significantly longer than the timescales associated with the

observed turbulence (but short enough that the eddy did not decay substantially during this timescale). Intrusions generally evolve over timescales of days to months (e.g., Gregg (1980); Armi et al. (1989)), supporting this assumption.

A single vertical profile through the intrusive region shows the layered cold-fresh/warm-salty structure (Fig. 3.8a; this structure is more pronounced in temperature than salinity due to higher resolution in temperature and its weaker influence on density). The Turner angle calculated along the profile shows both the top and bottom of warm-salty intrusions are susceptible to double diffusion, with DDC instability above intrusions and susceptibility to salt fingering beneath intrusions (Fig. 3.8b). We see evidence of DDC at the top of warm-salty regions, where small steps in both temperature and salinity indicate the presence of DDC (Fig. 3.8a). The rate of dissipation of both TKE and thermal variance was generally modest along intrusions, with intermittent spikes in both ε and χ apparent in diffusive convective regions (e.g., 60 m depth, Fig. 3.8c and d).

As intrusions develop along the flanks of an eddy, they act like the ribs on a radiator, increasing the surface area over which heat can exit the eddy. Along each warm-salty intrusion, strong thermal gradients above and below the intrusion drive double diffusion and allow heat to mix vertically out of the intrusion. If the intrusions remain in approximate steady state on timescales short compared to the eddy decay time, the total flux of heat out the top and bottom of each intrusion must be balanced by the lateral advective flux of heat along the warm-salty intrusion (just as the heat that radiates out of the ribs of a radiator must be balanced by heat that enters through the radiator's pipe if the radiator's temperature remains constant). This model has been used by Gregg (1980) and Ruddick et al. (2010) to infer the net lateral heat flux through intrusions by matching it to the small-scale turbulent heat fluxes through the edges of individual intrusions. This is the approach we take here as well.

Heat fluxes due to each process

In the following analysis, each process is considered separately in the region of the eddy in which it dominates:

1. Shear-driven turbulence beneath the eddy's core (horizontal coordinate 8 km $< s <$ 16 km and 27 km $< s <$ 35 km, where s is kilometers along ship track from the start of the microstructure survey and within isopycnals $24.8 < \sigma_\theta < 25.5$; green contour in Fig. 3.5);

2. DDC, (8 km $< s <$ 16 km and 27 km $< s <$ 35 km, where x is kilometers along ship track from the start of the microstructure survey, and within isopycnals $24.8 < \sigma_\theta < 25.5$; red contour in Fig. 3.5); and

3. Lateral mixing at the edges of the eddy ($s <$ 8 km, 16 km $< s <$ 27 km, and $s >$ 35 km, within isopycnals $23.6 < \sigma_\theta < 25$, and where the lateral thermal gradient magnitude is at least 5×10^{-4} °C m^{-1}; cyan contour in Fig. 3.5).

Shear-driven turbulence beneath the eddy core

Density diffusivity due to shear-driven turbulence at the bottom of the eddy (K_ρ^{bottom}) is calculated using Osborn's 1980 equation, $K_\rho^{bottom} \leq \Gamma\langle\varepsilon\rangle/\langle N^2\rangle$, in which Γ is a mixing efficiency and N^2 is the buoyancy frequency (Osborn, 1980), and angled brackets indicate averages taken over all bins within the region. Γ is generally taken to be 0.2 (e.g., Gregg et al. (2018)). In fully-developed turbulence, heat and density both diffuse at the same eddy diffusivity, and K_ρ^{bottom} is identical to the thermal diffusivity K_T^{bottom}. We assume this equivalence holds throughout the analysis.

Beneath the eddy's core, $\langle\varepsilon\rangle$ was 1.1×10^{-9} W kg^{-1} and $\langle N^2\rangle$ was 5.6×10^{-4} s^{-1} (Fig. 3.9iii). This results in an upper bound for K_T^{bottom} of 4×10^{-7} m^2 s^{-1} (about 2.5 times the molecular value for heat). The average T_z found beneath the eddy's core was -0.3 °C m^{-1}. The

average heat flux $F_H^{bottom} = -\rho C_p K_T^{bottom} T_z$ out of the bottom of the eddy was estimated as -0.5 W m^{-2} (Fig. 3.10c). The eddy's lifetime may be estimated by considering the integrated area flux of 4 $\times 10^7$ W removing the eddy's heat anomaly of 7 $\times 10^{16}$ J. This results in a decay timescale of 60 years.

Double diffusive convection above the eddy core

Multiple methods have been used to estimate heat fluxes due to DDC. The Osborn-Cox equation, $K_T^{OC} = 0.5\langle\chi\rangle/\langle\theta_z\rangle^2$ (Osborn and Cox, 1972), in which angled brackets represent averaged values of χ and N^2 on isothermal surfaces, applies in the double diffusive regime (see Winters and D'Asaro (1996)). Care must be taken when calculating χ, which it is generally determined via Fourier analysis over windows of approximately 1 m. Diffusive interfaces are much smaller than these windows, so a spectral window which includes an interface will give an erroneously high value for χ, due to contamination from the sharp change in background temperature gradient. It has been empirically demonstrated that the Osborn equation (Osborn, 1980) also gives fairly reliable estimates for the effective diffusivity within diffusive layers provided that Γ is taken to be 1, rather than the conventional 0.2 (in a perfectly convecting cell, each convection cycle converts all kinetic energy to potential energy, and vice versa) (St. Laurent and Schmitt, 1999; Inoue et al., 2007). Additionally, a variety of flux laws have been developed based on laboratory studies that relate heat flux to the temperature difference $\delta\theta$ across adjacent steps (e.g., Turner (1973); Kelley (1984, 1990) and others). These laws have the advantage that fluxes may be computed without microstructure measurements of temperature or shear. Such flux laws have been applied to oceanic DDC and appear to agree well with microstructure results (Padman and Dillon, 1989; Sundfjord et al., 2007; Polyakov et al., 2012; Guthrie et al., 2015).

For the purpose of this analysis, four distinct methods were used to calculate the heat flux due to diffusive convection. First, for ease of comparison with the other processes, the Osborn-Cox equation was used with 0.25 m binned data with averages taken over the entire diffusive convective region (Fig. 3.9, top), so that flux derived from χ (F_χ) was estimated as

$F_\chi = \rho C_p K_T^{OC} T_z$. In the region at the top of the eddy's core, $\langle \chi \rangle$ was 1.6×10^{-6} °C^2 s^{-1} and $\langle T_z \rangle$ was 1.0 °C m^{-1}. This method led to an effective diffusivity K_T^{OC} of 8×10^{-7} m^2 s^{-1} and an estimated heat flux of 3 W m^{-2}.

For a more robust analysis, we followed the methods of Padman and Dillon (1989), who calculated diffusive convective fluxes within each layer of a diffusive staircase (see Fig. 3.11). In this analysis, windows containing only the well-mixed diffusive layers were hand-selected for each profile. While these fluxes should ideally be calculated based on values averaged horizontally along a single diffusive layer, we found it difficult to trace single layers over multiple adjacent profiles, likely due to the short height of layers and the high-shear background environment that may result in intermittent disruptions to layers. For this reason, fluxes were calculated from values determined within each layer for each profile. The reported results are an average of such fluxes. Both the Osborn-Cox and the Osborn equation with $\Gamma = 1$ were used to calculate fluxes within each layer. The calculated fluxes over the diffusive convective region were 6 W m^{-2}, using $F_{\chi_{layers}} = \rho C_p K_{T_{layers}}^{OC} T_z$ and 4 W m^{-2}, using $F_{\varepsilon_{layers}} = \rho C_p K_{T_{layers}}^{O} T_z$, in which $K_{T_{layers}}^{O}$ was calculated with Γ = 1.

Because empirical flux laws are frequently used when microstructure measurements are not available, we also compared these results to those found using the flux law described by Kelley (1990) and verified by Guthrie et al. (2015):

$$F_{4/3} = 0.0032 \exp\left(\frac{4.8}{R_\rho^{0.72}}\right) \rho C_p \left(\frac{\alpha g \kappa}{P_r}\right)^{1/3} \delta\theta^{4/3}, \tag{3.2}$$

In Eq. (2), R_ρ is the density ratio as defined above and averaged over a profile, ρ = 1025 kg m^{-3} is density, C_p = 4000 J K^{-1} kg^{-1} is the heat capacity of salt water, κ = 1.4×10^{-7} m^2 s^{-1} is the molecular diffusivity of heat, $P_r = \frac{\nu}{\kappa}$ is the dimensionless Prandtl number (with the kinematic viscosity $\nu = 1.8 \times 10^{-6}$ m^2 s^{-1}), and $\delta\theta$ is the difference in potential temperature between adjacent layers. In general, $F_{4/3}$ is higher than that derived from both $F_{\chi_{layers}}$ and $F_{\varepsilon_{layers}}$, with an

average value of 12 W m^{-2}.

Although agreement between all methods is fair, the two estimates of flux derived from χ and ε within layers ($F_{\chi_{layers}}$ and $F_{\varepsilon_{layers}}$) incorporate all available information (both the microstructure data and the boundaries of layers), and we suspect these are the most accurate methods. Averaging these estimates together, the total heat flux over the top of the eddy core is an estimated F_H^{top} = 5 W m^{-2}. With a vertical temperature gradient of 1.0 °C m^{-1}, this corresponds to an approximate thermal diffusivity K_T^{top} of 1.2 $\times 10^{-6}$ m^2 s^{-1}. Taking the area-integrated heat flux as 4 $\times 10^8$ W and the eddy's heat anomaly of 7 $\times 10^{16}$ J suggests a decay timescale of 6 years.

Lateral intrusions on the sides of the eddy

Assuming that the intrusions are in approximate steady state, all vertical production of temperature variance must be balanced by large scale horizontal production of variance. The effective isopycnal thermal diffusivity due to advection along intrusions ($K_{T_I}^{sides}$) can be calculated from diapycnal diffusivity ($K_{T_D}^{sides}$) as $K_{T_I}^{sides} = \overline{K_{T_D}^{sides} T_z^2} / \overline{T_x}^2$ (Ruddick et al., 2010), in which $\overline{T_x}$ represents the bulk lateral gradient and $\overline{K_{T_D}^{sides} T_z^2}$ is averaged over the entire intrusive region. Ruddick et al. (2010) obtained this result by equating the horizontal production of thermal gradient variance to the vertical production averaged over all the intrusive surfaces, which is in turn equated to the average χ.

The simplest way to calculate $K_{T_D}^{sides}$ within the intrusive region is by taking the Osborn-Cox equation $K_{T_D}^{sides} = 0.5\langle\chi\rangle / \langle\theta_z\rangle^2$ and using this to calculate $K_{T_I}^{sides}$ from the averaged χ and T_x within the intrusive region. We found $\langle\chi\rangle$ in this region was 1.09$\times 10^{-6}$ °C^2 s^{-1} and $\langle T_x\rangle$ was 1.2$\times 10^{-3}$ °C m^{-1} (Fig. 3.9). This results in an estimated $K_{T_I}^{sides}$ of 0.4 m^2 s^{-1}. The lateral heat flux F_H^{sides} is 2000 W m^{-2} (Fig. 3.10), and the corresponding lifetime taking area-integrated heat flux of 2 $\times 10^9$ W and assuming this removes the eddy's heat anomaly of 7 $\times 10^{16}$ J suggests a decay timescale of 1 year.

Within the intrusive region, accurately calculating χ is somewhat challenging as intrusions can occur on very small scales and are difficult to distinguish from turbulent features (see

Appendix A). Therefore, we additionally use measured ε to bound the lateral flux as follows.

There are two distinct processes that can result in elevated ε: (1) shear-driven turbulent mixing can occur along intrusions, either as the large scale azimuthal velocity of the eddy is converted to intrusion-scale shear or due to other sources of shear, and (2) DDC can occur above warm/salty intrusions. While characteristic diffusive layers are apparent above intrusions in some profiles, these are not coherent across multiple profiles, suggesting that there is sufficient shear to disrupt DDC cells, and that both DDC and shear-driven turbulence could contribute to the observed ε. We treat the two extreme cases of pure shear-driven turbulence and pure DDC using Osborn's equation $K_{T_D}^{sides} = \Gamma\langle\varepsilon\rangle/\langle N^2\rangle$. For shear-driven turbulence, the mixing efficiency Γ is set to 0.2, while for DDC Γ can be taken to be 1 (St. Laurent and Schmitt, 1999; Inoue et al., 2007). Thus, assuming that the observed ε is entirely due to shear-driven turbulence (DDC) results in a lower (upper) bound on the effective lateral diffusivity and resulting heat flux.

To bound heat flux, we set $K_{T_D}^{sides} = \Gamma\langle\varepsilon\rangle/\langle N^2\rangle$ and proceed to calculate $K_{T_I}^{sides} = K_{T_D}^{sides}\langle T_z^2\rangle/\langle T_x\rangle^2$. With $\langle\varepsilon\rangle$ = 2.0$\times10^{-9}$ W kg^{-1}, $\langle N^2\rangle$ = 7.1$\times10^{-4}$ s^{-2}, $\langle|T_x|\rangle$ = 1.2$\times10^{-3}$ °C m^{-1}, and $\langle T_z^2\rangle$ = 0.44 °C^2 m^{-2}, the resulting bounds on $K_{T_I}^{sides}$ are 0.2-0.8 m^2 s^{-1} (for Γ in the range 0.2-1; Fig. 3.9). The corresponding range of heat flux is 800-4000 W m^{-2}.

Both upper and lower bounds are within a factor of 3 of the original estimate of F_H^{sides} = 2000 W m^{-2} from χ, and are thus within the instrument error associated with measurements of χ and ε. Although we lack the horizontal resolution to fully verify the Ruddick et al. (2010) method for calculating $K_{T_I}^{sides}$, we can use the assertion that the total vertical transport of heat out of the eddy along intrusions must be balanced by an advective flux along intrusions to assess whether the model is physically realistic. Considering the average vertical heat flux in the intrusive region, $\rho CpK_{T_D}^{sides}|T_z| = 3$ W m^{-2} and the horizontal heat flux $\rho CpK_{T_I}^{sides}|T_x| = 2000$ W m^{-2}, we see that these differ by a factor of 700. The net heat transport through the vertical surfaces above and below isopycnals must match the horizontal heat transport. Assuming that both lateral and vertical heat fluxes occur over the same radial distance, this factor of 700 must represent the

ratio of the vertical height of the eddy core (corresponding to the distance over which lateral heat flux occurs) to the path length along intrusions (corresponding to the distance over which the vertical heat flux occurs). Taking the height of the intrusive region to be 30 m, this implies an along-intrusion path length of 20 km. The intrusive region extends about 2-3 km. Individual intrusions extend up to 2 km, so that a total path length of 20 km due to four or five intrusions is plausible.

3.4 Total heat loss implications

Putting together the results of the last section, a picture emerges of a warm eddy losing heat from its top, bottom, and sides (Fig. 3.12). Using the results from the last section and modeling the eddy as a cylinder with a height of 40 m and a radius of 5 km, we can calculate the total heat transport out of the eddy due to each of the identified processes: (1) shear-driven turbulence acting at the bottom of the eddy transports 0.04 GW (0.01 to 0.1 GW); (2) DDC acting at the top of the eddy transports 0.5 GW (0.2 to 1.5 GW); and (3) lateral intrusions acting along the sides of the eddy transport 2 GW (1 to 6 GW). Our measurements show a net heat flux out of the eddy at this time of 2.5 GW; if this were simplistically extrapolated into the future it suggests a decay timescale of about a year. Complete results are given in Table 3.3.

3.5 Summary and discussion

The structure and dynamics of a warm-core intrahalocline anticyclonic eddy observed on the Chukchi shelf in September of 2015 have been described. With core temperatures around 6 °C, this eddy was extremely warm compared to most prior observations of Arctic eddies, although the eddy described by Kawaguchi et al. (2012) was similarly warm. A 6 °C intrusion was also observed in the Canada Basin at approximately 50 m depth by an Ice-Tethered-Profiler

in 2010 (Timmermans and Jayne, 2016). The recent appearance of these warm subsurface features suggests that either modern sampling schemes are capturing intermittent features that were previously unobserved, or that temperature anomalies of 6 °C in the western Arctic are a relatively new phenomenon. Such structures may play an important role in the transport of Pacific-origin heat and freshwater in the Canada Basin, and may have biological effects as well.

Microstructure measurements through the eddy core determined that while ε was generally weak beneath the mixed layer, ε was elevated surrounding the eddy core [$\mathcal{O}(10^{-8})$ W kg^{-1}] as a result of three different processes: shear-driven overturns below the eddy core, diffusive convection above the core, and lateral mixing due to intrusions along the sides of the eddy. The eddy lost heat at a rate of 2.5 GW, with lateral mixing responsible for approximately 80% of this heat loss and DDC accounting for the remaining 20%. Heat loss by shear turbulence at the bottom of the eddy was negligible.

These estimates are subject to many sources of error. Inferring ε and χ from microstructure shear and temperature measurements is subject to errors of up to a factor of 3. Our windowing procedure for calculating χ (Appendix A) is subjective and subject to error, particularly in intrusive regions as distinguishing between turbulent mixing and small scale thermohaline intrusions is extremely difficult. The validity of the Ruddick et al. (2010) formulation for the decay of an eddy to thermohaline intrusions has not been established outside of the meddy Sharon; in the Arctic Ocean the thermal expansion coefficient α is quite small and varies strongly with temperature, which may affect the results. Additionally, we assume the turbulence is isotropic even though this is a low shear environment in which this assumption may not hold at all times. We use canonical values for Γ of 0.2 in shear-driven turbulence and 1 in DDC turbulence although the accuracy of these values is an area of active research. We have also extrapolated heat fluxes for the entire eddy based on a pair of transects, neither of which bisected the eddy's center. However, the lifetime we estimate for the eddy of approximately a year is in line both with other observations of small Arctic eddies (e. g., D'Asaro (1988a), Zhao et al. (2014)) and with the observed decay of the

meddy Sharon, which also decayed due to thermohaline intrusions (Armi et al., 1989; Ruddick et al., 2010).

The 5 W m^{-2} DDC flux present above the eddy is notable in contrast to the relatively weak effect of the ubiquitous diffusive layers at the top of the Atlantic Water, which are thought to be associated with maximal heat fluxes of 0.3 W m^{-2} in the Canada Basin (Timmermans et al., 2008a). The larger DDC fluxes observed above the eddy are more similar in magnitude to those observed in the Eurasian basin (Padman and Dillon, 1991; Polyakov et al., 2012), and occur due to the significant temperature gradient [$\mathcal{O}(1)$ °C m^{-1}] and unstable density ratio above the eddy. The relatively high-shear environment may also play a role in increasing fluxes through the diffusive staircase as the ambient shear injects energy and creates instabilities between the convecting cells and interfaces that separate them (Padman, 1994; Stamp et al., 1998; Smyth and Kimura, 2007). The fluxes calculated in the above analysis are lower than the average fluxes of 20 W m^{-2} that Kawaguchi et al. (2012) observed above a similar warm-core eddy. This may be partially explained because Kawaguchi et al. (2012) observed extremely elevated values of χ in a few regions, which they attributed to intense double-diffusive mixing. However, their very high χ values may also be overestimates that result from taking spectral windows over the discrete steps within a DDC staircase; such steps contaminate the Fourier transform at all scales and are inconsistent with the turbulence theory underlying this analysis technique (see Appendix A for details).

Existing literature suggests eddies are generated both in Barrow Canyon and along the Beaufort and Chukchi shelf breaks (D'Asaro, 1988a; Pickart et al., 2005; Spall et al., 2008). While most studies have focused on cold-core eddies, eddies such as the one described in this study could play an important role in transporting warm coastal water into the interior of the Arctic basin. We estimate the observed eddy has a lifetime of $\sim$1 year; assuming it continued to travel at a rate of 8 cm/s into the basin, this would allow it to penetrate $\sim$1500 km into the basin, carrying heat, salt, and nutrients with it. However, this assumes that the eddy dynamics

remain constant in time, which may not be the case. During the fall and winter as the mixed layer deepens, shear-driven mixing may play an increasingly important role in extracting heat from the eddy. Profiles collected in the Beaufort Sea of October of 2015 in similar regions suggest the mixed layer can deepen to 25 or 30 m as early as October (Toole et al. (2010); Timmermans (2015), Jim Thomson, personal communication 2017). If the eddy were to persist at the same depth into the autumn and encountered such conditions, its dynamics would rapidly change, likely resulting in its dissolution and the release of its heat to the mixed layer. Assuming the eddy survived 40 days after observation and continued to drift at 8 cm/s, it would penetrate about 300 km into the Canada Basin during this timeframe.

Brugler et al. (2014) suggest that summer heat transport in the Alaskan Coastal Current (ACC) at the base of Barrow Canyon averages around 3 TW, while Corlett and Pickart (2017) estimate 1.4 TW of heat are advected west along the Chukchi slope in a baroclinically unstable current (known as the Chukchi slope current) from July to October. These pathways account for approximately 3×10^{19} J of heat each year. The ultimate fate of this heat is unclear. Some of it is likely lost to the atmosphere, some may be used to melt local sea ice, and some makes its way into the Canada Basin, where it persists as a year-round subsurface temperature maximum. If all of the heat were dispersed into the basin in eddies like the one described in this study, this would correspond to the formation of $\sim$400 eddies each year. However, most PSW is not contained in such eddies, but is distributed throughout the Beaufort Sea in interleaving filaments and intrusions (e.g., Timmermans et al. (2014); Kawaguchi et al. (2014); Timmermans and Jayne (2016)). Such structures may also be susceptible to processes that mix heat both vertically and laterally, but the net heat fluxes and the relative importance of each process may be quite different.

Thermohaline intrusions may act directly on currents carrying ACW. If thermohaline intrusions similar to those along the eddy flanks exist along both the Beaufort shelfbreak jet and the Chukchi slope current, the total distance susceptible to intrusions would be 1300 km. Assuming a current depth of 50 m for both currents gives a total surface area of 6.5×10^7 m^2

facing into the basin for these currents. A lateral flux of 2000 W m^{-2} along this area would result in a total lateral heat transport of 0.2 TW. This is another pathway that could allow heat to enter the Canada Basin from these topographically trapped currents.

Within a rapidly changing Arctic, oceanic heat may play a crucial role in the growth/melt cycle of sea ice and in setting local stratification. Improving our understanding of the pathways heat takes into the basin interior and the processes that drive both vertical and lateral oceanic heat fluxes are necessary steps towards developing better models of the Arctic climate. Warm-core eddies may represent an important pathway for Pacific-origin heat into the central basin. However, the frequency of formation of such eddies and their response to seasonal deepening of the mixed layer is unknown at this time, and many questions remain to be answered.

3.6 Acknowledgements

This work was supported by NSF grants PLR 14-56705 and PLR-1303791 and by NSF Graduate Research Fellowship grant DGE-1650112. We gratefully acknowledge the r/v *Sikuliaq* captain and crew, MOD engineering team, and ArcticMix collaborators who made this study possible. We are additionally grateful to Mike Gregg, Tom Weingartner, Peter Winsor, Harper Simmons, Mary-Louise Timmermans, Yueng-Djern Lenn, Rob Pinkel, Laurie Padman, and Joe Metzger for scientific support and insight; to Mike Gregg and Dave Winkel for supporting the transition of the MMP and SWIMS instrumentation from APL/UW to SIO; and to Glenn Carter, who provided an implementation of MLE estimation for calculating χ. Finally, we thank Ilker Fer, Laurie Padman and Barry Rudnick for their helpful comments and suggestions on this manuscript.

Shipboard and microstructure data are available for download at http://www.rvdata.us/catalog/SKQ201511S and https://microstructure.ucsd.edu, respectively. SWIMS transects are available from the authors upon request.

Chapter 3, in full, is a reprint of the material as it appears in Journal of Physical Oceanog-

raphy 2018. Fine, Elizabeth; MacKinnon, Jennifer A.; Alford, Matthew H.; Mickett, John B. Microstructure observations of turbulent heat fluxes in a warm-core Canada Basin eddy. J. Phys. Oceanogr., 48:2397-2418. The dissertation author was the primary investigator and author of this paper.

3.7 Appendix: χ in double diffusive environments

χ is usually understood in the context of Osborn-Cox-style analysis, in which the small-scale variance of the thermal gradient is used to estimate thermal diffusivity. In using maximum likelihood estimation to fit Batchelor spectra to the spectra of microstructure measurements of the thermal gradients, 1 to 2 m windows are generally used. When this spectral analysis is used to infer thermal diffusivity, there is an implicit assumption that the background thermal gradient varies slowly over such length scales, so that the spectra of thermal variance relate directly to the microscale mixing associated with fully-developed isotropic turbulence.

In the Arctic Ocean, the temperature gradient at length scales of 1 to 2 m can vary rapidly in the presence of diffusive layers or thermohaline intrusions, as shown in Fig. 3.13 (see also e.g. Guthrie et al. (2015)). If spectra are calculated over windows that span such larger-scale variation, the high wavenumber portion of the temperature gradient will consist of both small temperature anomalies that relate to thermal diffusivity in a traditional Osborn-Cox sense, and of the high-wavenumber signatures of larger scale intrusions or diffusive steps. When double diffusive interfaces or intrusions occur on length scales similar to those seen in isotropic turbulence, this leads to overestimation of the thermal diffusivity and heat flux calculated from χ, since the measured high-wavenumber thermal variance is only partially due to microscale mixing. Spectra taken over such windows deviate from a Batchelor curve as a spike in the thermal gradient contaminates all wavenumbers longer than the width of the spike in spectral space.

In general, when spectra deviate too far from a Batchelor spectra the MLE analysis will

Table 3.1: Description of each transect of the eddy survey undertaken using the Shallow Water Integrated Mapping System (SWIMS) and the Modular Microstructure Profiler (MMP). SWIMS is a towed profiler that carries both CTDs and ADCPs, while MMP has fast-response shear and temperature sensors to collect microstructure data. Transects are shown in Fig. 3.1.

Transect Name	Instrument	Transect Length (km)	Number of Profiles	Ship Speed (ms^{-1})
T1	SWIMS	7.2	34	2.1
T2	SWIMS	13.8	48	2.5
T3	SWIMS	16.3	97	1.7
T4	SWIMS	19.5	81	2.3
T5	MMP	15.1	40	0.5
T6	MMP	23.1	59	0.5

not converge in a given window. In windows where this occurred, microstructure temperature was examined by eye. When possible, the window was broken down into regions in which the background thermal gradient varied slowly, and the bin estimate for χ was computed as a weighted average of these sub-binned values. Fig. 3.13 shows one such window, the spectra calculated over this window, and the subwindows that were used for the final gridded χ product as well as the spectra for a representative subwindow. While the MLE analysis would not converge over the original window, simply summing the variance beneath a cutoff wavenumber gives an estimated χ of 4×10^{-4} °C^2 s^{-1}. Taking a weighted average over the MLE estimates within each subwindow produces 5×10^{-7} °C^2 s^{-1} for the gridded χ value for this window. In this case there is a factor of 1000 difference between simple integration of the spectrum of thermal variance and careful MLE fitting within hand-selected subwindows.

This method is subject to some uncertainties. The MLE estimate may converge in windows that include some variation of background chi that is not due to turbulent mixing, biasing estimates high. We lack a rigorous method to distinguish between small-scale thermal variations due to mixing versus those due to small-scale interleaving. For this reason, all estimates of physical quantities based on measured χ are compared to estimates based on measured ε; generally these two methods show good agreement.

Table 3.2: Properties of DDC staircases. Means are taken over each step included in analysis. The 95% confidence intervals assuming statistically independent measurements are given in parentheses.

Property	Mean Value (95% confidence interval)
R_ρ	2.6 (1.6, 3.6)
Layer Height	0.96 m (0.88 m, 1.03 m)
Interface Height	0.079 m (0.075 m, 0.083 m)
ΔT Across Interfaces	0.29 °C (0.27 °C, 0.31 °C)

Table 3.3: Heat fluxes, areas, transports, diffusivity, and estimated lifetimes for each edge of the eddy core. Error bounds are given for heat flux based on the spread of alternate methods for calculating heat flux (Section 3.b.2; only one method was used to calculate heat flux out of the bottom of the eddy so quantitative error bounds cannot be determined as systemic error is likely much larger than sampling error (Fig. 3.10). Errors in the range of factors of 2 to 3 are frequently associated with this type of turbulence measurement (Peters et al., 1988).)

Region	Flux (W/m^2)	Area (m^2)	Transport (GW)	K (m^2/s)	Lifetime (years)
Above eddy core	5 (3, 12)	8×10^7	0.4	3×10^{-6}	6 years
Eddy flanks	2000 (800, 4000)	1×10^6	2	0.4	1 year
Beneath eddy core	-0.5	8×10^7	-0.04	4×10^{-7}	60 years

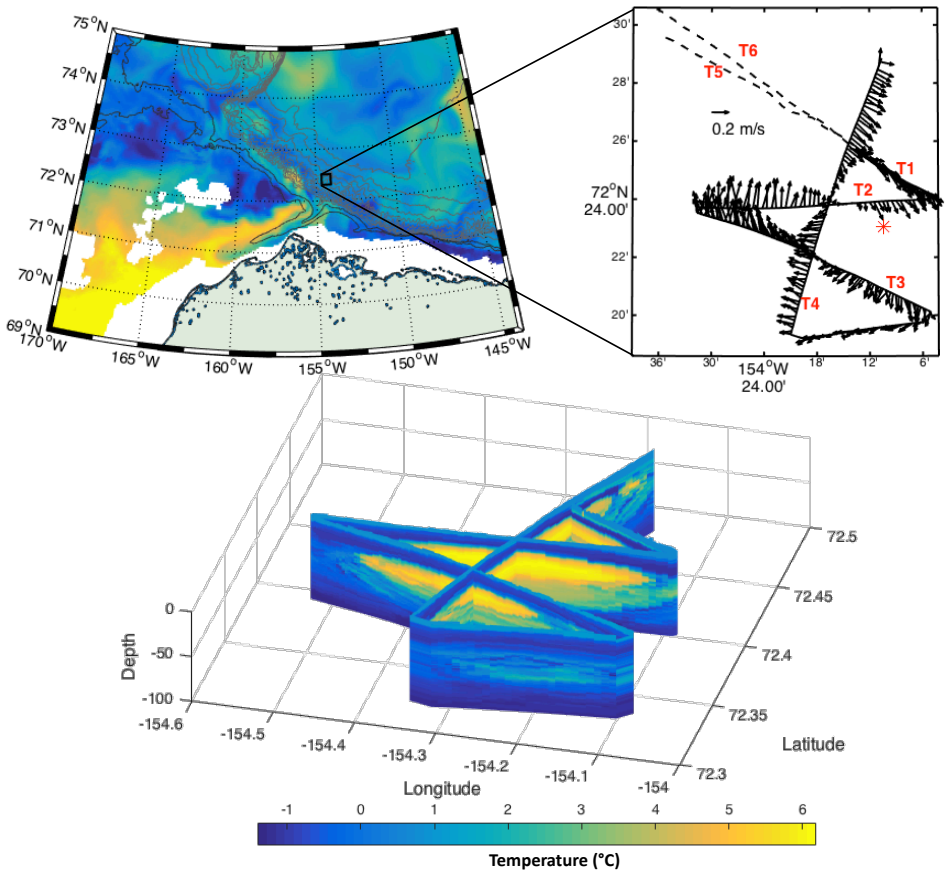

Figure 3.1: Survey details. Left: Map of the Chukchi shelf slope. Color represents temperature at 50 m depth, as determined by a global HYCOM model (Metzger et al., 2014). Barrow Canyon is just to the north west of Alaska. The eddy survey region is enclosed in a black box. Right: Eddy survey pattern. SWIMS sections are shown as solid lines, MMP as dashed. The average velocity relative to the eddy center in the 30-50 m depth range is shown for SWIMS sections. The red star indicates the inferred position of the eddy's center when the survey began. Bottom: Temperature measured in SWIMS survey along lines T1-T4.

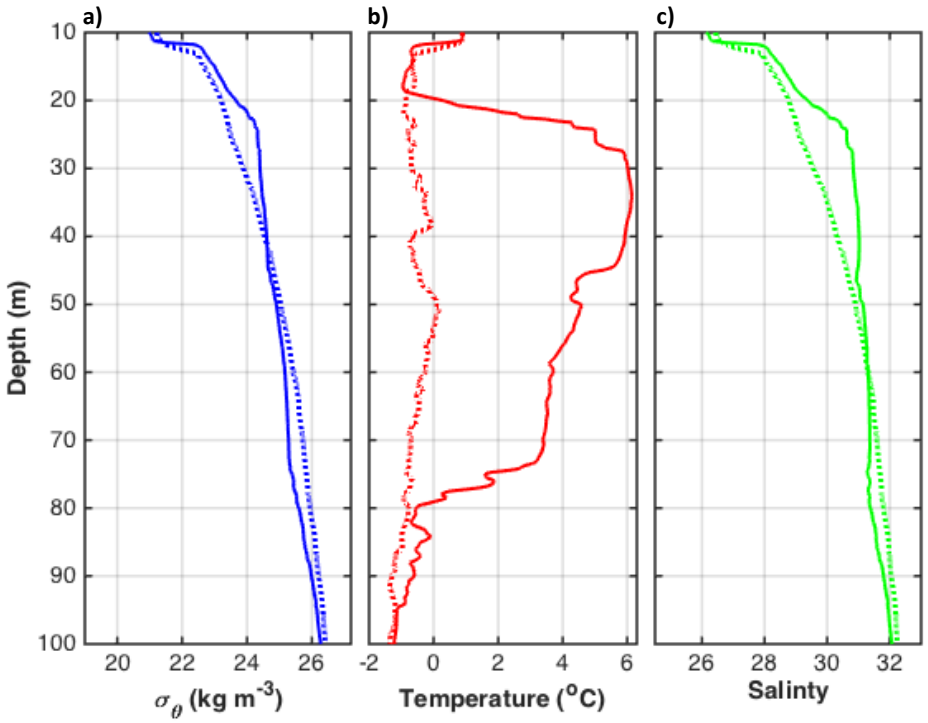

Figure 3.2: (a) Potential density, (b) temperature, and (c) salinity within the eddy core (solid) and at a point outside of the eddy (dashed).

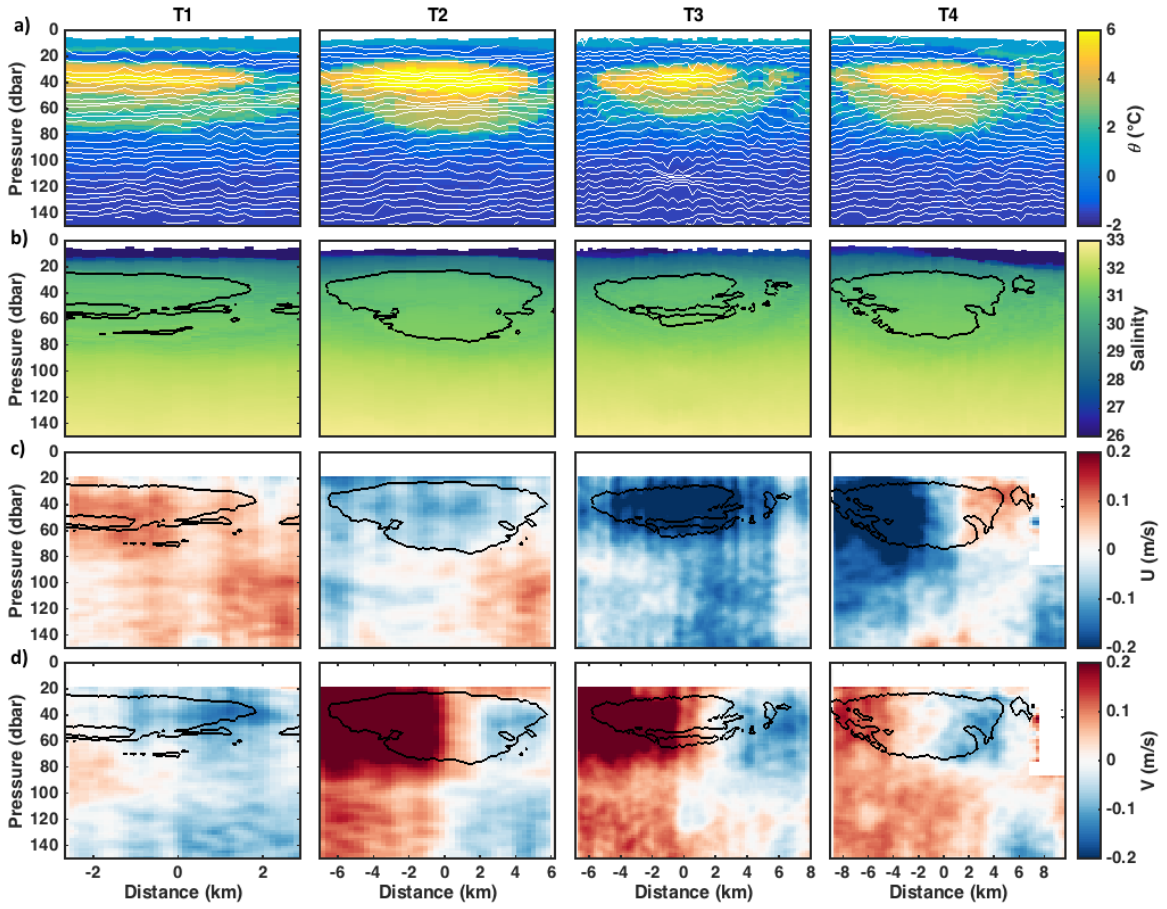

Figure 3.3: SWIMS sections of (a) temperature, (b) salinity, (c) eastward, and (d) northward velocity plotted against along-track distance. In (a), isopycnals are contoured in white. In (b), (c), and (d), the 3 °C isotherm is contoured in black.

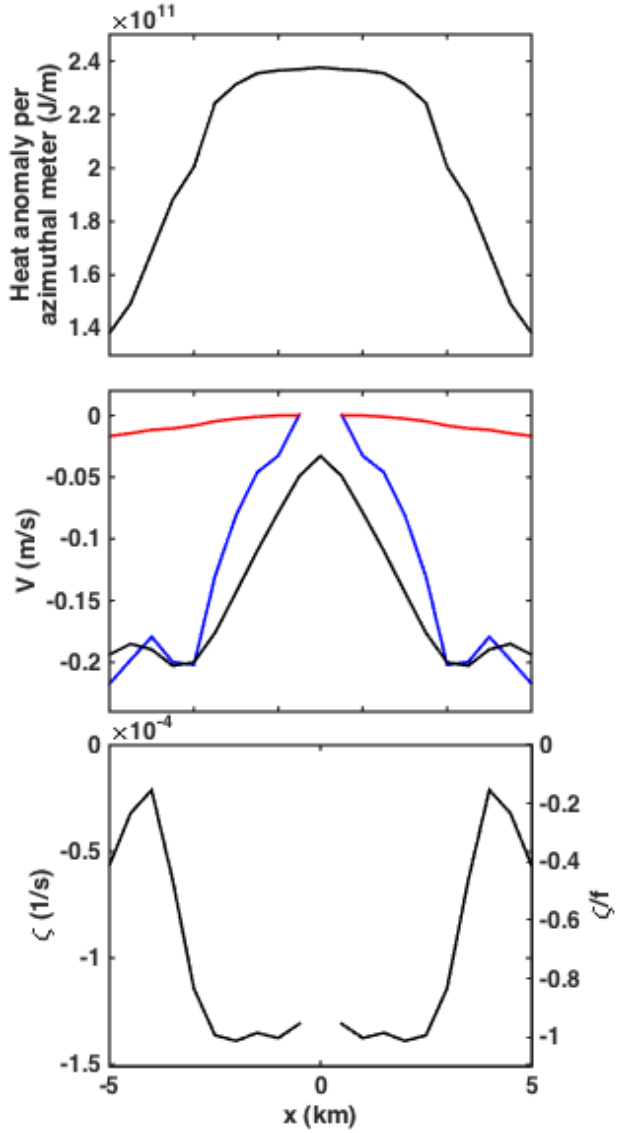

Figure 3.4: Composite eddy (a) heat content anomaly relative to 0 °C per azimuthal meter, (b) total (black), geostrophic (blue), and cyclostrophic (red) azimuthal velocity, and (c) vorticity, averaged within the core of the eddy (30 - 50 m depth). Heat per meter (a) is integrated vertically and radially, so that integrating azimuthally results in total eddy heat. All plots are symmetric about the center of the eddy.

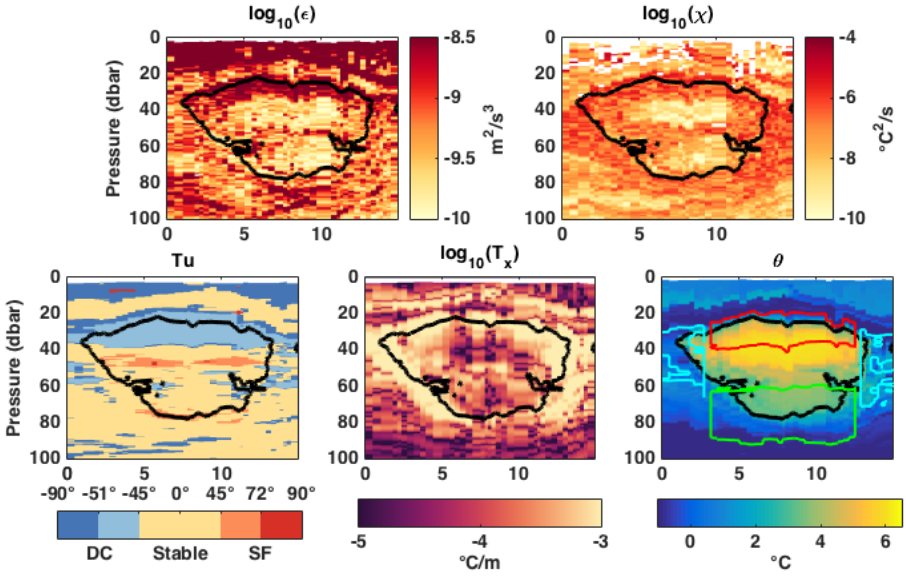

Figure 3.5: (a) ε, (b) χ, (c) vertical Turner angle (Tu), (d) horizontal temperature gradient, and (e) θ measured in T5. The x-axis represents distance from the start of the transect in km. The 3 °C isotherm is contoured in black; the zones referred to as the "top", "bottom", and "sides" of the eddy are contoured in red, cyan, and green, respectively in (e).

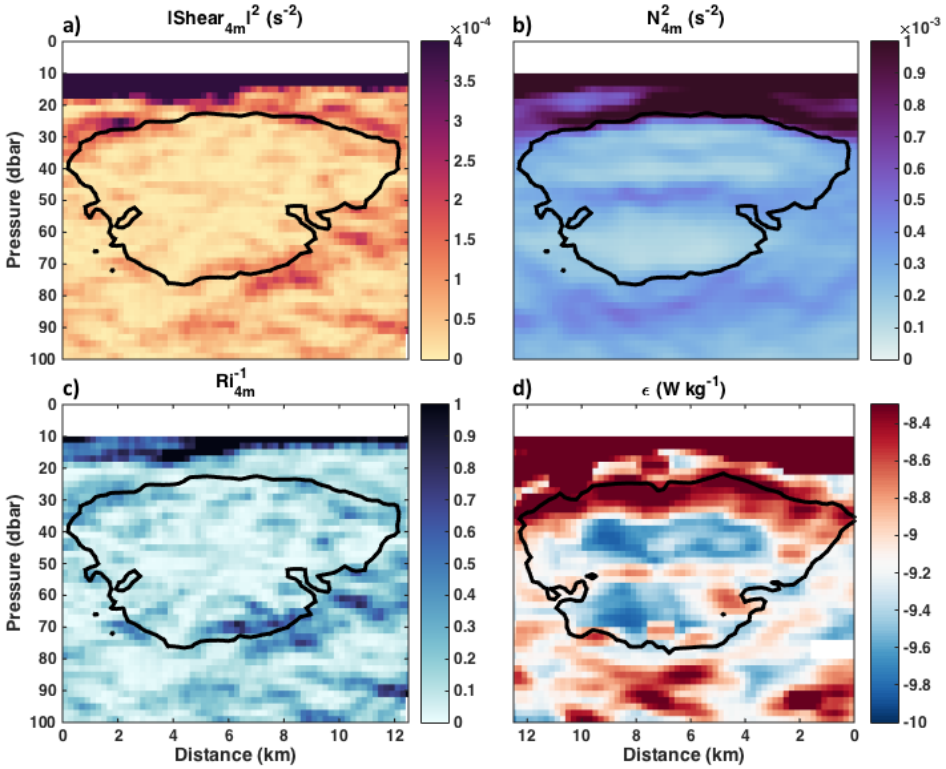

Figure 3.6: (a) Magnitude-squared of shear$_{4m}$, (b) N^2_{4m}, and (c) inverse Ri$_{4m}$ from T2; (d) ε from T5. The 3 °C isotherm is contoured in black in all panels. The x-axis represents distance along each transect; in (d) the axis is flipped because T5 was undertaken in the opposite direction from T2. Although T2 and T5 do not spatially overlap (Fig. 3.1), the shape of the 3 °C contour was similar in both transects due in part to the eddy's translational motion during the survey.

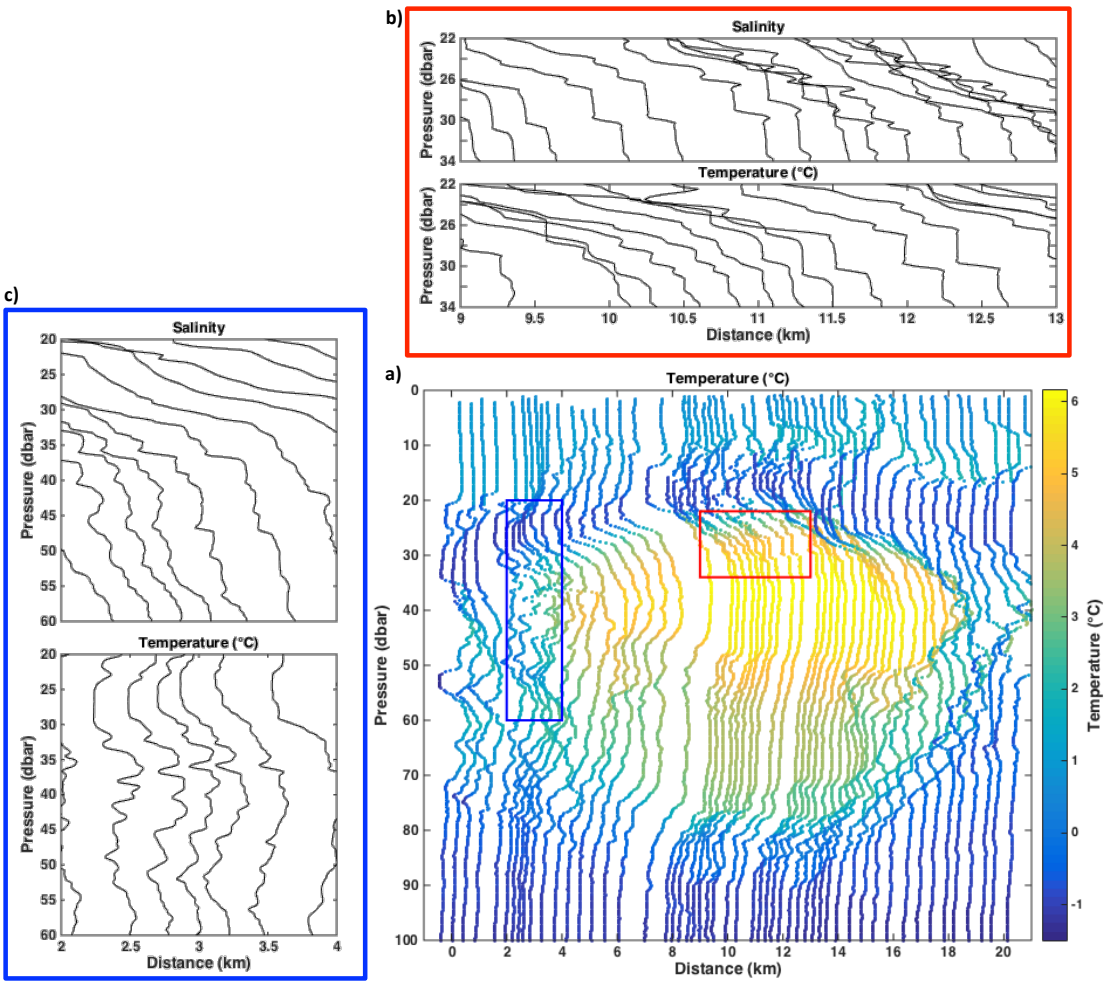

Figure 3.7: Temperature and salinity profiles. (a) All temperature profiles taken on T5 of the eddy. The red box highlights a region with diffusive layers; the blue box highlights a region with thermohaline intrusions. (b) Salinity and temperature profiles at the top of the eddy. Distinctive steps are apparent, with well-mixed layers separated by sharp interfaces. The salinity profiles show some salinity spiking due to the abruptness of the interfaces. (c) Salinity and temperature profiles at the side of the eddy. Alternating layers of cold/fresh and warm/salty water indicate the presence of lateral intrusions.

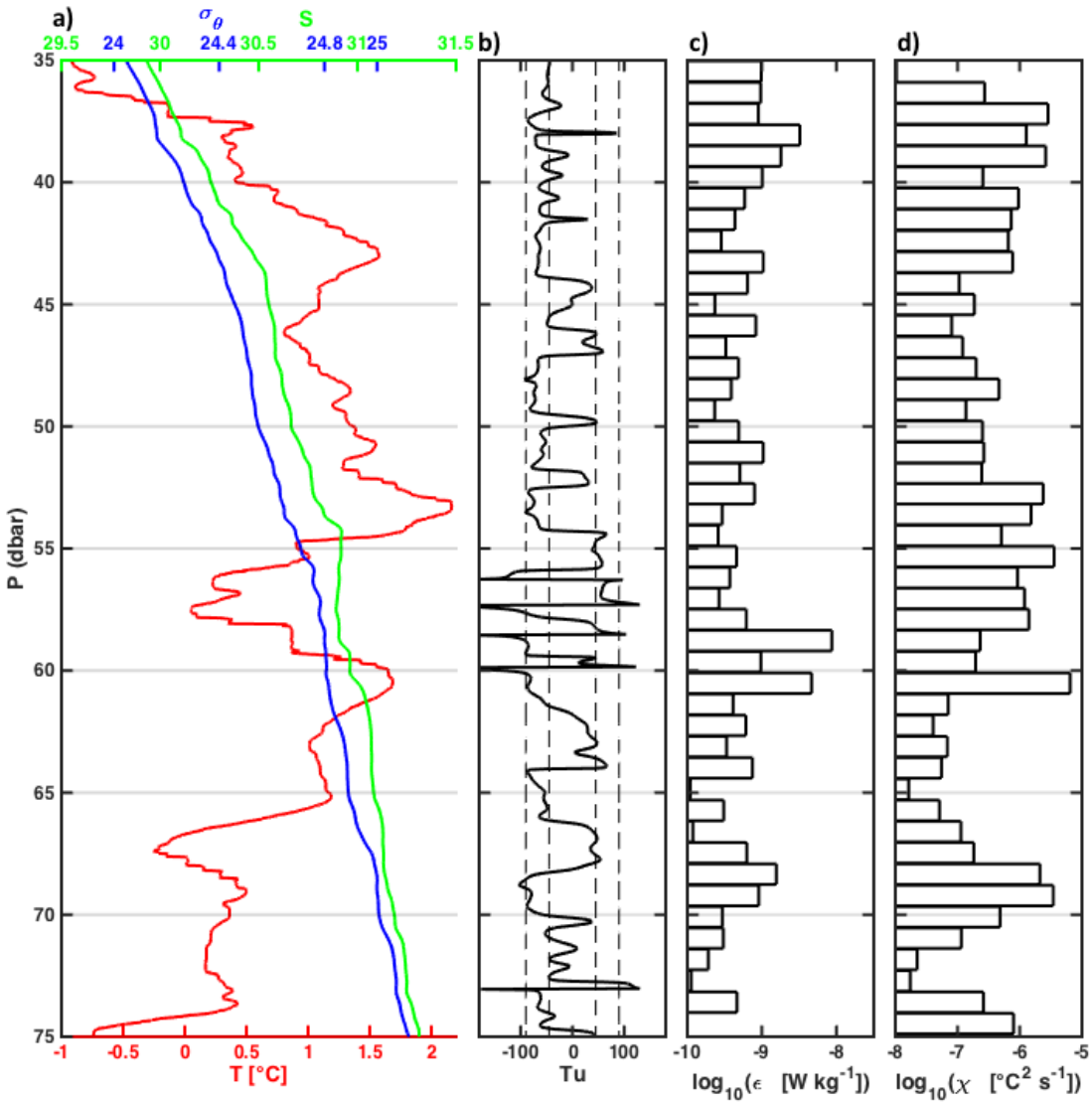

Figure 3.8: A single profile in the intrusive region showing: a) high-resolution thermistor temperature, CTD salinity and density; b) Turner angle; c) ε and d) χ.

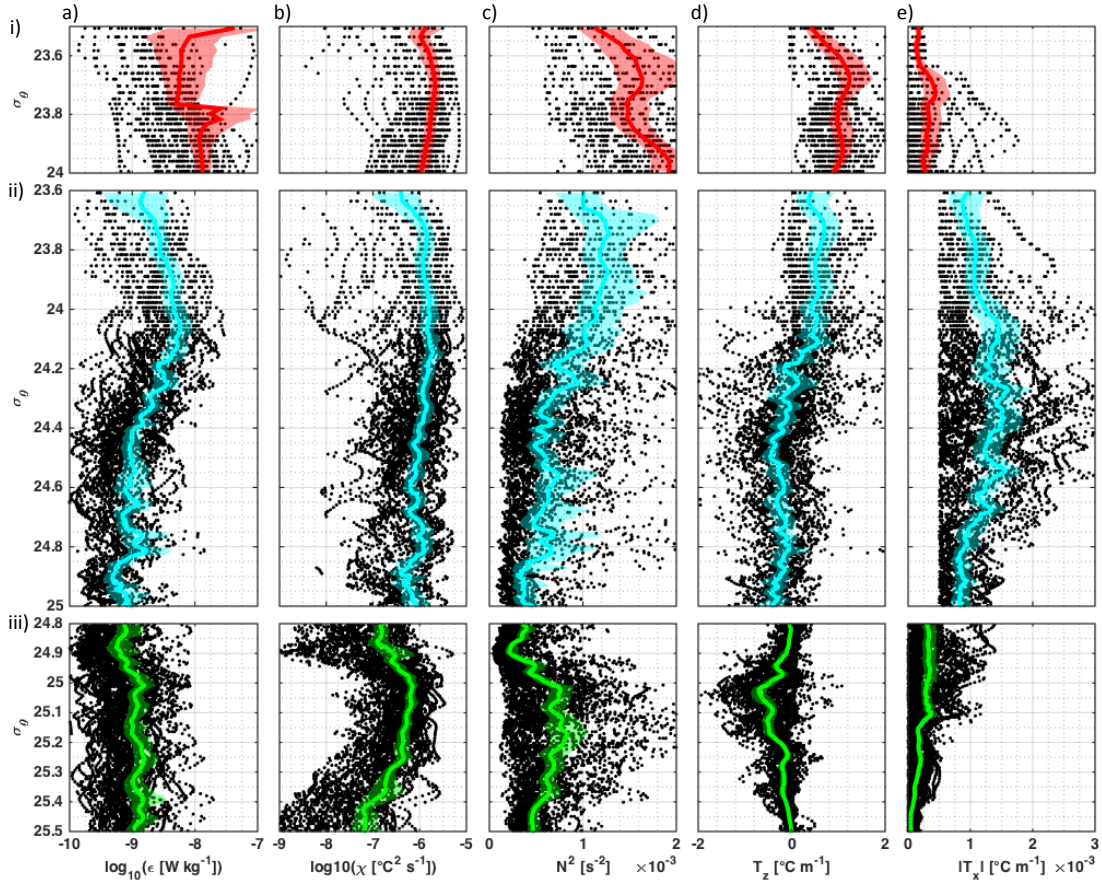

Figure 3.9: Raw data and average profiles of (a) ε, (b) χ, (c)N^2, (d) $\frac{\partial T}{\partial z}$, and (e) $\overline{\frac{\partial T}{\partial x}}$ in boxes at the (i) top, (ii) sides, and (iii) bottom of the eddy. The lateral thermal gradient is never less than 5×10^{-4} °C m^{-1} in the lateral region due to the definition of the lateral mixing region. Density ranges approximately correspond to 25-40 m (top), 30-70 m (sides), and 60-90 m (bottom). Bootstrapped 95% confidence intervals for each isopycnal bin are shaded. The lateral thermal gradient is smoothed laterally, so that results between profiles are correlated, reducing calculated sampling error.

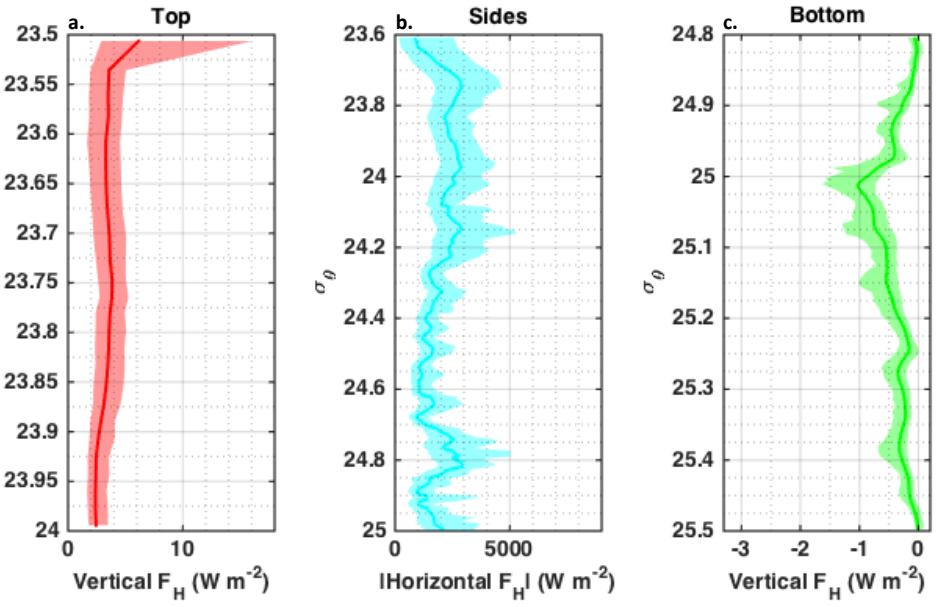

Figure 3.10: Heat fluxes calculated from averaged quantities shown in Fig. 3.9 for the (a) top, (b) sides, and (c) bottom edges of the eddy. Density ranges approximately correspond to 25-40 m (top), 30-70 m (sides), and 60-90 m (bottom). Bootstrapped 95% confidence intervals are shaded; note that these intervals are generally within the factor of 2-3 uncertainty associated with measurements of ε and χ.

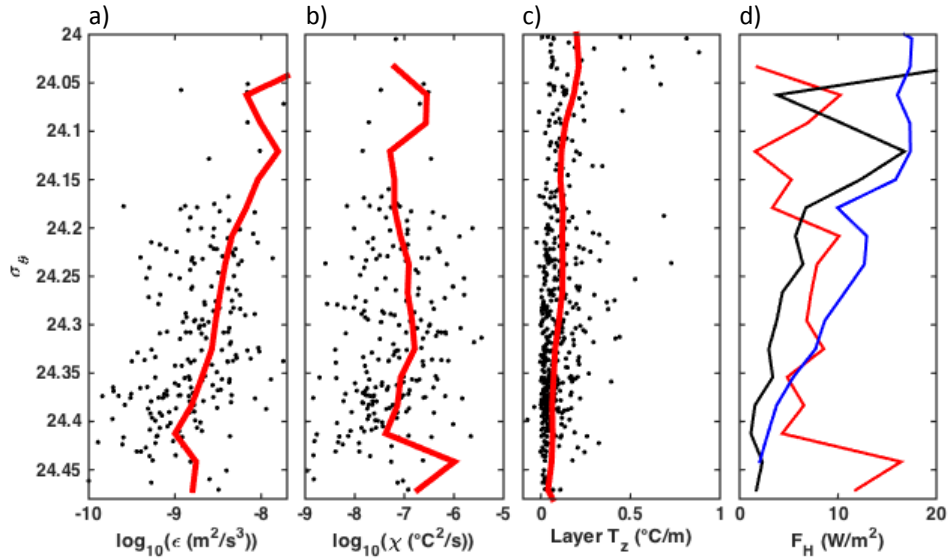

Figure 3.11: Quantities averaged within diffusive layers at the top of the eddy. (a) ε calculated within layers, (b) χ calculated within layers, (c) $\frac{\partial T}{\partial z}$ within layers (used along with ε and χ within layers to calculate heat fluxes within each layer) (d) F_ε (black), F_χ (red), and $F_{4/3}$ (blue).

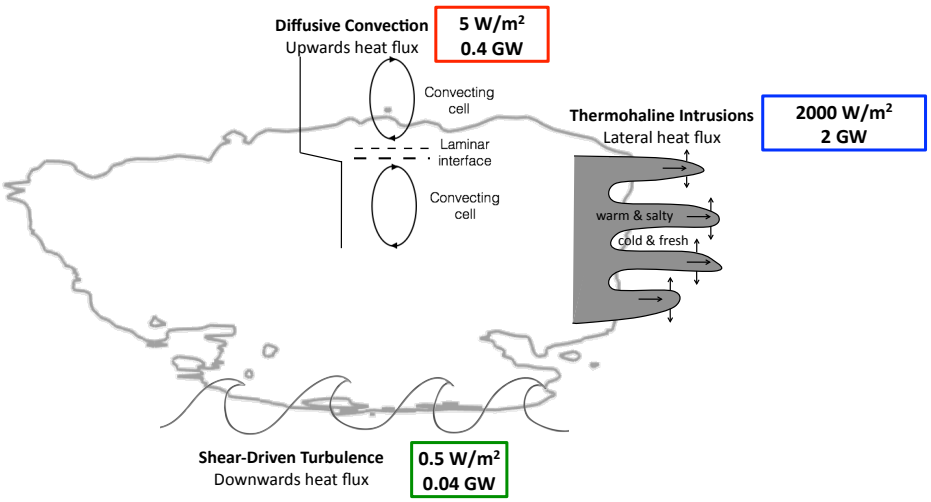

Figure 3.12: Schematic diagram of the eddy, indicating diffusive convection at its top, lateral intrusions at its sides, and shear-driven turbulence at its bottom. Estimated heat fluxes and transports due to each process are noted.

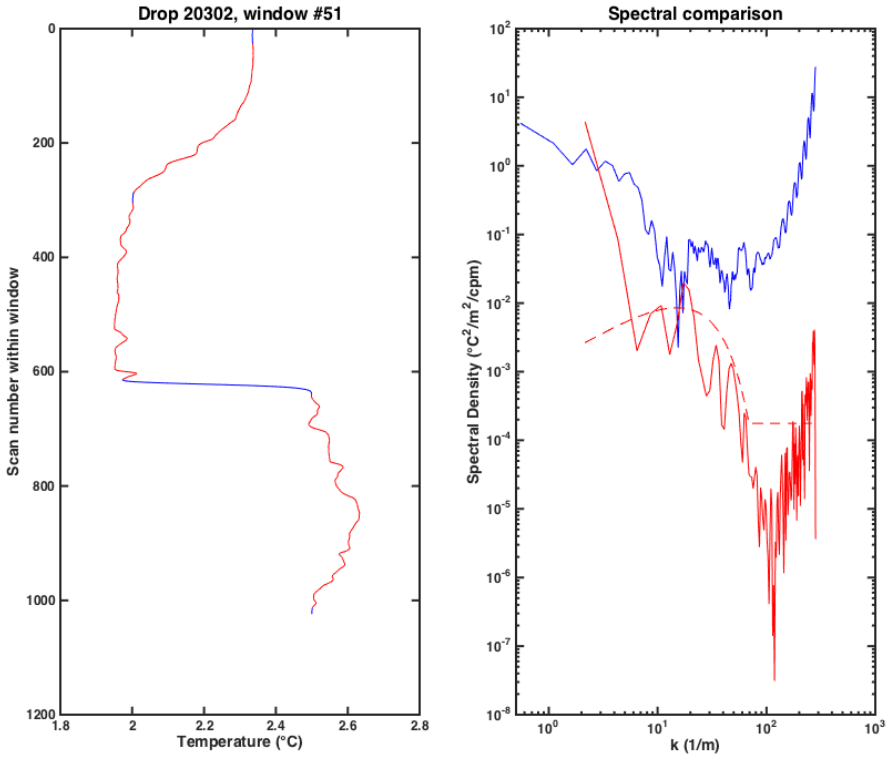

Figure 3.13: A1: Example window in which estimates of χ did not converge due to the sharp step within the sampled window. The left hand panel shows the thermistor temperature over the full window (blue), while the red sections represent the region in which χ was recalculated using handpicked windows. The original spectrum (blue) and the spectrum taken over the upper subwindow (red) are shown on the right, along with the MLE fit to the latter (red, dashed). The MLE method does not converge for the spectrum taken over the entire original window. Integrating under the spectrum over the full original window results in an estimate for χ that is two orders of magnitude higher than that obtained by taking the weighted average of the hand selected windows.

Chapter 4

Mixing of Pacific Summer Water intrusions, eddies, and filaments in the Beaufort Sea

4.1 Introduction

Pacific Water enters the Chukchi Sea via the Bering Strait at an annual mean rate of approximately 0.8 Sv. From there, about 0.5 Sv enters the Canada Basin via Barrow Canyon (Itoh et al., 2013; Corlett and Pickart, 2017). During the summer and autumn months, significant quantities of heat are transported into the Canada Basin along this route–Itoh et al. (2013) estimate annual averages from 2000 to 2008 of 1-3 TW, with substantial interannual variability. Much of this heat is carried in two boundary currents, the Beaufort Shelfbreak Jet and the Chukchi Slope Current (von Appen and Pickart, 2012; Brugler et al., 2014; Corlett and Pickart, 2017). These inflows feed into the upper halocline layer of the Canada Basin, forming Pacific Summer Water, generally characterized by salinities from 30 to 33. This water mass lies above the cold halocline Pacific Winter Water, beneath which sits the warm Atlantic Water, forming a deeper

warm halocline. From 1987-2017, the heat content within the 31 to 33 salinity range has nearly doubled (Timmermans et al., 2018).

While the implications of this increased heat are not fully understood, there is spatial correlation between regions that are now ice free in the summer and increased temperatures in the warm halocline, implying that warm PSW may play a role in melting Arctic sea ice (Timmermans et al., 2018). Shimada et al. (2006) proposed a feedback mechanism in which warmer PSW in the spring results in earlier melting of landfast sea ice on the north coast of Alaska. This opens the Beaufort sea to wind forcing, which tends to draw more PSW into the basin. However, the mechanism by which PSW influences sea ice is not obvious. While significant heat is stored in PSW, mixing rates in the stratified western Arctic are generally quite low, and shallow mixed layers with strong haloclines limit vertical heat fluxes from the deeper PSW (Fer, 2009; Toole et al., 2010; Jackson et al., 2010).

Sparse observations have captured episodic intrusions of PSW into the Canada Basin that result in substantial upward heat fluxes. These include warm anticylonic eddies (Kawaguchi et al., 2012; Fine et al., 2018) and less organized filaments or intrusions (Kawaguchi et al., 2014; Timmermans and Jayne, 2016). In these events, double diffusive heat fluxes are significant [$\mathcal{O}$(1-10 W m^{-2})]. In 2018, the most significant such event yet documented resulted in upwards heat fluxes of $\sim$ 100 W m^{-2} (MacKinnon et al., 2019). All of these events contained Alaskan Coastal Water (ACW), the warmest and freshest variety of PSW, which forms along the coast of Alaska in the summer. These events demonstrate that under the right conditions, Pacific-origin heat may be carried into the mixed layer and potentially affect sea ice. However, as these events generally have very weak surface expression and are transient in nature, it is challenging to assess the frequency with which they occur and their ultimate impact on vertical heat transport. Given that the strong double diffusion associated with substantial heat fluxes is only expected to occur over intrusions with substantial thermohaline gradients (e.g., Kelley et al. (2003)), a crucial question is how the stirring proccesses that distribute PSW heat laterally and set these

initial gradients interact with double diffusion and other vertical mixing processes to mediate vertical heat transport rates.

In the current study, we use the most expansive microstructure dataset in the western Arctic to date to specifically address the interplay between lateral stirring and vertical mixing processes in PSW intrusions. We begin with an examination of these processes in a particularly well-resolved ACW intrusion actively undergoing both lateral stirring and vertical mixing. Using insight developed from this analysis, we return to the entire dataset to expand and extrapolate on the relationship between lateral and vertical processes.

4.2 Methods

Observations were made onboard the R/V *Sikuliaq* during the September 2015 NSF-funded ArcticMix and the September 2018 ONR-funded Stratified Ocean Dynamics of the Arctic (SODA) process cruises. Fifteen microstructure surveys were conducted in the Canada Basin over the two cruises (Fig. 4.1a).

Microstructure measurements were made using the Modular Microstructure Profiler (MMP). The MMP is a loosely-tethered free-falling turbulence profiler developed by M. C. Gregg at the Applied Physics Laboratory of the University of Washington. The MMP falls at nominally 0.6 m s^{-1}, and carries two custom-built shear probes, an FP07 thermistor, a Seabird CTD, and an altimeter. The TKE dissipation rate (ε) is calculated by iteratively fitting a Panchev curve to shear spectra calculated over 2.5 second (1-2 m) windows.

We will focus particularly on a warm intrusion observed on the 26th of September 2018 during a transect traveling westwards from the Canada Basin toward the Chukchi slope (Fig. 4.1a inset). The survey was conducted at 73.37 ° N, 158.63 °W over 6.5 hours.

4.3 Results

4.3.1 Temperature, Salinity, water masses

The 2015 ArcticMix cruise and the 2018 SODA cruise both collected microstructure profiles over similar areas of the western Arctic (Fig. 4.1a). In T-S space, some patterns across both years emerge (Fig. 4.1b and c). In both years, the transition from warm PSW to the cold PWW halocline occurred between salinities of 32 to 33, while the transition from cold PWW to the warmer AW occurred at salinities of 33 to 34. Peaks of the warmest PSW were found around 30.5 psu. In 2018 this temperature peak was warmer and spanned a larger range of isohalines, partially due to a large warm intrusion described in MacKinnon et al. (2019), while in 2015 this temperature peak was made up of samples collected from a warm-core eddy (Fine et al., 2018). In the ArcticMix data, there is a clear distinction between a near surface temperature maximum (Jackson et al., 2010; Timmermans et al., 2014) containing water fresher than 28.5 and saltier PSW, while in the SODA data this distinction is blurry. We identify twelve surveys over the two cruises that contained PSW, which we define here as water warmer than 0 °C with salinity between 28.5 to 32. This cutoff is determined from the T-S plots which show no temperatures above 0 °C in the 32 to 33 salinity range.

Along the same isopycnals as the T-S peak formed by the ACW temperature maximum, there are many data points with intermediate T-S characteristics between the very warm ACW and the coldest waters on the these isopycnals that were observed in these surveys. This is true over both the ArcticMix and SODA data sets. This suggests that in both cases, the warmest waters observed were in the process of stirring and mixing with the resident basin water. The aim of this study is to use the available data to build understanding of the processes that control these mixing rates and how these processes may be affected by increasingly warm PSW. To this end, we begin with an analysis of the thermohaline structure and associated mixing in an intrusion observed in the Chukchi Slope Current (CSC) in September 2018.

4.3.2 Intrusion Temperature, Salinity, water masses

The CSC intrusion contained water reaching temperatures of 7 °C, with a salinity of approximately 30.5 (Fig. 4.2a and b), consistent with the T-S properties of ACW. Significant fine structure was associated with this temperature maximum, with complicated layering between warm ACW and cool background Arctic water. While some of this structure was reflected in isopycnal displacement, to a large degree the T-S structure was density compensated. Relatively warm and salty coherent structures crossed isopycnals (Fig. 4.2a and b).

The complex thermohaline structure resulted in double diffusive instabilites. These instabilities can be identified using the density ratio

$$R_\rho = \frac{\beta \Delta S}{\alpha \Delta T} \tag{4.1}$$

in which α and β are the thermal expansion and haline contraction coefficients, and $\Delta S/\Delta T$ is the ratio of the vertical gradient of salinity to the vertical gradient of temperature (Fig. 4.2c). In this analysis gradients are calculated over 0.25 m depth bins and smoothed in the vertical by 2 m. Double diffusive instabilities may occur where $R_\rho > 0$, that is, when both temperature and salinity either increase or decrease in depth ($R_\rho < 0$ indicates either double stability or gravitational instability). A vertical profile is unstable to double diffusive convection where $R_\rho > 1$, and is unstable to salt fingering where $0 < R_\rho < 1$. Strong double diffusive convection occurs where $1 < R_\rho < 10$, while strong salt fingering occur where $1/2 < R_\rho < 1$. Coherent double diffusive staircases are usually only found in regions of strong instability (Kelley et al., 2003; Bebieva and Timmermans, 2015).

Over the intrusion, R_ρ has complex small-scale structure, with regions of strong salt fingering and strong double diffusive convection occurring on scales as small as 1 m. Double diffusive convective/salt fingering instabilities occur above/below local temperature maxima. The small scale layers in R_ρ highlight the complexity of vertical gradients in both temperature and

salinity associated with the largely density-compensated structure of the intrusion.

4.3.3 Velocity/dynamics

The study region is at the transition from the Canada Basin onto the Chukchi slope (Fig. 1a). The CSC is a surface-intensified current that runs through this region to the northwest, consistent with strong cross-track velocity (Fig. 4.1a inset and 4.3a and b, (Corlett and Pickart, 2017)). Flow is intensified towards the surface, consistent with other CSC observations. Vertical shear is intensified in a layer from 10 to 30 m beneath the surface (Fig. 4.3c and d). Beneath 20 m, the northwest flow is somewhat relaxed. However, it picks up around 80 m, with a corresponding deeper shear layer. Geostrophic crosstrack shear shows qualitative similarities, although the geostrophic shear is about three times weaker than measured shear (fig. 4.3e).

4.3.4 Turbulence and Mixing

The Richardson number $Ri = N^2/|\mathbf{U_z}|^\mathbf{2}$ indicates susceptibility to shear instabilities. We interpolate CTD and microstructure data onto the same grid as velocity and smooth all quantities over 4 m in the vertical and 0.5 km in the horizontal to compare these data. Total vertical shear $|\mathbf{U_z}|^\mathbf{2} = \mathbf{U_z^2} + \mathbf{V_z^2}$ was elevated along the intrusion (Fig. 4.4a). The buoyancy frequency N^2 showed structure similar to shear (Fig. 4.4b), while low Ri (high Ri^{-1}) highlights areas of shear instability along the top edge of the intrusion (Fig. 4.4c).

The intrusion was characterized by elevated rates of turbulent kinetic energy dissipation (ε). The intricate T-S structure was reflected in ε, with elevated ε along thermohaline gradients and in double diffusively unstable regions (Fig. 4.2d). The burst of high inverse Richardson number around 20 m deep at 7 km is also characterized by high ε (Fig. 4.4d).

In T-S space, a primary temperature peak appears at 7 °C and 30 salinity, with a slightly fresher peak at 5.5 °C (Fig. 4.5). An additional cooler and saltier peak occurs at 2 °C and 31

salinity. This cooler peak has a salinity just over 31, and indicates the presence of a second PSW water mass, summer Bering Sea Water (sBSW, (Timmermans et al., 2014)). Turbulent dissipation rates are relatively high above T-S peaks (Fig. 4.5a). The inverse Richardson number is rarely unstable in these areas, with most instability at the top and base of the intrusion (Fig. 4.5b). However, double diffusive convective instabilities are common in the regions of high ε (Fig. 4.5c). Mixing is generally low where the water column is double-diffusively stable, except at salinities less than 28 where mixed layer dynamics are present.

4.4 Discussion

4.4.1 Mixing processes

Observed R_ρ (Fig. 4.2c) and Ri (Fig. 4.4c) indicate that both shear instabitilies and double diffusive instabilities occur along the intrusion. In this section we will argue that both types of instability cause elevated ε and corresponding mixing. We examine the effect of each process by binning ε based on stability criteria and considering the resulting distributions.

Shear instability

High ε values where Ri^{-1} is high (Fig. 4.4c and d) suggest that shear instability plays a role in generating mixing. We bin ε values based on Ri, defining $Ri \leq (\geq)3$ as "small (big) Ri", and calculate probability density functions (PDFs) and histograms based on $\log_{10}(\varepsilon)$ for all measurement bins between 15 m and 75 m. The probability density functions indicate slightly higher ε associated with low Ri, as expected (Fig. 4.6i.a). The histograms emphasize that shear instability was relatively rare throughout the survey, with shear-stable bins making up a majority of measurements (Fig. 4.6ii.a).

Double diffusive instability

There are two distinct types of double diffusive instability, double diffusive convection (DDC) and salt fingering (SF), which form above and below warm salty intrusions respectively. Each of these instabilities can be either strong or weak, with coherent staircase formations generally only occurring in regions with strong instabilities. Binning $\log_{10}(\varepsilon)$ values based on double diffusive stability criteria (i.e., Fig. 4.2c) reveals a relationship between ε and double diffusive stabilitiy. Double stability and weak DDC are both associated with lower ε, while strong DDC is associated with higher ε (Fig. 4.6i.b). Both weak and strong SF are associated with intermediate ε. A histogram reveals that DDC bins account for a majority of measurements, while SF is relatively rare (Fig. 4.6ii.b). DDC particularly accounts for a majority of the bins with elevated ε, suggesting that this process plays an important role in setting mixing rates.

Interplay between shear instabilities and double diffusion

To compare the influence of shear instabilities and double diffusive instabilities, we interpolate temperature and salinity onto the same grid as shear. Following St. Laurent and Schmitt (1999), we bin ε values by both *Ri* and double diffusive stability between 15 and 65 m (below 65 m, *Ri* is suspect due to noise in shear). For this analysis, strong and weak SF and DDC are all treated as double diffusive instability. Considering the resulting four PDFs, some patterns emerge (Fig. 4.6i.c). Bins which are stable to both double diffusion and shear instabilities are associated with the lowest values of ε ($\langle\varepsilon\rangle = 1.0 \times 10^{-9}$). Bins that are stable to double diffusion but subject to shear instabilities have only slightly higher mean ε values ($\langle\varepsilon\rangle = 1.3 \times 10^{-9}$). Double diffusive unstable bins are associated with higher values of ε ($\langle\varepsilon\rangle = 1.5 \times 10^{-9}$), with bins subject to both double diffusive and shear instabilites having the highest mean ($\langle\varepsilon\rangle = 2.2 \times 10^{-9}$). A small secondary peak is apparent in bins that are double diffusively stable but susceptible to shear instabilities at $\log_{10}\varepsilon = -7$. These bins are associated with the isolated burst of shear-driven turblence around 20 m deep.

A stacked histogram emphasizes the dominant role of double diffusion in setting mixing rates (Fig. 4.6ii.c). The vast majority of bins are not subject to shear instabilities, but many experience double diffusive instabilities, particularly at higher values of $\log_{10}\varepsilon$. Thus, while shear instabilities are responsible for some of the highest values of ε, these events are so rare (even in this relatively high-shear environment) that double diffusion is a more important factor overall. Considering the nondimensional buoyany Reynolds number $Re_\nu = \varepsilon/(\nu N^2)$ provides another interpretation of these results. Active turbulence occurs where $Re_\nu > 100$, which happens in 9% of the bins in the survey. Of those 9%, the proportion that falls within each type of instability is given in Table 4.1. Only 9% of these bins experience shear instabilities, while 64% experience double diffusive instabilities. The 30% of actively turbulent bins that are not susceptible to either instability emphasize the limitations of this analysis. Active turbulence can be the result of shear instabilities on scales smaller than the resolution of our ADCP, or can persist after mixing has resulted in a doubly stable profile or the large scale shear has dissipated (Gibson, 1987). In such cases, the ultimate cause of the turbulence cannot be determined from the current survey.

While this analysis suggests that DDC is the dominant cause of small-scale turbulent mixing, there is another possible interpretation of these results. The thermohaline gradients that define the contours of the intrusion may be subject to strong shear due to the lateral stirring of the intrusion. These vertical scales are too small to be resolved by the ADCP observations, and without higher resolution shear measurements it is impossible to eliminate this hypothesis. However, due to the strong double diffusive instabilities identified along these gradients and the separation in PDFs based on the type of double diffusive instability, we suspect that double diffusion plays a substantial role in setting rates of vertical heat flux. In either case, the result is elevated mixing along high thermal gradients, resulting in a net transport of heat out of the warm intrusion.

4.4.2 Basin significance

Within the intrusion discussed above, we concluded that lateral stirring results in double diffusively unstable thermohaline structure as well as potentially elevated shear along these structures, facilitating a net heat flux from the warm intrusion to the surrounding water. The ultimate result of this heat transport is water mass modification as the temperature anomaly of the intrusion erodes.

How common is this dynamic (lateral stirring resulting in increased turbulent mixing along PSW intrusions) in a basin-wide sense? In the following section, we use twelve MMP surveys that sampled PSW, collected over both the ArcticMix and SODA cruises, to explore the relationship between the vertical structure of an intrusion and its efficiency in mixing the intruding PSW into the cold resident water.

Normalized heat transport

To compare mixing rates of PSW across multiple surveys, we define a normalized heat transport. PSW intrusions are primarily characterized by their temperature anomalies, due to the western Arctic's halocline stratification (while PSW intrusions also have salinity signatures these are a much smaller relative anomaly). Quantifying the heat transport out of a given intrusion represents a metric for the mixing of PSW associated with that intrusion. Accurately determining the total heat transport from a given warm intrusion is difficult considering that the horizontal spacing of the MMP profiles is large relative to the scale of horizontal structure, and most intrusions are only sampled in one lateral direction. In light of these limitations, a normalized heat transport with units of W m^{-2}, representing the average heat transport observed in each MMP profile, is used as a metric for comparision. This quantity is calculated as follows:

1. Calculate N^2 and T_z as first-differences over the 0.25 m bins. N^2 is calculated from sorted density profiles and smoothed over 2 m. In the current analysis, we are interested in PSW,

so we restrict the salinity range considered from 28.5 to 32. We additionally restrict the analysis to depths beneath 30 m, as mixed-layer processes can dominate shallower mixing.

2. For each profile, bin ε, N^2, and $|T_z|$ based on temperature.

3. Within each isothermal bin, calculate $\langle\varepsilon\rangle$, $\langle N^2\rangle$, and $\langle T_z\rangle$. For $\langle\varepsilon\rangle$ and $\langle N^2\rangle$, both of which are lognormally distributed, means are calculated as 10 to the power of the mean of $\log_{10}$ of the quantity (i.e., the geometric mean).

4. Within each isothermal bin, calculate a heatflux $F_H(\theta) = \rho C_p \langle T_z\rangle \Gamma \langle\varepsilon\rangle / \langle N^2\rangle$, in which $\rho = 1025$ kg m^{-3} is density, $C_p = 4000$ J kg^{-1} °C^{-1} is heat capacity, and Γ is the mixing efficiency. For this analysis, we set $\Gamma = 1$, as shear-driven mixing is generally quite low in the western Arctic and we assume double diffusive mixing dominates along warm intrusions. This assumption is supported by the CSC intrusion analysis above suggesting that most mixing occurs due to double diffusion, as well as analysis of a warm eddy sampled during the ArcticMix cruse (Fine et al., 2018).The units of $F_H(\theta)$ are W m^{-2}. (Note that this is very similar to the recipe for the flux of a scalar quantity described in Winters and D'Asaro (1996). It differs in that the thermal gradient $\langle T_z\rangle$ is calculated *in situ*, rather than from Thorpe-sorted depth.)

5. For each isothermal bin, multiply the mean heat flux $F_H(\theta)$ across that isotherm by the average number of times that isotherm appears in for each profile. This converts the heat flux (heat transport per surface area of each isotherm) into a normalized heat transport (heat transport per surface area sampled by each MMP profile).

6. Take the geometric mean of the normalized heat transport values calculated for each isotherm to obtain the mean normalized heat transport over a given isothermal range.

This procedure results in a well-defined average heat transport between isotherms per square meter of ocean.

Quantifying vertical structure

The complexity of the thermal gradient T_z is a reasonable proxy for the complexity of the thermohaline vertical structure, as temperature varies much more than salinity due the strong halocline in the western Arctic. In the simplest case of a single warm layer, T_z would vary smoothly from a positive to a negative value. In more complex structures, T_z may vary sharply.

To remove the influence of slowly varying background, we fit a polynomial T_{zfit} to T_z, and take $T_{zres} = T_z - T_{zfit}$. To quantify the variability of T_{zres} over a given profile, we take its root-mean-squared value T_{zrms}. We treat this quantity as a metric for the complexity of the vertical structure of a given profile.

Relationship between heat transport and vertical structure

There are at least two factors that would tend to result in higher heat transport between PSW and background water in intrusions with a more complicated vertical structure. First, complicated vertical structure results in more surface area for any given isotherm. Much like the ribs of a radiator, more surface area implies more opportunity for heat exchange, even if the heat flux along each surface is relatively low. Secondly, intrusions with complex vertical structure are likely to have higher vertical mixing rates due to double diffusion. Complex structure in T-S space results in vertical profiles that alternate between cold/fresh and warm/salty water parcels. On either side, these parcels may be double diffusively unstable. Additionally, the layering that occurs in complex structures may indicate the presence of small-scale vertical shear. Both double diffusive instabilities and vertical shear tend to increase mixing rates.

To examine the relationship between heat transport and vertical structure, we consider 12 surveys taken over both the SODA and ArcticMix process cruise using the MMP. For each survey, we calculate $\langle T_{zrms} \rangle$ averaged over the survey. Using 0.5 °C width bins from 0 to 4 °C, we additionally calculate the mean normalized heat transport between these isotherms for the entire survey. There is a linear relationship between the $\log_{10}$ of the normalized heat flux and

T_{zrms} ($R^2 = .77$ excluding a single outlier, Fig. 4.7a).

Physical Interpretation

The normalized heat transport is controlled by $\langle \log_{10}(\varepsilon) \rangle$, $\langle \log_{10}(N^2) \rangle$, $\langle |T_z| \rangle$, and the number of times an isotherm is seen in an average profile ($\langle iso\# \rangle$), in which angled brackets represent quantities averaged over the isotherms of interest within each survey. Many of these factors are independently correlated with $\langle T_{zrms} \rangle$ (Fig. 4.7b-e).

The positive correlation between $\langle \log 10(\varepsilon) \rangle$ and $\langle T_{zrms} \rangle$ ($R^2 = 0.64$) has two possible explanations. First, profiles with complex vertical thermohaline structure tend to be susceptible to double diffusion, resulting in elevated mixing. A second possibility is that complex vertical structure may be associated with small scale vertical shear, if the structure is generated by active lateral stirring. Vertical shear would also tend to increase the mixing rates associated with this structure.

A positive correlation also exists between $\langle |T_z| \rangle$ and $\langle T_{zrms} \rangle$ ($R^2 = 0.64$), although it is ambiguous whether this correlation is physically signficant. In general, a profile with larger $\langle |T_z| \rangle$ is likely to have higher $\langle T_{zrms} \rangle$ simply because T_z changes sign above and below intrusions. Complex vertical structure may be associated with sharper gradients if lateral stirring acts to sharpen gradients that relax due to local mixing, however, the current analysis is not able to conclude whether such a process occurs over this data set.

Finally, a positive association between $\langle iso\# \rangle$ and $\langle T_{zrms} \rangle$ ($R^2 = 0.67$) may be understood as the result of lateral stirring increasing the surface area of individual isotherms. A more complex vertical profile is characterized by "wiggliness" of the temperature profile, providing more surfaces for heat exchange between water masses.

This analysis has identified three possible processes by which lateral stirring acts to increase small scale vertical heat fluxes out of PSW intrusions. Lateral stirring stretches and folds isotherms, creating more surface area for heat exchange. Stirring may additionally sharpen thermal

gradients along isotherms. Finally, turbulent mixing along isotherms is enhanced, either due to double diffusion associated with enhanced temperature gradients, or due to shear instabilities along regions with high thermal gradients.

4.5 Summary and future work

Microstructure, CTD, and velocity data collected in a warm CSC intrusion capture active turbulent mixing along the thermohaline gradients associated with the intrusion. Statistical analysis of ε and turbulent instability criteria suggests that double diffusive convection plays a dominant role in setting these relatively high mixing rates.

An analysis of microstructure surveys taken over 12 warm intrusions in both 2015 and 2018 finds an association between complex thermal structure and elevated transport of heat out of warm intrusions. This association is due to three separate factors: the stretching of isotherms that occurs due to lateral stirring, the sharpening of thermal gradients associated with lateral stirring, and the increase in ε due to either double diffusive instabilities associated with high temperature gradients or shear due to lateral stirring.

The linear association between thermal structure and both heat transport and mixing rates may allow for the parameterization of turbulent fluxes from temperature profiles. The SODA and ArcticMix process cruises both included many high-resolution CTD transects, providing ample opportunity to put these new ideas into practice. Additionally, autonomous drifters including both ARGO-style ALAMO floats and ice-tethered profilers have been deployed in the western Arctic, providing CTD profiles over a much broader spatial area.

Pacific Summer Water intrusions may play a crucial role in setting local oceanic turbulent heat fluxes. Microstructure data collected in September of 2015 and 2018 demonstrates a relationship between the vertical structure of these intrusions and the mixing rates associated with them. This relationship may prove useful in assessing the impact of such intrusions on the

Table 4.1: Percent of bins characterized by active turbulence ($Re_\nu > 100$) subject to double diffusive and shear instability criteria.

	Double Diffusive	**Doubly Stable**	**Total**
$Ri < 3$	4%	5%	9%
$Ri > 3$	60%	31%	91%
Total:	64%	36%	

marginal ice zone, and in monitoring changes in the mixing rates of such intrusions as PSW continues to warm.

4.6 Acknowledgments

This work was supported by ONR grant N00014-16-1-2378 and NSF grants PLR 14-56705 and PLR-1303791 and by NSF Graduate Research Fellowship grant DGE-1650112.

We gratefully acknowledge the *Sikuliaq* captain and crew, MOD engineering team, and SODA collaborators who made this study possible. We are additionally grateful to Mike Gregg, Peter Winsor, Mary-Louise Timmermans, Yueng-Djern Lenn, and Rob Pinkel, for scientific support and insight; and to Mike Gregg, Dave Winkel, Amy Waterhouse, and Sam Fletcher for supporting the transition of the MMP instrumentation from APL/UW to SIO.

Microstructure data are available for download at https://microstructure.ucsd.edu.

Chapter 4, in full, is being prepared for submission for publication. Fine, Elizabeth; MacKinnon, Jennifer A.; Alford, Matthew H.; Mickett, John B.; Peacock, Thomas; le Boyer, Arnold. The dissertation author was the primary investigator and author of this paper.

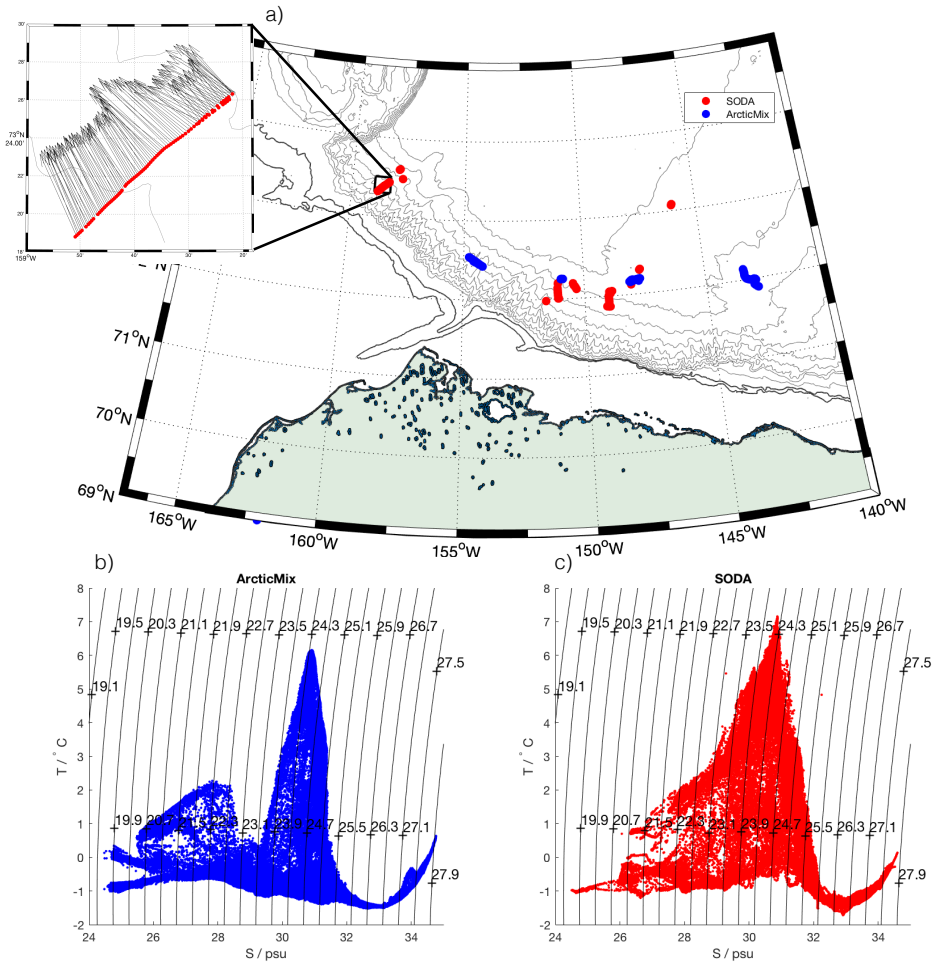

Figure 4.1: a) Map of the survey region showing locations of MMP profiles during the 2018 SODA cruise (red) and 2015 ArcticMix cruise (blue). Inset highlights the 2018 Chukchi Slope Current survey, with mean velocity vectors from 15 to 80 m. b) T-S diagrams for all Canada Basin MMP profiles collected during the 2015 ArcticMix cruise c) T-S diagrams for all Canada Basin MMP profiles collected during the 2018 SODA cruise

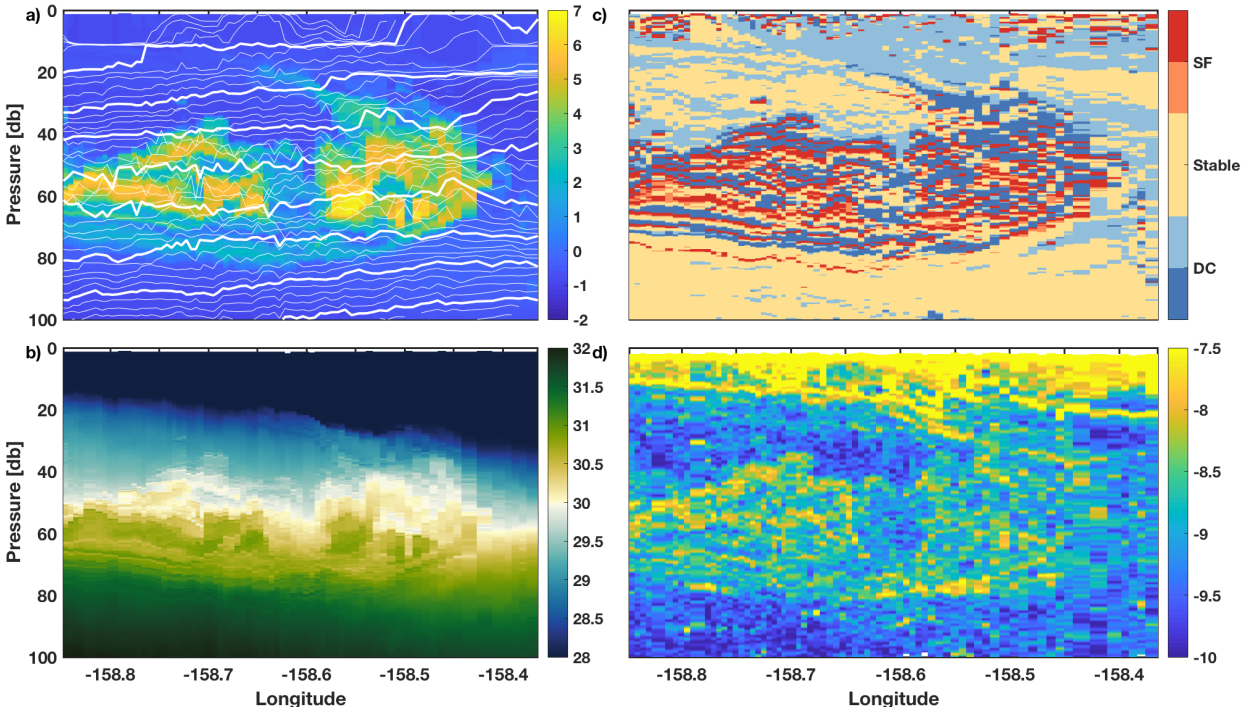

Figure 4.2: a) Temperature (°C) with isopycnals in white, b) salinity, c) double diffusive stability, and d) $\log_{10}(\varepsilon(\mathrm{W\ kg^{-1}}))$ measured during the CSC intrusion microstructure survey.

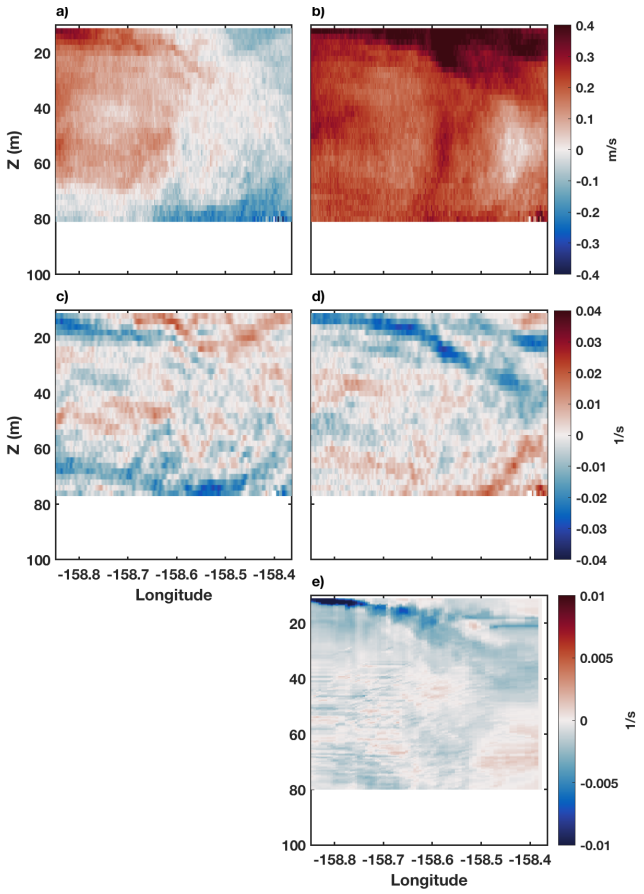

Figure 4.3: Measured velocity from the shipboard ADCP during the CSC intrusion survey a) along and b) across the ship track; measured shear from the shipboard ADCP during the CSC intrusion survey c) along and d) across the ship track; e) cross track geostrophic shear calculated from MMP survey.

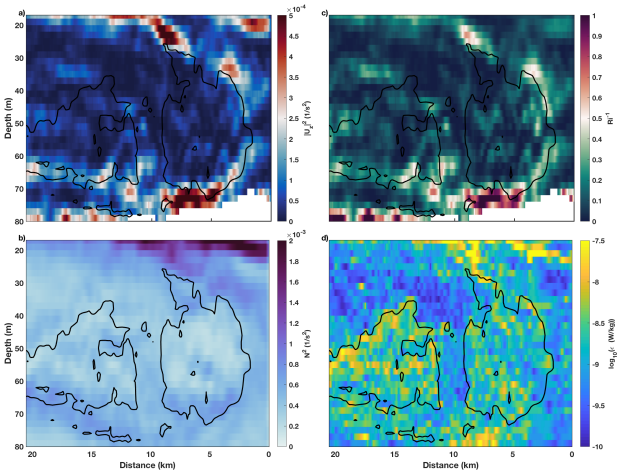

Figure 4.4: a) $|U_z|^2$, b) N^2, c) Ri^{-1}, d) $\log_{10}(\varepsilon)$ measured during the CSC intrusion survey, all interpolated onto the same grid as the ADCP velocity and smoothed over 4 m in the vertical and 0.5 km in the horizontal.

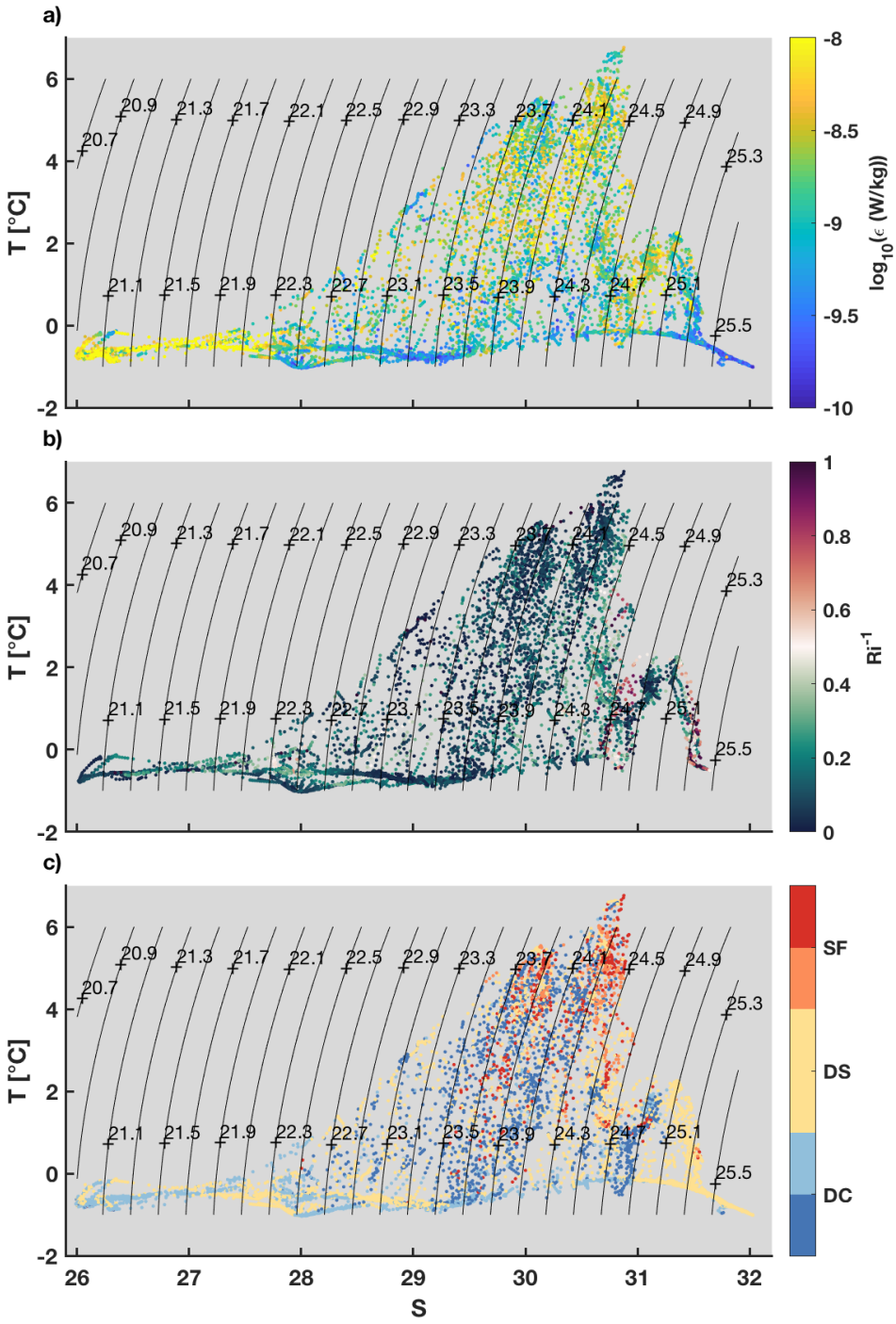

Figure 4.5: Temperature (° C) and salinity colored by: a) $\log_{10}(\varepsilon(\mathrm{W\ kg^{-1}}))$, b) Ri^{-1}, and c) double diffusive stability.

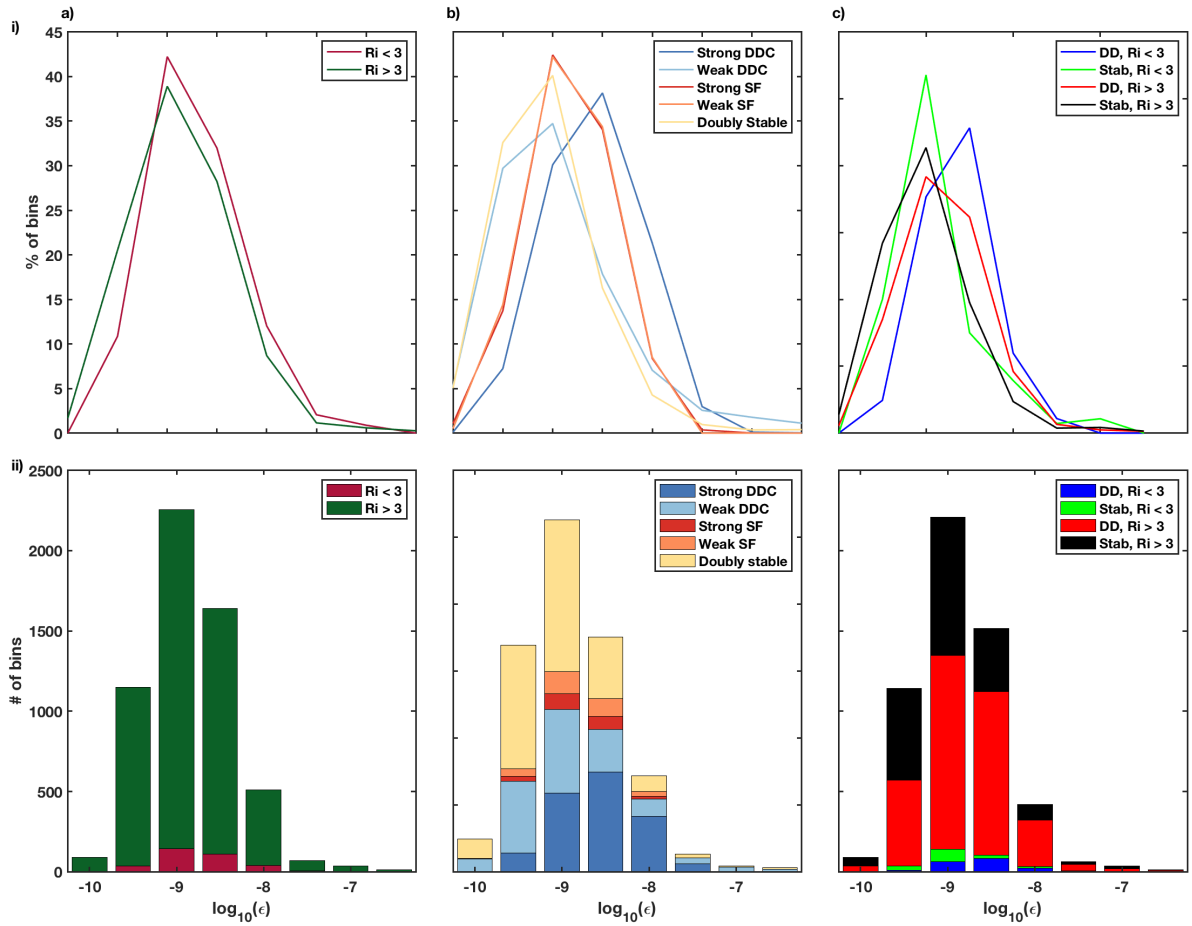

Figure 4.6: i) PDFs and ii) stacked histograms of $\log_{10}(\varepsilon)$ binned by a) *Ri*, b) double diffusive stability, and c) both *Ri* and double diffusive stability.

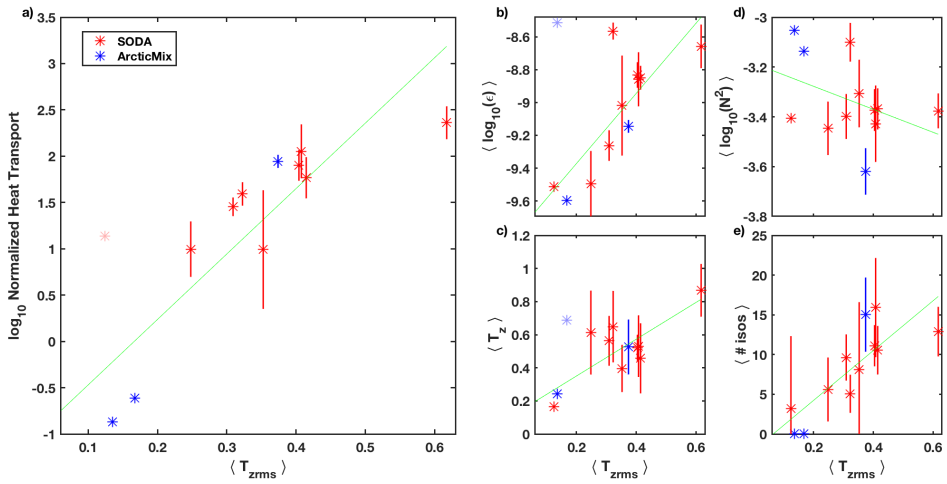

Figure 4.7: Quantities averaged over SODA and ArcticMix surveys at salinities less than 32, for temperatures from 0 to 4 °C. Averages over SODA surveys are shown as red stars and ArcticMix surveys as blue stars. Linear regression best fit lines are shown in green, with outliers (denoted as light red and blue stars for the SODA and ArcticMix data respectively) excluded from the regression. Error bars are given as the mean over all iostherms plus or minus the standard deviation over all isotherms, except in cases where only one isotherm within the 0 to 4 °C range appeared in the survey. a) The $\log_{10}$ of normalized heat transport as a function of $\langle T_{zrms} \rangle$ (see text for definitions of both quantities, $R^2 = 0.77$). b) $\langle \log_{10}(\varepsilon) \rangle$ as a function of $\langle T_{zrms} \rangle$, ($R^2 = 0.64$) c) $\langle T_z \rangle$ as a function of $\langle T_{zrms} \rangle$, ($R^2 = 0.64$). d) $\langle \log_{10}(N^2) \rangle$ as a function of $\langle T_{zrms} \rangle$, ($R^2 = 0.16$). e) $\langle \#isos \rangle$ as a function of $\langle T_{zrms} \rangle$, (see text for definition, $R^2 = 0.67$)

References

M. H. Alford. Internal swell generation: The spatial distribution of energy flux from the wind to mixed-layer near-inertial motions. *J. Phys. Oceanogr.*, 31(8):2359–2368, 2001.

M. H. Alford. Improved global maps and 54-year history of wind-work on ocean inertial motions. *Geophys. Res. Lett.*, 30(8):1424–1427, 2003.

M. H. Alford and M. C. Gregg. Near-inertial mixing: Modulation of shear, strain and microstructure at low latitude. *J. Geophys. Res.*, 106(C8):16947–16968, 2001.

M. H. Alford, M. F. Cronin, and J. M. Klymak. Annual Cycle and Depth Penetration of Wind-Generated Near-Inertial Internal Waves at Ocean Station Papa in the Northeast Pacific. *J. Phys. Oceanogr.*, 42(6):889–909, 2012.

L. Armi and W. Zenk. Large lenses of highly saline mediterranean water. *Journal of Physical Oceanography*, 14(10):1560–1576, 1984.

L. Armi, D. Hebert, N. Oakey, J. Price, P. Richardson, H. T. Rossby, and B. Ruddick. Two years in the life of a Mediterranean salt lens. *J. Phys. Oceanogr.*, 19:354–370, March 1989.

Y. Bebieva and M.-L. Timmermans. An examination of double-diffusive processes in a mesoscale eddy in the Arctic Ocean. *Journal of Geophysical Research*, 120, 2015.

Y. Bebieva and M.-L. Timmermans. The relationship between double-diffusive intrusions and staircases in the Arctic Ocean. *Journal of Physical Oceanography*, 47(4):867–878, 2017. doi: 10.1175/JPO-D-16-0265.1. URL http://dx.doi.org/10.1175/JPO-D-16-0265.1.

E. T. Brugler, R. S. Pickart, G. W. K. Moore, S. Roberts, T. Weingartner, and H. Statscewich. Seasonal to interannual variability of the Pacific water boundary current in the Beaufort Sea. *Progress in Oceanography*, 2014.

J. L. Cairns and G. O. Williams. Internal wave observations from a midwater float, 2. *J. Geophys. Res.*, 81:1943–1950, 1976.

E. Carmack, I. Polyakov, L. Padman, I. Fer, E. Hunke, J. Hutchings, J. Jackson, D. Kelley, R. Kwok, C. Layton, et al. Towards quantifying the increasing role of oceanic heat in sea ice

loss in the new Arctic. *Bulletin of the American Meteorological Society*, 2015.

M. Chanona, S. Waterman, and Y. Gratton. Variability of internal wave-driven mixing and stratification in Canadian Arctic shelf and shelf-slope waters. *Journal of Geophysical Research: Oceans*, 123(12):9178–9195, 2018.

S.-Y. Chao and P.-T. Shaw. A numerical study of dense water outflows and halocline anticyclones in an Arctic baroclinic slope current. *Journal of Geophysical Research: Oceans*, 108(C7), 2003.

B. S. Chinn, J. B. Girton, and M. H. Alford. The impact of observed variations in the shear-to-strain ratio of internal waves on inferred turbulent diffusivities. *Journal of Physical Oceanography*, 46(11):3299–3320, 2016.

S. T. Cole, J. M. Toole, L. Rainville, and C. M. Lee. Internal waves in the Arctic: Influence of ice concentration, ice roughness, and surface layer stratification. *Journal of Geophysical Research: Oceans*, 123, 2018.

W. B. Corlett and R. S. Pickart. The Chukchi slope current. *Progress in Oceanography*, 2017.

E. D'Asaro. The energy flux from the wind to near-inertial motions in the mixed layer. *J. Phys. Oceanogr.*, 15(8):1043–1059, 1985.

E. D'Asaro and J. H. Morison. Internal waves and mixing in the Arctic Ocean. *Deep-Sea Research*, 39(Suppl. 2):S459–S484, 1992.

E. A. D'Asaro. Generation of submesoscale vortices: A new mechanism. *J. Geophys. Res.*, 93 (C6):6685–6693, 1988a. Eddies, vorticity generation.

E. A. D'Asaro. Observations of small eddies in the Beaufort Sea. *J. Geophys. Res.*, 93(C6): 6669–6684, 1988b. Eddies, vorticity generation, vortices.

E. A. D'Asaro. The decay of wind-forced mixed layer inertial oscillations due to the β effect. *J. Geophys. Res.*, 94(C2):2045–2056, February 1989.

E. A. D'Asaro and M. D. Morehead. Internal waves and velocity fine structure in the Arctic Ocean. *Journal of Geophysical Research: Oceans (1978–2012)*, 96(C7):12725–12738, 1991.

H. V. Dosser and L. Rainville. Dynamics of the changing near-inertial internal wave field in the Arctic Ocean. *J. Phys. Oceanogr.*, 2016.

I. Eisenman, T. Schneider, D. S. Battisti, and C. M. Bitz. Consistent changes in the sea ice seasonal cycle in response to global warming. *Journal of Climate*, 24(20):5325–5335, 2011.

I. Fer. Weak vertical diffusion allows maintenance of cold halocline in the central Arctic. *Atmos. Oceanic Sci. Lett*, 2(3):148–152, 2009.

I. Fer, R. Skogseth, and F. Geyer. Internal Waves and Mixing in the Marginal Ice Zone near the Yermak Plateau. *J. Phys. Oceanogr.*, 40(7):1613–1630, 2010. ISSN 1520-0485.

E. C. Fine, J. A. Mackinnon, M. H. Alford, and J. B. Mickett. Microstructure observations of turbulent heat fluxes in a warm-core Canada basin eddy. *Journal of Physical Oceanography*, 48(2397–2418):2397–2418, 2018.

N. Furuichi, T. Hibiya, and Y. Niwa. Model predicted distribution of wind-induced internal wave energy in the world's oceans. *J. Geophys. Res.*, 113(C09034), 2008. doi: 10.1029/2008JC004768.

C. Garrett and W. Munk. Oceanic mixing by breaking internal waves. *Deep-Sea Res.*, 19:823–832, 1972.

C. J. R. Garrett and W. H. Munk. Space-time scales of internal waves: A progress report. *J. Geophys. Res.*, 80(3):291–297, january 1975.

C. H. Gibson. Fossil turbulence and intermittency in sampling ocean mixing processes. *J. Geophys. Res.*, 92(C5):5383–5404, 1987.

A. E. Gill. *Atmosphere-Ocean Dynamics*. Academic Press, 1982.

A. E. Gill. On the behavior of internal waves in the wake of a storm. *J. Phys. Oceanogr.*, 14: 1129–1151, 1984.

M. Gregg. Scaling turbulent dissipation in the thermocline. *J. Geophys. Res.*, 94(C7):9686–9698, 1989.

M. Gregg, D. Winkel, and T. Sanford. Varieties of fully resolved spectra of vertical shear. *J. Phys. Oceanogr.*, 23(1):124–141, january 1993.

M. Gregg, E. D'Asaro, J. Riley, and E. Kunze. Mixing efficiency in the ocean. *Annual review of marine science*, (0), 2018.

M. C. Gregg. Microstructure patches in the thermocline. *J. Phys. Oceanogr.*, 10(6):915–943, June 1980.

M. C. Gregg and L. J. Pratt. Flow and hydraulics near the sill of hood canal, a strongly sheared, continuously stratified fjord. *J. Phys. Oceanogr.*, 40(5):1087–1105, 2010. doi: 10.1175/2010JPO4312.1. URL http://journals.ametsoc.org/doi/abs/10.1175/2010JPO4312.1.

M. C. Gregg, T. B. Sanford, and D. P. Winkel. Reduced mixing from the breaking of internal waves in equatorial waters. *Nature*, 422:513–515, April 2003.

J. D. Guthrie, J. H. Morison, and I. Fer. Revisiting internal waves and mixing in the arctic ocean. *Journal of Geophysical Research: Oceans*, 118(8):3966–3977, 2013.

J. D. Guthrie, I. Fer, and J. Morison. Observational validation of the diffusive convection flux laws in the Amundsen Basin, Arctic Ocean. *Journal of Geophysical Research: Oceans*, 120 (12):7880–7896, 2015.

C. Halle. Internal wave variability in the Beaufort Sea during the winter of 1993/1994. *J. Geophys. Res.*, 108(C7):doi:10.1029/2000JC000703, 2003.

L. N. Howard. Note on a paper of John W. Miles. *J. Fluid Mech.*, 10:509–512, 1961.

K. L. Hunkins. Subsurface eddies in the arctic ocean. In *Deep Sea Research and Oceanographic Abstracts*, volume 21, pages 1017–1033. Elsevier, 1974.

H. E. Huppert and J. S. Turner. Double-diffusive convection. *J. Fluid Mech.*, 106:299–329, 1981.

R. Inoue, H. Yamazaki, F. Wolk, T. Kono, and J. Yoshida. An estimation of buoyancy flux for a mixture of turbulence and double diffusion. *J. Phys. Oceanogr.*, 37(3):611–624, 2007.

M. Itoh, S. Nishino, Y. Kawaguchi, and T. Kikuchi. Barrow canyon volume, heat, and freshwater fluxes revealed by long-term mooring observations between 2000 and 2008. *Journal of Geophysical Research: Oceans*, 118(9):4363–4379, 2019/08/04 2013. doi: 10.1002/jgrc.20290. URL https://doi.org/10.1002/jgrc.20290.

J. M. Jackson, E. Carmack, F. McLaughlin, S. E. Allen, and R. Ingram. Identification, characterization, and change of the near-surface temperature maximum in the canada basin, 1993–2008. *Journal of Geophysical Research: Oceans*, 115(C5), 2010.

D. Kadko, R. S. Pickart, and J. Mathis. Age characteristics of a shelf-break eddy in the western Arctic and implications for shelf-basin exchange. *Journal of Geophysical Research: Oceans*, 113(C2), 2008.

Y. Kawaguchi, M. Itoh, and S. Nishino. Detailed survey of a large baroclinic eddy with extremely high temperatures in the Western Canada Basin. *Deep Sea Res. I*, 66:90–102, 2012.

Y. Kawaguchi, T. Kikuchi, and R. Inoue. Vertical heat transfer based on direct microstructure measurements in the ice-free Pacific-side Arctic Ocean: the role and impact of the Pacific water intrusion. *Journal of Oceanography*, 70(4):343–353, 2014.

Y. Kawaguchi, S. Nishino, J. Inoue, K. Maeno, H. Takeda, and K. Oshima. Enhanced diapycnal mixing due to near-inertial internal waves propagating through an anticyclonic eddy in the ice-free Chukchi Plateau. *Journal of Physical Oceanography*, 46(8):2457–2481, 2016. URL http://dx.doi.org/10.1175/JPO-D-15-0150.1.

D. Kelley. Effective diffusivities within oceanic thermohaline staircases. *J. Geophys. Res.*, 89: 10,484–10,488, 1984.

D. Kelley. Fluxes through diffusive staircases, a new formulation. *J. Geophys. Res.*, 95:3365–3371, 1990.

D. E. Kelley, H. J. S. Fernando, A. E. Gargett, J. Tanny, and E. Özsoy. The diffusive regime of double-diffusive convection. *Progress in Oceanography*, 56:461–481, Mar. 2003. doi: 10.1016/S0079-6611(03)00026-0.

R. A. Krishfield, A. J. Plueddemann, and S. Honjo. Eddys in the Arctic Ocean from IOEB ADCP data. Technical report, Woods Hole Oceanographic Institution, 2002.

E. Kunze. Near-inertial wave propagation in geostrophic shear. *J. Phys. Oceanogr.*, 15:544–565, 1985.

E. Kunze. The mean and near-inertial velocity fields in a warm-core ring. *J. Phys. Oceanogr.*, 16: 1444–1461, 1986.

E. Kunze. A review of oceanic salt-fingering theory. *Progress in Oceanography*, 56(3):399–417, 2003.

E. Kunze and T. B. Sanford. Observations of near-inertial waves in a front. *J. Phys. Oceanogr.*, 14:566–581, 1984.

E. Kunze, E. Firing, J. Hummon, T. K. Chereskin, and A. Thurnherr. Global abyssal mixing inferred from lowered ADCP shear and CTD strain profiles. *J. Phys. Oceanogr.*, 36(8): 1553–1576, 2006.

Y.-D. Lenn, P. Wiles, S. Torres-Valdes, E. Abrahamsen, T. Rippeth, J. Simpson, S. Bacon, S. Laxon, I. Polyakov, V. Ivanov, et al. Vertical mixing at intermediate depths in the Arctic boundary current. *Geophysical Research Letters*, 36(5), 2009.

M. D. Levine, C. A. Paulson, and J. H. Morison. Internal waves in the arctic ocean: Comparison with lower-latitude observations. *J. Phys. Oceanogr.*, 15(6):800–809, 1985.

B. J. Lincoln, T. P. Rippeth, Y.-D. Lenn, M. L. Timmermans, W. J. Williams, and S. Bacon. Wind-driven mixing at intermediate depths in an ice-free Arctic ocean. *Geophysical Research Letters*, 43(18):9749–9756, 2016.

C. Lique, J. D. Guthrie, M. Steele, A. Proshutinsky, J. H. Morison, and R. Krishfield. Diffusive vertical heat flux in the Canada Basin of the Arctic Ocean inferred from moored instruments. *J. Geophys. Res. Oceans*, 119(1):496–508, 2014.

D. A. Luketina and J. Imberger. Determining turbulent kinetic energy dissipation from Batchelor curve fitting. *Journal of atmospheric and oceanic technology*, 18(1):100–113, 2001.

J. A. MacKinnon, J. D. Nash, M. H. Alford, A. J. Lucas, J. B. Mickett, E. L. Shroyer, A. F.

Waterhouse, A. Tandon, D. Sengupta, A. Mahadevan, M. Ravichandran, R. Pinkel, D. L. Rudnick, C. B. Whalen, M. S. Alberty, J. Sreelekha, E. C. Fine, D. Chaudhuri, and G. L. Wagner. A tale of two spicy seas. *Oceanography*, 29(2):50–61, 2016.

J. A. MacKinnon, M. H. Alford, J. K. Ansong, B. K. Arbic, A. Barna, B. P. Briegleb, F. O. Bryan, M. C. Buijsman, E. P. Chassignet, G. Danabasoglu, and et al. Climate process team on internal-wave driven ocean mixing. *Bulletin of the American Meteorological Society*, 98(11): 2429–2454, 2017. ISSN 1520-0477. doi: 10.1175/bams-d-16-0030.1.

J. A. MacKinnon, J. Thomson, H. L. Simmons, and et al. Soda mushroom. 2019.

T. Manley and K. Hunkins. Mesoscale eddies of the Arctic Ocean. *Journal of Geophysical Research: Oceans*, 90(C3):4911–4930, 1985.

K. I. Martini, H. L. Simmons, C. A. Stoudt, and J. K. Hutchings. Near-Inertial Internal Waves and Sea Ice in the Beaufort Sea. *J. Phys. Oceanogr.*, 44(8):2212–2234, 2014.

B. D. May and D. E. Kelley. Effect of baroclinicity on double-diffusive interleaving. *J. Phys. Oceanogr.*, 27:1997–2008, 1997.

G. A. Maykut and N. Untersteiner. Some results from a time-dependent thermodynamic model of sea ice. *Journal of Geophysical Research*, 76(6):1550–1575, 1971.

H. Melling, R. Lake, D. Topham, and D. Fissel. Oceanic thermal structure in the western Canadian Arctic. *Continental Shelf Research*, 3(3):233–258, 1984.

E. J. Metzger, O. M. Smedstad, P. G. Thoppil, H. E. Hurlburt, J. A. Cummings, A. J. Wallcraft, L. Zamudio, D. S. Franklin, P. G. Posey, M. W. Phelps, et al. Us navy operational global ocean and arctic ice prediction systems. *Oceanography*, 27(3):32–43, 2014.

A. Meyer, I. Fer, A. Sundfjord, and A. K. Peterson. Mixing rates and vertical heat fluxes north of Svalbard from Arctic winter to spring. *Journal of Geophysical Research: Oceans*, 122(6): 4569–4586, 2017.

J. B. Mickett, Y. L. Serra, M. F. Cronin, and M. H. Alford. Resonant forcing of mixed layer inertial motions by atmospheric easterly waves in the Northeast tropical Pacific. *J. Phys. Oceanogr.*, 40(2):401–416, 2010.

J. W. Miles. On the stability of heterogeneous shear flows. *J. Fluid Mech.*, 10:496–508, 1961.

J. H. Morison, C. E. Long, and M. D. Levine. Internal wave dissipation under sea ice. *Journal of Geophysical Research: Oceans (1978–2012)*, 90(C6):11959–11966, 1985.

R. D. Muench, J. T. Gunn, T. E. Whitledge, P. Schlosser, and W. Smethie. An Arctic Ocean cold core eddy. *Journal of Geophysical Research: Oceans*, 105(C10):23997–24006, 2000.

A. Münchow and E. C. Carmack. Synoptic flow and density observations near an Arctic shelf break. *J. Phys. Oceanogr.*, 27(7):1402–1419, 1997.

A. Münchow, E. C. Carmack, and D. A. Huntley. Synoptic density and velocity observations of slope waters in the Chukchi and East-Siberian seas. *Journal of Geophysical Research: Oceans*, 105(C6):14103–14119, 2000.

W. Munk and C. Wunsch. Abyssal recipes II: energetics of tidal and wind mixing. *Deep-Sea Res. Part I*, 45:1977–2010, 1998.

S. Neshyba, V. T. Neal, and W. Denner. Temperature and conductivity measurements under Ice Island T-3. *Journal of Geophysical Research*, 76(33):8107–8120, 1971.

J. Newton, K. Aagaard, and L. K. Coachman. Baroclinic eddies in the Arctic Ocean. In *Deep Sea Research and Oceanographic Abstracts*, volume 21, pages 707–719. Elsevier, 1974.

A. Nikolopoulos, R. S. Pickart, P. S. Fratantoni, K. Shimada, D. J. Torres, and E. P. Jones. The western Arctic boundary current at 152 W: Structure, variability, and transport. *Deep Sea Research Part II: Topical Studies in Oceanography*, 56(17):1164–1181, 2009.

T. R. Osborn. Estimates of the local rate of vertical diffusion from dissipation measurements. *J. Phys. Oceanogr.*, 10:83–89, 1980.

T. R. Osborn and C. S. Cox. Oceanic fine structure. *Geophys. Fluid Dyn.*, 3:321–345, 1972.

J. E. Overland and M. Wang. When will the summer Arctic be nearly sea ice free? *Geophysical Research Letters*, 40(10):2097–2101, 2013.

L. Padman. Momentum fluxes through sheared oceanic thermohaline steps. *Journal of Geophysical Research: Oceans*, 99(C11):22491–22499, 1994. ISSN 2156-2202. doi: 10.1029/94JC01741. URL http://dx.doi.org/10.1029/94JC01741.

L. Padman and T. M. Dillon. Vertical heat fluxes through the Beaufort Sea thermohaline staircase. *J. Geophys. Res.*, 92:10,799–10,806, 1987.

L. Padman and T. M. Dillon. On the horizontal extent of the Canada Basin thermohaline steps. *J. Phys. Oceanogr.*, 18:1458–1462, 1988.

L. Padman and T. M. Dillon. Thermal microstructure and internal waves in the Canada Basin diffusive staircase. *Deep-Sea Res.*, 36:531–542, 1989.

L. Padman and T. M. Dillon. Turbulent mixing near the Yermak Plateau during the Coordinated Eastern Arctic Experiment. *J. Geophys. Res*, 96(C3):4769–4782, 1991.

L. Padman and S. Erofeeva. A barotropic inverse tidal model for the arctic ocean. *Geophys. Res. Lett.*, 31(L02303), 2004.

L. Padman, M. D. Levine, T. Dillon, J. Morison, and R. Pinkel. Hydrography and microstructure of an Arctic cyclonic eddy. *J. Geophys. Res.*, 95(C6):9411–9420, 1990.

H. Peters, M. Gregg, and J. Toole. On the parameterization of equatorial turbulence. *J. Geophys. Res.*, 93:1199–1218, 1988.

A. K. Peterson, I. Fer, M. G. McPhee, and A. Randelhoff. Turbulent heat and momentum fluxes in the upper ocean under arctic sea ice. *Journal of Geophysical Research: Oceans*, 122(2): 1439–1456, 2017.

R. S. Pickart. Shelfbreak circulation in the Alaskan Beaufort Sea: Mean structure and variability. *Journal of Geophysical Research: Oceans (1978–2012)*, 109(C4), 2004.

R. S. Pickart and G. Stossmeister. Outflow of Pacific water from the Chukchi Sea to the Arctic Ocean. *Chin. J. Polar Oceanogr.*, 19(2-English):135–148, 2008.

R. S. Pickart, T. J. Weingartner, L. J. Pratt, S. Zimmermann, and D. J. Torres. Flow of winter-transformed pacific water into the western arctic. *Deep-Sea Res. II*, 52(24):3175–3198, 2005.

R. Pinkel. Near-inertial wave propagation in the western Artic. *J. Phys. Oceanogr.*, 35(5): 645–665, 2005.

M. N. Pisareva, R. S. Pickart, M. Spall, C. Nobre, D. Torres, G. Moore, and T. E. Whitledge. Flow of pacific water in the western Chukchi Sea: Results from the 2009 RUSALCA expedition. *Deep Sea Res. I*, 105:53–73, 2015. doi: http://dx.doi.org/10.1016/j.dsr.2015.08.011.

A. Plueddemann, R. Krishfield, T. Takizawa, K. Hatakeyama, and S. Honjo. Upper ocean velocities in the Beaufort Gyre. *Geophysical research letters*, 25(2):183–186, 1998.

R. T. Pollard and R. C. Millard. Comparison between observed and simulated wind-generated inertial oscillations. *Deep-Sea Res.*, 17:153–175, 1970.

I. V. Polyakov, A. V. Pnyushkov, R. Rember, V. V. Ivanov, Y.-D. Lenn, L. Padman, and E. C. Carmack. Mooring-based observations of double-diffusive staircases over the Laptev Sea slope. *Journal of Physical Oceanography*, 42(1):95–109, 2012. doi: 10.1175/2011JPO4606.1. URL http://dx.doi.org/10.1175/2011JPO4606.1.

K. Polzin, E. Kunze, J. Hummon, and E. Firing. The finescale response of lowered ADCP velocity profiles. *J. Atmos. Oceanic Technol.*, 19:205–224, February 2002.

K. L. Polzin, J. M. Toole, and R. W. Schmitt. Finescale parameterizations of turbulent dissipation. *J. Phys. Oceanogr.*, 25:306–328, 1995.

K. L. Polzin, A. C. Naveira Garabato, T. N. Huussen, B. M. Sloyan, and S. Waterman. Finescale parameterizations of turbulent dissipation. *Journal of Geophysical Research: Oceans*, 119(2):

1383–1419, 2014. ISSN 2169-9291. doi: 10.1002/2013JC008979. URL http://dx.doi.org/10.1002/2013JC008979.

L. Rainville and P. Winsor. Mixing across the arctic ocean: Microstructure observations during the Beringia 2005 expedition. *Geophys. Res. Lett.*, 35(L08606):1–5, 2008. doi: doi:10.1029/2008GL033532.

L. Rainville and R. Woodgate. Observations of internal wave generation in the seasonally ice-free Arctic. *Geophysical Research Letters*, 36(23):L23604, 2009. ISSN 0094-8276.

J. J. Rohr, E. C. Itsweire, K. N. Helland, and C. W. V. Atta. Growth and decay of turbulence in a stably stratified shear flow. *Journal of Fluid Mechanics*, 195:77–111, 1988. doi: 10.1017/S0022112088002332.

B. Ruddick and K. Richards. Oceanic thermohaline intrusions: Observations. *Prog. Oceanog.*, 56:499–523, 2003.

B. Ruddick, A. Anis, and K. Thompson. Maximum likelihood spectral fitting: The Batchelor spectrum. *J. Atmos. Ocean. Tech.*, 17:1541–1555, 2000.

B. R. Ruddick. Intrusive mixing in a Mediterranean salt lens – Intrusion slopes and dynamical mechanisms. *J. Phys. Oceanogr.*, 22:1274–1285, 1992.

B. R. Ruddick and J. S. Turner. The vertical length scale of double-diffusive intrusions. *Deep-Sea Res.*, 26A:903–913, 1979.

B. R. Ruddick, N. S. Oakey, and H. D. Measuring lateral heat flux across a thermohaline front: A model and observational test. *J. Mar. Res.*, 68(3-4):523–539, 2010.

B. Rudels. Arctic basin circulation. *Encyclopedia of Ocean Sciences. Academic Press, San Diego*, pages 177–187, 2001.

B. Rudels, E. P. Jones, U. Schauer, and P. Eriksson. Atlantic sources of the arctic ocean surface and halocline waters. *Polar Research*, 23(2):181–208, 2004.

S. Saha, S. Moorthi, H.-L. Pan, X. Wu, J. Wang, S. Nadiga, P. Tripp, R. Kistler, J. Woollen, D. Behringer, H. Liu, D. Stokes, R. Grumbine, G. Gayno, J. Wang, Y.-T. Hou, H.-y. Chuang, H.-M. H. Juang, J. Sela, M. Iredell, R. Treadon, D. Kleist, P. Van Delst, D. Keyser, J. Derber, M. Ek, J. Meng, H. Wei, R. Yang, S. Lord, H. van den Dool, A. Kumar, W. Wang, C. Long, M. Chelliah, Y. Xue, B. Huang, J.-K. Schemm, W. Ebisuzaki, R. Lin, P. Xie, M. Chen, S. Zhou, W. Higgins, C.-Z. Zou, Q. Liu, Y. Chen, Y. Han, L. Cucurull, R. W. Reynolds, G. Rutledge, and M. Goldberg. The ncep climate forecast system reanalysis. *Bulletin of the American Meteorological Society*, 91(8):1015–1058, 2019/08/21 2010. doi: 10.1175/2010BAMS3001.1. URL https://doi.org/10.1175/2010BAMS3001.1.

T. B. Sanford. Spatial structure of thermocline and abyssal internal waves. In *Dynamics of Oceanic Internal Gravity Waves, II: Proceedings of the 'Aha Huliko'a Hawaiian Winter Workshop*, pages 109–141. DTIC Document, 1991.

P.-T. Shaw and S.-Y. Chao. Effects of a baroclinic current on a sinking dense water plume from a submarine canyon and heton shedding. *Deep Sea Research Part I: Oceanographic Research Papers*, 50(3):357–370, 2003.

W. Shaw, T. Stanton, M. McPhee, J. Morison, and D. Martinson. Role of the upper ocean in the energy budget of arctic sea ice during sheba. *Journal of Geophysical Research: Oceans (1978–2012)*, 114(C6), 2009.

N. C. Shibley, M.-L. Timmermans, J. R. Carpenter, and J. M. Toole. Spatial variability of the arctic ocean's double-diffusive staircase. *Journal of Geophysical Research: Oceans*, 122(2): 980–994, 2017.

K. Shimada, E. C. Carmack, K. Hatakeyama, and T. Takizawa. Varieties of shallow temperature maximum waters in the western Canadian Basin of the Arctic Ocean. *Geophysical Research Letters*, 28(18):3441–3444, 2001.

K. Shimada, T. Kamoshida, M. Itoh, S. Nishino, E. Carmack, F. McLaughlin, S. Zimmermann, and A. Proshutinsky. Pacific Ocean inflow: Influence on catastrophic reduction of sea ice cover in the Arctic Ocean. *Geophysical Research Letters*, 33(8), 2006.

E. L. Shroyer. Turbulent kinetic energy dissipation in Barrow Canyon. *J. Phys. Oceanogr.*, 42(6): 1012–1021, 2012.

A. Sirevaag and I. Fer. Vertical heat transfer in the Arctic Ocean: The role of double-diffusive mixing. *Journal of Geophysical Research: Oceans*, 117(C7), 2012.

W. D. Smyth and S. Kimura. Instability and diapycnal momentum transport in a double-diffusive, stratified shear layer. *Journal of Physical Oceanography*, 37(6):1551–1565, 2007. doi: 10.1175/JPO3070.1. URL http://dx.doi.org/10.1175/JPO3070.1.

M. A. Spall, R. S. Pickart, P. S. Fratantoni, and A. J. Plueddemann. Western Arctic shelfbreak eddies: Formation and transport. *J. Phys. Oceanogr.*, 38(8):1644–1668, 2008.

L. St. Laurent and R. Schmitt. The contribution of salt fingers to vertical mixing in the North Atlantic Tracer Release Experiment. *J. Phys. Oceanogr.*, 27(7):1404–1424, 1999.

A. P. Stamp, G. O. Hughes, R. I. Nokes, and R. W. Griffiths. The coupling of waves and convection. *Journal of Fluid Mechanics*, 372:231–271, 1998.

M. Steele, J. Morison, W. Ermold, I. Rigor, M. Ortmeyer, and K. Shimada. Circulation of summer pacific halocline water in the arctic ocean. *Journal of Geophysical Research: Oceans*

(1978–2012), 109(C2), 2004.

M. E. Stern. Lateral mixing of water masses. *Deep-Sea Res.*, 14:747–753, 1967.

J. E. Stopa, F. Ardhuin, and F. Girard-Ardhuin. Wave climate in the Arctic 1992-2014: seasonality and trends. *The Cryosphere*, 10:1605–1629, 2016.

A. Sundfjord, I. Fer, Y. Kasajima, and H. Svendsen. Observations of turbulent mixing and hydrography in the marginal ice zone of the Barents Sea. *Journal of Geophysical Research: Oceans (1978–2012)*, 112(C5), 2007.

J. Thomson and W. E. Rogers. Swell and sea in the emerging arctic ocean. *Geophysical Research Letters*, 41(9):3136–3140, 2014.

M. Timmermans, J. Toole, R. Krishfield, and P. Winsor. Ice-Tethered Profiler observations of the double-diffusive staircase in the Canada Basin thermocline. *J. Geophys. Res.*, 113(C00A02), 2008a.

M.-L. Timmermans. The impact of stored solar heat on Arctic sea ice growth. *Geophys. Res. Lett.*, 42(15):6399–6406, 2015. doi: 10.1002/2015GL064541.

M.-L. Timmermans and S. R. Jayne. The Arctic Ocean spices up. *Journal of Physical Oceanography*, 46(4):1277–1284, 2016. doi: 10.1175/JPO-D-16-0027.1. URL http://dx.doi.org/10.1175/JPO-D-16-0027.1.

M.-L. Timmermans, J. Toole, A. Proshutinsky, R. Krishfield, and A. Plueddemann. Eddies in the Canada Basin, Arctic Ocean, observed from ice-tethered profilers. *J. Phys. Oceanogr.*, 38(1): 133–145, 2008b.

M.-L. Timmermans, A. Proshutinsky, E. Golubeva, J. M. Jackson, R. Krishfield, M. McCall, G. Platov, J. Toole, W. Williams, T. Kikuchi, et al. Mechanisms of Pacific Summer Water variability in the Arctic's Central Canada Basin. *Journal of Geophysical Research: Oceans*, 119(11):7523–7548, 2014.

M.-L. Timmermans, J. M. Toole, and R. A. Krishfield. Warming of the interior arctic ocean linked to sea ice losses at the basin margins. *Sci. Adv.*, 4, 2018.

J. M. Toole, M.-L. Timmermans, D. K. Perovich, R. A. Krishfield, A. Proshutinsky, and J. Richter-Menge. Influences of the ocean surface mixed layer and thermohaline stratification on Arctic sea ice in the central Canada Basin. *Journal of Geophysical Research: Oceans (1978–2012)*, 115(C10), 2010.

J. S. Turner. *Buoyancy Effects in Fluids*. Cambridge, 1973.

J. S. Turner. Double-diffusive phenomena. *Ann. Rev. Fluid Mech.*, 6:37–55, 1974.

J. S. Turner. Double-diffusive intrusions into a density gradient. *J. Geophys. Res.*, 83:2887–2901, 1978.

W.-J. von Appen and R. S. Pickart. Two configurations of the western Arctic shelfbreak current in summer. *J. Phys. Oceanogr.*, 42(3):329–351, 2012.

E. Watanabe. Beaufort shelf break eddies and shelf-basin exchange of Pacific summer water in the western Arctic Ocean detected by satellite and modeling analyses. *Journal of Geophysical Research: Oceans (1978–2012)*, 116(C8), 2011.

A. F. Waterhouse, J. A. MacKinnon, J. D. Nash, M. H. Alford, E. Kunze, H. L. Simmons, K. L. Polzin, L. C. S. Laurent, O. M. Sun, R. Pinkel, L. D. Talley, C. B. Whalen, T. N. Huussen, G. S. Carter, I. Fer, S. Waterman, A. C. Naveira Garabato, T. B. Sanford, and C. M. Lee. Global patterns of diapycnal mixing from measurements of the turbulent dissipation rate. *J. Phys. Oceanogr.*, 44(7):1854–1872, 2014.

S. Waterman, K. L. Polzin, A. C. Naveira Garabato, K. L. Sheen, and A. Forryan. Suppression of internal wave breaking in the antarctic circumpolar current near topography. *J. Phys. Oceanogr.*, 44(5):1466–1492, 2014/05/02 2014. doi: 10.1175/JPO-D-12-0154.1.

J. C. Wesson and M. C. Gregg. Mixing at Camarinal Sill in the Strait of Gibraltar. *J. Geophys. Res.*, 99(C5):9847–9878, 1994.

C. B. Whalen, L. D. Talley, and J. A. MacKinnon. Spatial and temporal variability of global ocean mixing inferred from Argo profiles. *Geophys. Res. Lett.*, 39(L18612): doi:10.1029/2012GL053196, 2012.

C. B. Whalen, J. A. MacKinnon, L. D. Talley, and A. F. Waterhouse. Estimating the mean diapycnal mixing using a finescale strain parameterization. *Journal of Physical Oceanography*, 45(4):1174–1188, 2015/05/13 2015. doi: 10.1175/JPO-D-14-0167.1. URL http://dx.doi.org/10.1175/JPO-D-14-0167.1.

K. B. Winters and E. A. D'Asaro. Diascalar flux and the rate of fluid mixing. *J. Fluid Mech.*, 317: 179–193, 1996.

R. A. Woodgate, T. Weingartner, and R. Lindsay. The 2007 Bering Strait oceanic heat flux and anomalous Arctic sea-ice retreat. *Geophysical Research Letters*, 37(1), 2010.

M. Zhao, M.-L. Timmermans, S. Cole, R. Krishfield, A. Proshutinsky, and J. Toole. Characterizing the eddy field in the Arctic Ocean halocline. *Journal of Geophysical Research: Oceans*, 119 (12):8800–8817, 2014.